NTNU
Norwegian University of
Science and Technology

A Spectroscopic Study of in situ Magnetic Doping of Novel Layered Materials for Spintronics

Kristoffer William Hunvik

Master of Science in Physics and Mathematics
Submission date: June 2016
Supervisor: Justin Wells, IFY

Norwegian University of Science and Technology
Department of Physics

Preface

This is the Master's thesis of my Master of Science degree in Applied Physics and Mathematics. The work on this project has been carried out during the spring semester of 2016, my last semester as a student at NTNU. The project has been carried out at Justin Wells' laboratory at NTNU and at Phil King's laboratory at University of St. Andrews.

My work with this project has included doing experiments in the NTNU XPS laboratory, one week of experiments carried out in Phil Kings laboratory in St. Andrews, carrying out data analysis and understanding the experiment. I would like to thank my supervisor Associate Professor Justin Wells at the Department of Physics at NTNU for his help and guidance throughout this semester. I would like to thank Federico Mazzola and Simon Cooil for their helpful insights and assistance with the experiments. I would like to thank Mathieu Børkja for his collaboration with the experiments. I would also like to thank Philip King for allowing us to use his lab for a week, and Lewis Bawden and Liam Collins-McIntyre for their assistance.

Kristoffer William Bø Hunvik

June 2016

Trondheim

Abstract

MoS_2 is a layered material in the family of the transition metal dicalchogenides (TMDCs), which hosts interesting spin physics. Even though the TMDCs are nonmagnetic in their bulk form, a local breaking of inversion symmetry combined with a strong in-plane dipole and a strongly localized character of the electron wavefunctions, causes the TMDCs to show highly anisotropic spintronic properties. In this work the effects of *in situ* evaporation and annealing of iron on the surface of MoS_2 are studied by the means of X-ray Photoemission Spectroscopy (XPS), Low Energy Electron Diffraction (LEED) and Angle Resolved Photoemission Spectroscopy (ARPES). This is to understand how to grow model systems to allow magnetic impurities and magnetic fields to influence the electronic properties of MoS_2. This is done by growth of thin films on MoS_2 and attempting intercalate iron into the crystal structure of MoS_2.

The results show that it is possible to grow fairly homogeneous films of iron on the surface of MoS_2, which cause band bending in the valence band and core levels of 0.41 ± 0.07 eV towards lower binding energy. The iron on the surface creates a flat band at the Fermi level, suggesting together with weaker intensity in the LEED measurements that the iron is not forming any ordered structure on the surface. By counterdoping with potassium the band bending from the iron is reduced such that the core levels return to their initial position. The results show that intercalation at room temperature is unlikely. Angle resolved XPS (ARXPS) data has been acquired and modelled by using a multilayer model and a model for agglomeration/intercalation. With the sample annealed to 400°C with potassium and iron on the surface, the data and the two models suggest that the iron could be intercalating with some iron left on the surface. With the sample annealed to 500°C with iron on the surface, the models disagree. The multilayer model suggests intercalation within the first two unit cells of the crystal and the other suggests 3D particle growth.

A preliminary low temperature ARPES study shows that for lower doses of iron the semiconducting behaviour of MoS_2 is preserved. For half a monolayer of iron on MoS_2, the valence band shifts towards lower binding energy by 0.12 eV suggesting n-doping. The n-type doping could be due to inhomogeneous band bending or iron-carbide forming on the surface. For another sample with 0.1 nm of iron, the two original bands at $\bar{K}$-point split into four bands, which could originate from an electrical potential and/or magnetic effect due to iron on the surface.

The results in this work provide a good foundation for further studies on the influence from magnetic impurities on these layered materials, to pave the way for spintronics for a new generation of multifunctional electronic devices.

Samandrag

MoS_2 er eit lagdelt materiale i familien "transition metal dicalchogenides" (TMDC), som har interessante spinntroniske eigenskapar. Sjølv om TMDCar ikkje er magnetiske i sin bulk form, fører eit lokalt brudd i inversjonsymmetrien kombinert med ein sterk magnetisk dipol i planet til at TMDCar har svært anisotropiske spinntroniske eigenskapar. I dette arbeidet har effekten av fordamping og oppvarming av jern på overflata av MoS_2 blitt studert ved hjelp av røntgen fotoemisjonsspektroskopi (XPS), låg energi elektrondiffraksjon (LEED) og vinkeloppløyst fotoemisjonspekstroskopi (ARPES). Dette er for å forstå korleis ein kan lage modellsystem for å få magnetiske ureiningar og magnetiske felt til å påvirke dei elektroniske eigenskapane til MoS_2 på ein kontrollert måte. Dette har blitt gjort ved vekst av tynnfilmar av ulik tjukkelse på MoS_2 og ved å forsøke å få jern til å migrere inn i van der Waals gapet i krystallstrukturen i MoS_2.

Resultata viser at det mogleg å gro relativt homogene tynnfilmar av jern på overflata av MoS_2, noko som fører til bandbøying i valensbandet og kjernenivåa med 0.41 ± 0.08 eV mot lågare bindingsenergi. Jernet på overflata skapar eit flatt band ved Fermi-nivået, noko som tyder saman med den svake intensiteten i LEED målingane at jernet ikkje dannar ein ordna struktur på overflata. Ved fordamping av kalium på overflata har det blitt vist at bandbøyinga frå jernet er redusert slik at kjernenivåa går tilbake til utgansposisjonen av ei rein overflate. Resultata viser at migrasjon av jern inn i van der Waals gapet ved romtemperatur er usannsynlig. Data frå vinkeloppløyst XPS (ARXPS) er blitt modellert ved hjelp av ein fleirlags modell og ein modell for 3D-partiklar/migrasjon. Data og modelltilpasning til dei to modellane viser at om prøva er varma opp til 400°C med kalium og jern på overflata så migrerar jernet mest sannsynleg inn i dei ein til to første einingcellene med noko jern att på overflata. For ei prøve varma opp til 500°C med jern på overflata er modellane ueinige. Fleirlags modellen tyder på at jernet fordelar seg i van der Waals gapa i dei to første einingcellene, medan den andre modellen tyder på at jernet dannar 3D partiklar av jern på overflata.

Innleiande låg temperatur ARPES studiar viser at for lågare dosar av jern beheld MoS_2 dei halvleiande eigenskapane sine. Ved eit halvt atomlag på overflata med jern, skiftar valensbandet seg mot lågare bindingsenergi med 0.12 eV, noko tyder på n-doping. Denne dopinga kjem moglegvis frå ikkje-homogen bandbøyning eller jern som binder seg med karbon på overflata. For ei anna prøve med 0.1 nm jern på overflata, splittar dei originalt to banda ved $\bar{K}$-punktet opp i fire nye band. Dette kan kome frå eit elektrisk potensial på overflata og/eller magnetiske effektar som oppstår på grunn av jern på overflata.

Resultata i dette arbeidet gir eit godt grunnlag for vidare studiar av påvirkninga frå magnetiske ureiningar på desse lagdelte materiala, noko som kan bane veg framtidig utvikling innan spinntronikk.

Contents

List of Tables

List of Figures

List of abbreviations

AES	=	Auger electron spectroscopy
AFM	=	Atomic force microscope
ARPES	=	Angle-resolved photoemission spectroscopy
ARXPS	=	Angle resolved X-ray photoemission spectroscopy
BZ	=	Brillouin zone
CEMS	=	Conversion electron Mössbauer spectroscopy
EDC	=	Energy distribution curve
FAT	=	Fixed analyser transmission mode
FWHM	=	Full width at half maximum
LEED	=	Low energy electron diffraction
PEEM	=	Photoemission electron microscopy
PES	=	Photoemission spectroscopy
MOKE	=	Magneto-optic Kerr effect
SEM	=	Scanning electron microscope
STM	=	Scanning tunneling microscopy
TEM	=	Transmission electron microscopy
TMDC	=	Transition Metal Dichalcogenides
UPS	=	Ultra-violet photoemission spectroscopy
XPD	=	X-ray photoelectron diffraction
XPS	=	X-ray photoemission spectroscopy

1 Introduction

1.1 Background

The transition metal dichalcogenides (TMDCs) are a family of around sixty different compounds that form layered structures of MX_2, where M is a transition metal such as W, Nb or Mo, and X is a chalcogenide such as S, Se or Te. Thoroughly investigated in the 1970s and 1980s, they regained their popularity after the discovery of graphene [1]. Despite being nonmagnetic in their bulk form, they exhibit interesting spin physics. In the 2H-polymorph of the layered materials, a local breaking of inversion symmetry, combined with a strong in-plane dipole, causes the TMDCs to show a spin polarization in their electronic properties [2–4] even in their bulk phase. In addition, several of the family members exhibit exotic superconducting phases as well as a charge and spin density wave phases [5, 6].

By adding magnetic dopants to these materials they can exhibit even more interesting features. For example in TaS_2 iron-doping is known to induce superconductivity [7]. It is also known to have doping dependent ferromagnetic and anti-ferromagnetic phase transitions [8]. In $TaSe_2$ the superconducting transition temperature is enhanced by nickel doping [9]. Furthermore a theoretical study of an iron thin film on MoS_2 has found that such systems might hold a strong Dzyaloshinskii-Moriya interaction, and could potentially host interesting skyrmion dynamics in an external magnetic field [10].

1.2 Motivation

Understanding how to manipulate spins in materials is of great technological interest [11]. Spintronics is a developing technological field. As opposed to regular electronics where the electron's charge is utilized as an information carrier, the spin of the electron is utilized as an information carrier in spintronics. The combination of a 2D spin polarized material with a magnetic transition metal is crucial to the technical advancements, and warrants a detailed study.

MoS_2 is an abundant TMDC, and good quality crystals can be found in nature. Magnetically doping, creating high quality overlayers and intercalating TMDCs are complicated. The *in situ* creation of these behaviours in MoS_2 could provide useful information that hopefully can be transferred to other exotic compounds of the same family. This could pave the way to potentially intercalation in just one layer, having magnetic order in the surface whereas the bulk stay the same, and provide fundamental information of the formation of both superconductivity and charge density wave order.

By magnetically doping a semiconductor like MoS_2 potentially a diluted magnetic semiconductor can be created [12]. A diluted magnetic semiconductor is created by substitutional doping of magnetic impurities to make a material both semiconducting and ferromagnetic. This would then host the opportunity to create spintronic devices like a spin transistor. There is controversy in the field [13], and gaining further knowledge of the phenomenas leading to this would be of both fundamental and technological advancement.

Doping and intercalation of metals on TMDCs has been studied by several research groups. The materials have long been used as catalysts for hydrodesulfurization and as solid film lubricants [14]. Kamaratos *et al.* [15] studied intercalation of iron, nickel and palladium in the bulk of single crystal MoS_2 by Auger electron spectroscopy (AES) and Ar^+-sputtering with room temperature growth and 1200 K postannealing. They reported that nickel and palladium tend to diffuse uniformly into the bulk, whereas iron atoms intercalated between the layers. In Ref.[16] they study the surface morphology, magnetism and the chemical state of iron on a geological MoS_2 sample by X-ray Photoelectron spectroscopy (XPS), Scanning Tunneling Microscopy (STM) and Magneto-optic Kerr effect (MOKE). They report that for low coverages of iron, the iron forms a nanoparticle array, which transforms into a continuous coverage for increasing amounts of iron. They also report an in-plane magnetic anisotropy for a coverage of above six monolayers.

1.3 Approach

In this study the changes in MoS_2 with the addition of iron has been studied by several experimental techniques. In Justin Wells' XPS laboratory at NTNU, the growth on the surface and the effects annealing of iron on MoS_2 have been studied by the means of X-ray Photoelectron Spectroscopy (XPS), Low Energy Electron Diffraction (LEED) and Ultraviolet Photoelectron Spectroscopy (UPS). XPS has been used to determine the stoichiometry of the sample, thickness and quality of the overlayer and if iron intercalates. LEED has been used to determine the crystalline quality of the sample, whereas UPS has been used to see the changes in the valence band. A preliminary study by Angle-Resolved Photoelectron Spectroscopy (ARPES) was carried out at Philip King's laboratory in St. Andrews in Scotland, to map out how the band structure changes when magnetic impurities are added to the material.

1.4 Structure of the report

The outline of this report is as follows: In chapter 2 the background information and the basic theory for this work will be presented. In chapter 3 the experimental techniques; XPS, UPS, ARPES and LEED will be described. The experimental method with the preparation will be described in chapter 4, and in chapter 5 and 6 the results will be presented and discussed. Lastly in chapter 7 a conclusion will be drawn, and further work will be discussed.

2 Theory

In this section a brief introduction to the material in question will be presented. Then it will be explained how this non-magnetic crystal can be spin polarized even though it is bulk inversion symmetric. To motivate the experiment it will be elaborated how magnetism could influence the band structure of the material. Lastly a presentation of crystal growth modes and intercalation will be discussed.

2.1 MoS_2

Molybdenum disulfide is an inorganic compound consisting of the two elements, molybdenum and sulfur. It forms natural crystals of two different polymorphs, the 2H and the 3R, where the former is the most abundant in nature and the one studied in this thesis. A natural MoS_2 crystal is shown in Figure 2.1.

Figure 2.1: MoS_2 crystal. The crystal has large crystal domains and forms in a layered structure. Picture taken from Ref.[17].

The hexagonal crystal structure 2H-polymorph is shown in Figure 2.2. The unit cell consists of two sandwiches of S-Mo-S, which makes 2H-MoS_2 a bi-layered material. The unit cell has an in-plane lattice constant $a = 3.16$ Å and an out-of-plane lattice constant $c = 12.29$ Å [18]. The S atoms are strongly bonded with Mo, but between the layers the bonding between the S atoms are weak van der Waals forces. This is a weak plane in the crystal, and if the crystal is cleaved, it will most likely break one of the S-S-bonds.

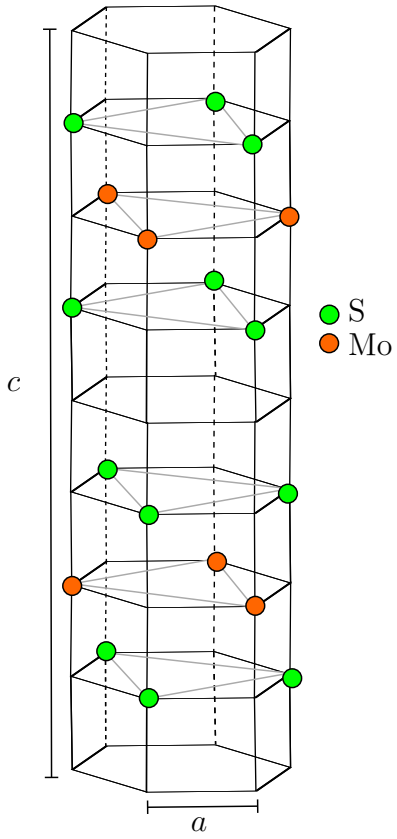

Figure 2.2: The unit cell crystal structure of 2H-MoS_2. Figure adapted from Ref.[19].

The reciprocal lattice of the 2H-MoS_2 polymorph is shown in Figure 2.3. The reciprocal lattice is the Fourier transform of the real space lattice. In electronic structure measurements the density of single-particle electronic excitations in the reciprocal space in a solid is measured. Reciprocal space is often mentioned as momentum space, as the Fourier transform of position is momentum. Figure 2.3 represents the first Brillouin zone (1BZ), and its dimension is described by reciprocal lattice vectors of dimensions $a^* = \frac{2\pi}{a}$ and $c^* = \frac{2\pi}{c}$. In Figure 2.3, the high symmetry points are depicted. These are points in reciprocal space that are more symmetrical than others, meaning that one or more symmetry operations can be carried out on them.

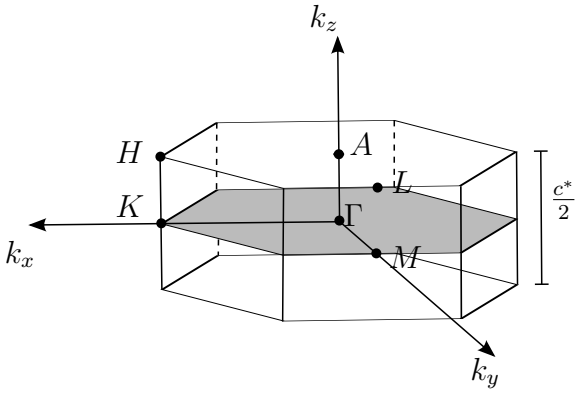

Figure 2.3: The first Brillouin zone (1BZ) of a hexagonal close-packed (hcp) structure.

Often in electronic structure measurements the electronic structure of the surface is probed. At the surface the out-of-plane direction is broken, which results in the Brillouin zone being reduced from a 3D zone to a 2D zone. In Figure 2.4 the new 2D Brillouin zone is depicted with the new high symmetry points depicted with a bar over. Here $\bar{K}$ and $\bar{K}'$ are not the same points. At the surface only one monolayer may be probed, depending on the mean free path of the electrons. Judging from Figure 2.2, the complete unit cell belongs to the D_{6h} point group. It has six-fold rotation symmetry, six mirror planes and inversion symmetry. In one monolayer the symmetry is reduced. The monolayer has only three-fold rotation symmetry and no inversion symmetry, and belongs in the D_{3h} point group. Because of this is $\bar{K}$ and $\bar{K}'$ not the same high symmetry points.

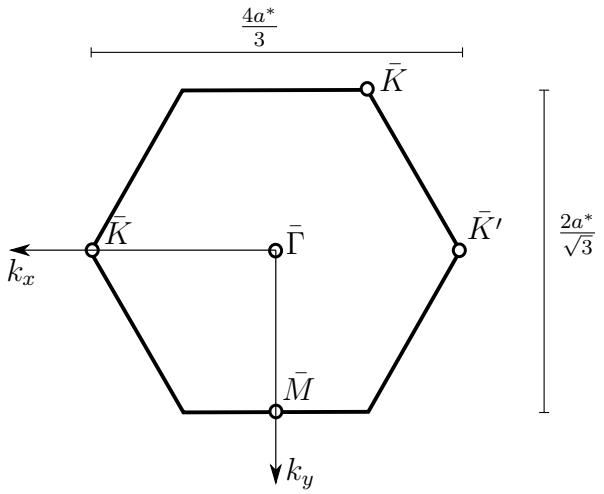

Figure 2.4: The surface Brillouin zone of MoS_2 where $\bar{K}$, $\bar{K}'$, $\bar{\Gamma}$ and $\bar{M}$ are high symmetry points. The surface high symmetry points are depicted with a bar, to distinguish between the bulk high symmetry points and the surface high symmetry points.

2.2 Spin polarized band structure

The band structure of MoS_2 is spin polarized as described in Figure 2.5. The band structure of the full unit cell is not spin polarized, but if one monolayer is probed the band structure is spin polarized. This is due to spin-orbit coupling.

There are several examples of spin orbit coupling in solids. In the presence of an external magnetic field, the electronic band structure splits by the Zeeman effect, and in the presence of an external electric field it splits by the Stark effect [20]. In the presence of an external magnetic field, time reversal symmetry is broken, and it is therefore possible to spin polarize the energy bands. Since MoS_2 is non-magnetic the spin polarization must come from somewhere else. The spin splitting in MoS_2 is due to a local breaking of inversion symmetry and a strong dipole field within the crystal.

In most crystals inversion symmetry is preserved. This means for an energy state E at a position $\boldsymbol{k}$ in reciprocal space with a spin $\uparrow$ will have counterpart at $-\boldsymbol{k}$ described by

$$E(\boldsymbol{k}, \uparrow) = E(-\boldsymbol{k}, \uparrow). \tag{2.1}$$

For the same state time reversal symmetry will lead to

$$E(\boldsymbol{k}, \uparrow) = E(-\boldsymbol{k}, \downarrow). \tag{2.2}$$

Combining these leads to Kramers relation

$$E(\boldsymbol{k}, \uparrow) = E(\boldsymbol{k}, \downarrow), \tag{2.3}$$

that every point in the Brillouin zone is spin degenerate. Since in MoS_2 there is a local inversion symmetry breaking in each layer equation (2.3) does not hold, and the bands will spin polarize as in Figure 2.5.

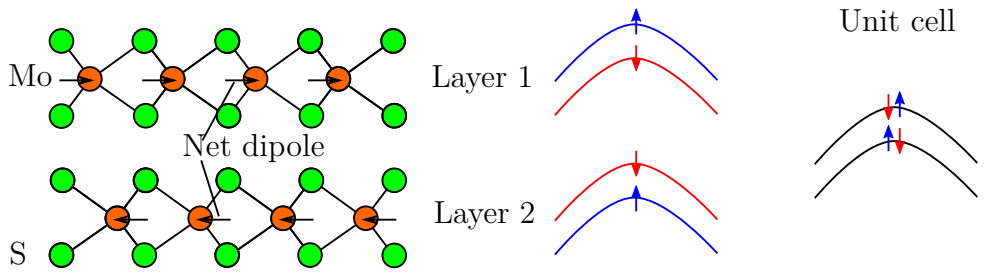

Figure 2.5: The unit cell structure of MoS_2 from the side, two monolayers stacked along the c axis, rotated in-plane 180° from each other. This results in a net dipole moment in each of the monolayers. At an arbitrary spin-polarized point if layer 1 has a spin-configuration will layer 2 have the opposite spin-configuration. The unit cell band structure will be an average over these, and will be spin degenerate.

How the bands will spin polarize comes from the spin orbit interaction, that enters into the Hamiltonian through the Dirac equation. In the non-relativistic limit of the Dirac equation this gives rise to the Pauli Spin Orbit term

$$H' = -\frac{\hbar}{4m_0^2c^2}\boldsymbol{\sigma} \cdot \boldsymbol{p} \times (\nabla V_0) \tag{2.4}$$

where $\hbar$ is Planck's constant, m_0 is the mass of a free electron, c is the speed of light, $\boldsymbol{p}$ is the momentum operator, V_0 is the Coulomb potential of the atomic core, and $\boldsymbol{\sigma} = (\sigma_x, \sigma_y, \sigma_z)$ is the vector of the Pauli spin matrices [21].

The first order manifestation of this response in an inversion asymmetric system with an out-of-plane electric field is know as the Rashba effect. The Rashba effect is given by

$$H' = \alpha(\boldsymbol{k} \times \boldsymbol{\sigma}) \cdot \hat{z} \tag{2.5}$$

where α is defined as the Rashba parameter and $\boldsymbol{k}$ is the wave vector defined through $\boldsymbol{p} = \hbar\boldsymbol{k}$. For a 2D system with $\boldsymbol{k} = (k_x, k_y, 0)$, the Rasbha effect will give a relation

$$H' = \alpha(k_x\sigma_y - k_y\sigma_x). \tag{2.6}$$

If this now is taken to influence an electronic band dispersion by the free electron model, the Rasbha effect will in 2D give an electronic dispersion

$$E(k_x, k_y) = \frac{\hbar^2}{2m}(k_x^2 + k_y^2) + \alpha(\pm|k_x| \pm |k_y|). \tag{2.7}$$

This dispersion is sketched in Figure 2.6, showing that the two bands will be shifted from another, and have in-plane spins pointing in a vortex structure.

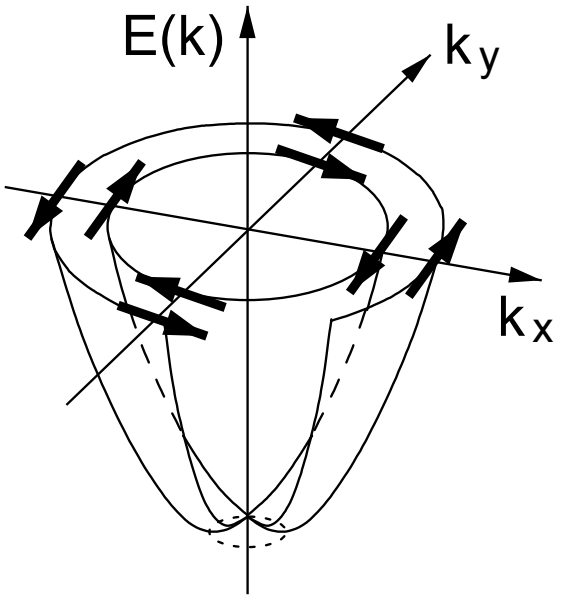

Figure 2.6: Qualitative sketch of the spin-split dispersion $E(k)$ by Rashba splitting in 2D. Arrows indicate the spin orientation. Figure taken from Ref.[21].

For TMDCs like MoS_2 it has been observed that the spin polarization is primarily out-of-plane[2, 3], and the Rashba effect is not the primary effect. This is caused by an in-plane dipole through the center of each layer, as seen in Figure 2.5. Thus higher order terms have to be considered for the spin orbit coupling. The third order term for the D_{3h} point group [22]

$$H^{(3)}(k) = \nu_k(k_x\sigma_y - k_y\sigma_x) + \lambda_k(3k_x^2 - k_y^2)k_y\sigma_z, \tag{2.8}$$

where $k = \sqrt{k_x^2 + k_y^2}$, $\nu_k = \nu(1 + \alpha k^2)$, σ_i is the Pauli matrices and λ_k is the warping parameter. In this equation the first part as the Rashba effect that will cause an in-plane spin, while the second part will cause an out-of-plane spin. The mirror plane through the center of the monolayer suppresses the out-of-plane field, and this leads to a strong out-of-plane spin polarization. From this third order interaction will the strength of the out-of-plane spin polarization develop as in Figure 2.7 [22]. A full understanding of the spin polarization of the band structure in MoS_2 is not yet acquired, and even higher order terms may interact. For a more elaborate description of how bands in TMDCs spin polarize, please consider my project thesis [23].

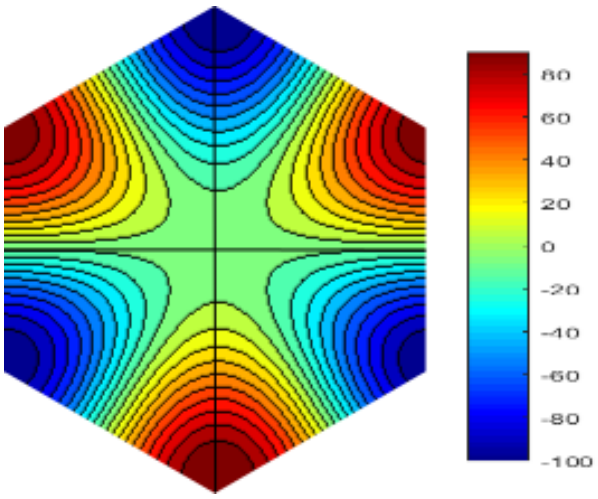

Figure 2.7: Sketch of how the out-of-plane spin polarization behaves in MoS_2. The hexagon represents 1BZ of a hexagonal crystal, where $\bar{K}$ is found in the corners and $\bar{\Gamma}$ is in the center. Red indicates a positive spin polarization and blue a negative spin polarization.

2.3 Influence of a magnetic field on the band structure

How an external magnetic field influences the band structure is quite complicated. The Zeeman effect will split the energy bands into spin polarized energy bands. An external magnetic field lifts time reversal symmetry, so that a finite Zeeman energy splitting $\Delta E = g^*\mu_B B$ can be obtained, where g^* is the effective g factor and μ_B is the Bohr magneton of the electron hole state. For a 2D system there are invariants for the in-plane and perpendicular components $\boldsymbol{B}_{||} = (B_x, B_y, 0)$ and B_z [24]. The Hamiltonian for Zeeman splitting is

$$H = \frac{g_{||}}{2}\mu_B(B_x\sigma_x + B_y\sigma_y) + \frac{g_z}{2}\mu_B B_z\sigma_z, \tag{2.9}$$

where $g_{||}$ and g_z are the effective g-factors in the parallel and perpendicular direction.

If an out-of-plane magnetic field influences the already spin split band structure of MoS_2, this will behave as in Figure 2.8 at the $\bar{K}$ and $\bar{K}'$ point. The bands with their spins in the direction of the field will have their energy increased by $\frac{g_z}{2}\mu_B B_z$, and the bands with opposite spin will have their energy decreased by the same amount. This will enlarge the gap at $\bar{K}$, and shrink the gap at $\bar{K}'$. This is of course if the bands are spin-polarized. If the full unit cell is probed, the bands are spin degenerate, and each band will split in two like in Figure 2.8. For parts of the bandstructure away from $\bar{K}(\bar{K}')$, the bands are less spin polarized. For these bands there will be a splitting where there will be a higher density of states for the band initially polarized parallel to the field. Parts of the band structure with spin polarization perpendicular to the field will be unaffected.

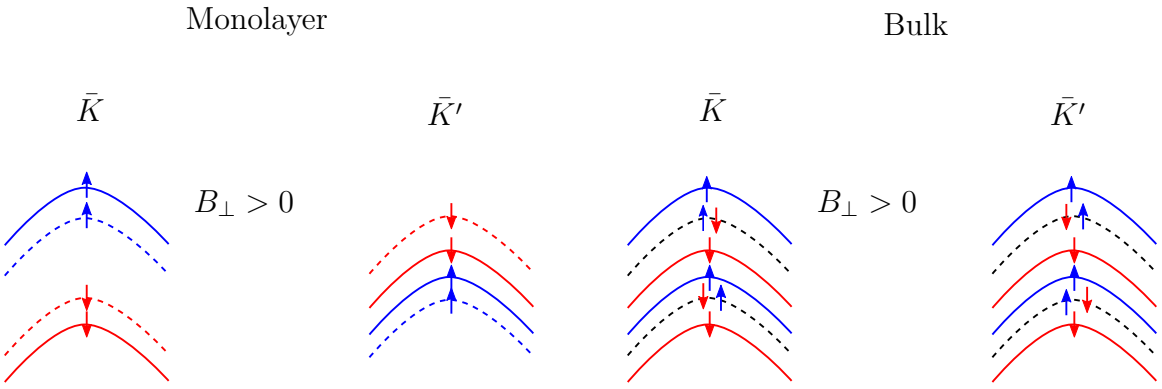

Figure 2.8: Perturbation at the $\bar{K}(\bar{K}')$-point in a out-of-plane magnetic field. Dotted lines are $B = 0$, and full lines are $B_\perp > 0$

An in-plane magnetic field will have a different effect on the band structure than an out-of-plane field. For the spin degenerate bands these will have a similar energy splitting as for an out-of-plane field, dependent on the asymmetry in the effective g-factor. At $\bar{K}(\bar{K}')$ Ref.[6, 25, 26] has found that the out-of-plane spin is protected by the inversion symmetry, and it would require a very large field to align the spin with the field. Thus their energy will not be affected in an in-plane magnetic field, since they are orthogonal to the field. In-plane spin polarized parts of the band structure will have their energy changed respectively as the out-of-plane spin polarized states in an out-of-plane field.

Such Zeeman splitting has been realised experimentally on several TMDCs by applying an external magnetic field[27–29]. They report a shift of around 0.1-0.2 meV/T. The energy resolution of the ARPES system used is of the order of 3-10 meV, and thus large field strengths are required. This cannot be achieved by magnetic doping, and such high fields would obstruct the detection of the photoelectrons.

The magnetic field will also split the energy levels into a set of magnetic sub-bands (Landau levels). If this is applied on the free electron model, these levels will be separated by the cyclotron frequency, with energies given by

$$E_n = (n + \frac{1}{2})\hbar\omega_c + \frac{\hbar^2 k_{||}^2}{2m^*} \tag{2.10}$$

where $\omega_c = eB/m^*$ is the cyclotron frequency where $m*$ is the effective mass of the electron and $k_{||}$ is the component of the wavevector parallel to the magnetic field. If Zeeman splitting occurs, each Landau level splits up into pairs, one for spin up and one for spin down.

If magnetic impurities substitutionally dope into the crystal structure, it is far more difficult to predict how it will change the band structure. Several theoretical/numerical investigations of iron doping in both bulk and monolayer MoS_2 has been carried out [12, 30–33]. In Ref.[33] they show that for different situations of iron doping, the compound will show both a p-type semiconducting character and a metallic character with n-type conductivity with spin polarization appearing. In Ref.[12] they predict the magnetic properties of monolayer MoS_2, and support iron as a promising element for making MoS_2 a dilute magnetic semiconductor.

2.4 Thin film growth

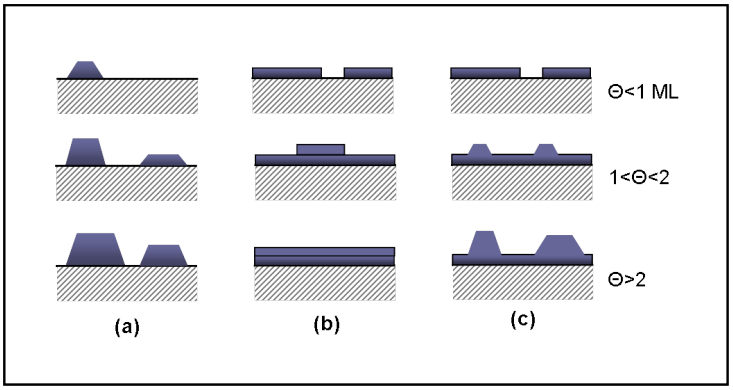

Figure 2.9: Cross-section of the three primary modes of thin film growth. (a) Volmer-Weber, (b) Frank-van der Merwe and (c) Stranski-Krastanov. Figure taken from Ref.[34].

As illustrated in Figure 2.9, in thin film growth there are three primary models for thin films to grow at a crystal surface or interface. How a thin film will grow on a surface depends on interaction strength between the adatoms and the surface. In Volmer-Weber growth, the interaction between the adatoms is stronger than that of the adatom and the surface, and this leads to the formation of three-dimensional structures of islands and clusters on the surface. With this kind of growth the surface will be rough and multilayered. On the other hand in Frank-van der Merwe growth, the adatoms attach preferentially to surface sites and thus makes a smooth surface. This then starts a layer by layer growth where the growth of one layer is completed before the growth of the next starts. Stranski-Krastanov growth is a process that is a combination of the other two growth modes. At first the growth of the thin film grows layer by layer, but at a critical thickness islands starts to form. [35]

2.5 Intercalation

Intercalation refers to the reversible insertion of a molecule or an ion into a layered structure. There are many examples of intercalation, for example in graphite, transition metal dichalcogenides, zeolites, etc. In intercalation the intercalant prefers to take up the space in the van der Waals gap between the layers of layered a compound, expanding the gap between the sheets. The resulting material, the intercalation compound, can have completely different properties from the pure material. For instance intercalation of Ca in graphite is known to introduce superconductivity [36]. Intercalation can be achieved in many different ways: by adding the guest species during synthesis, by diffusion from vapour or liquid phase into the sample or electrochemically. For *in situ* vacuum measurements the desired intercalant can be evaporated on top of the surface of the sample, and thereby intercalate into the compound. In Figure 2.10 a sketch of how intercalation could be in MoS_2 is shown. [37]

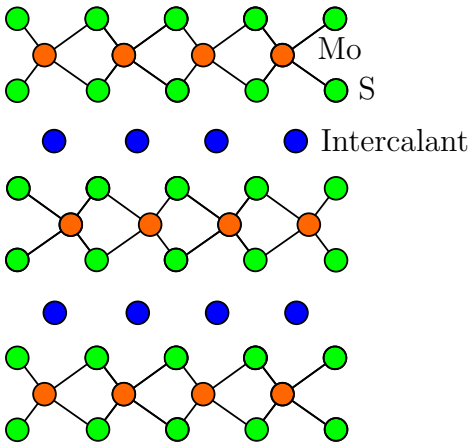

Figure 2.10: Sketch of intercalation in MoS_2. The figure shows a cut through the side in the crystal lattice of 2H-MoS_2, where an intercalant has intercalated into the van der Waals gap between the layers in the crystal structure.

3 Experimental Techniques

In this chapter the experimental techniques used in this work will be described. First a general description of photoemission will be outlined. Then a general description of how an X-ray Photoemission Spectroscopy (XPS) spectrum can be interpreted, analysed and used to determine layer thickness will be described. Then a description of Angle-Resolved Photoemission Spectroscopy (ARPES) will be outlined. Lastly a short description of Low Energy Electron Diffraction (LEED) and how to achieve Ultra High Vacuum (UHV) conditions. Unless something else is stated are the main sources for section 3.1 and 3.2 Ref.[38], Ref.[39, 40] for section 3.3 and for section 3.4 and for section 3.5 Ref.[41].

3.1 Photoelectron spectroscopy (PES)

Photoelectron spectroscopy (PES) is a surface sensitive quantitative technique that utilizes the photoelectric effect. The spectrum is obtained by irradiating the sample with light while simultaneously measuring the kinetic energy and the number of photoelectrons ejected from the sample. The technique was developed by Kai Siegbahn's research group in Uppsala in the 1960s[42, 43], and the technique was first coined with the name Electron Spectroscopy for Chemical Analysis (ESCA). The technique was first used for chemical analysis, but further development of photoemission techniques proved as just as interesting in physics as well as chemistry.

Depending on the energy range there are different names for photoelectron spectroscopy techniques, and different features that can be examined. X-ray photoelectron spectroscopy (XPS) utilizes X-rays to look at the core levels in a sample, while ultraviolet photoelectron spectroscopy (UPS) utilizes ultraviolet light to determine the molecular orbitals in the valence region. Angle resolved photoelectron spectroscopy (ARPES) utilizes that an electron's momentum is coupled with the angle it exits the sample to map out the electronic structure of the valence band. Photoemission electron microscopy (PEEM) use the emitted photoelectron and local variations in electron emission to generate image contrast. Moreover X-ray photoelectron diffraction utilizes the diffraction conditions for different elements and energies to discover the structure of specific elements in a sample. There is even a wider variety of PES techniques, and in this work XPS, UPS and ARPES have been used to develop a further understanding of the sample.

3.1.1 Basic principles

The basic principle of PES is that an incident photon is absorbed in the sample, and the absorbed energy ejects an electron from one of the atomic orbitals or the valence band,

which is collected by an electron analyser where the kinetic energy is detected. Several attempts have been made to make a theoretical model for the process. The process is often described by a three-step model, even though no separation like this can exist. First the incident beam excites the electron from the initial state to the final state, the electron then travels through the crystal towards the surface and at the surface the electron escapes into vacuum.

The energetics of this process can be described as in Figure 3.1. When a sample is irradiated with photons, the energy is conserved, such that

$$E_B = h\nu - \Phi_S - E_{\text{kin}}, \tag{3.1}$$

where E_{kin} is the kinetic energy of the ejected photoelectron, $h\nu$ is the energy of the incoming photon and Φ_s is the sample work function. E_B is the binding energy of the electron, the energy difference between the initial state and the final state.

In PES experiments the electron analyzer and the sample are electrically grounded, hence their Fermi levels will be aligned. As can be seen in Figure 3.1 the work function of the sample and the electron analyser may be different. The binding energy of the emitted photoelectron is defined to the Fermi level, so that zero binding energy is at the Fermi level. This means that it is the analyzer work function Φ_A, that must known correctly and not the sample's, Φ_S. The energetics of the process is hence given by

$$E_B = h\nu - \Phi_A - E_{\text{kin}}. \tag{3.2}$$

The analyser work function is a known quantity, that is determined by analysing standard samples prior to the experiments.

3.1.2 Experimental setup

Typically in a photoemission experiment is the kinetic energy of the emitted electrons detected by a hemispherical analyser. A schematic of a photoemission experiment is sketched in Figure 3.2. Photons from a source are directed towards a sample, and these cause photoelectrons to be emitted from the sample. These are collected into the electrostatic lenses where they are energy-selected and focused into the entrance slit of the hemisphere. In the hemisphere the electrons are selected by their kinetic energy. Only those electrons within the right pass energy range will hit the detector. This is done by setting the two concentric spheres at a different potential, causing there to be an electric field. The electrons that have too high kinetic energy will hit the outer hemisphere, and those electrons that are travelling with a lower kinetic energy will hit the inner hemisphere.

To detect the electrons two different systems have been used, a channeltron detector and a 2D detector consisting of a multichannel plate connected to a phosphorus screen. The reason for why these two have been used will become clear in the upcoming ARPES section. In the 2D detector the electrons first hit a microchannel plate where this causes a cascade of electrons amplifying the original signal. The electrons then impact on a fluorescent screen which is coupled with a CCD-camera that detects the intensity of

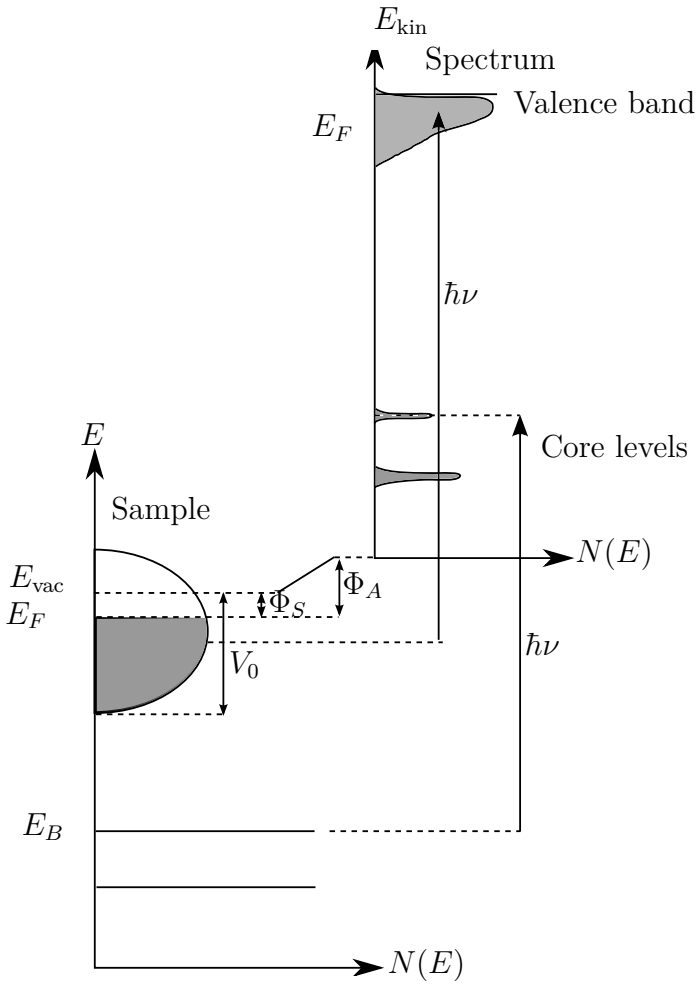

Figure 3.1: The energetics of the photoemission process. The right side show the electron energy distribution produced by the incoming photons, and measured as a function of the kinetic energy E_{kin} of the photoelectrons. The binding energy E_B is more convenient when referring to the energy levels in a solid. In the left it is shown how the binding energy E_B relates to the kinetic energy E_{kin}, where E_B =0 at E_F. Figure adapted from Ref.[38, 39].

fluorescence on the screen. In the channeltron detector there is a set of electron multipliers in a line causing a similar cascade as in the microchannel plate. These channels are at different potential, and by measuring the resistance of these channeltrons the intensity of the incoming electrons is observed.

The energy resolution $\Delta E_{\text{measured}}$ of an PES experiment is given by

$$\Delta E_{\text{measured}} = \sqrt{\Delta E^2_{\text{source}} + \Delta E^2_{\text{analyser}} + \Delta E^2_{\text{sample}}} \tag{3.3}$$

where ΔE_{source} is the resolution of the photon source, $\Delta E_{\text{analyser}}$ is the resolution of the analyser and ΔE_{sample} is the sample contribution to the broadening. The energy resolution of the analyser is dependent upon the pass energy E_{pass}, and the physical size of the analyser

$$\Delta E = E_{\text{pass}}\left(\frac{R_1 R_2}{2R_0 + \alpha^2}\right). \tag{3.4}$$

where R_1 is the inner radius of the analyser, R_2 is the outer radius of the analyser, R_0 is the radius to the center of the analyser and α is the angular half aperture of the entrance slit. The analyser in XPS laboratory at NTNU is a SPECS Phoibos 150 analyser and the energy resolution for this scales as [44]

$$\frac{\Delta E_{\text{analyser}}}{E_{\text{pass}}} \approx 0.01. \tag{3.5}$$

In St. Andrews the larger SPECS Phoibos 225 was used, which yields an even better energy resolution.

The sample uncertainty ΔE_{sample} is limited by the thermal broadening. At room temperature this scales as $E \sim 4.4 k_B T \approx 0.11\text{eV}$, and can generally be neglected. The main uncertainty is the source, and will be described later for the respective sections.

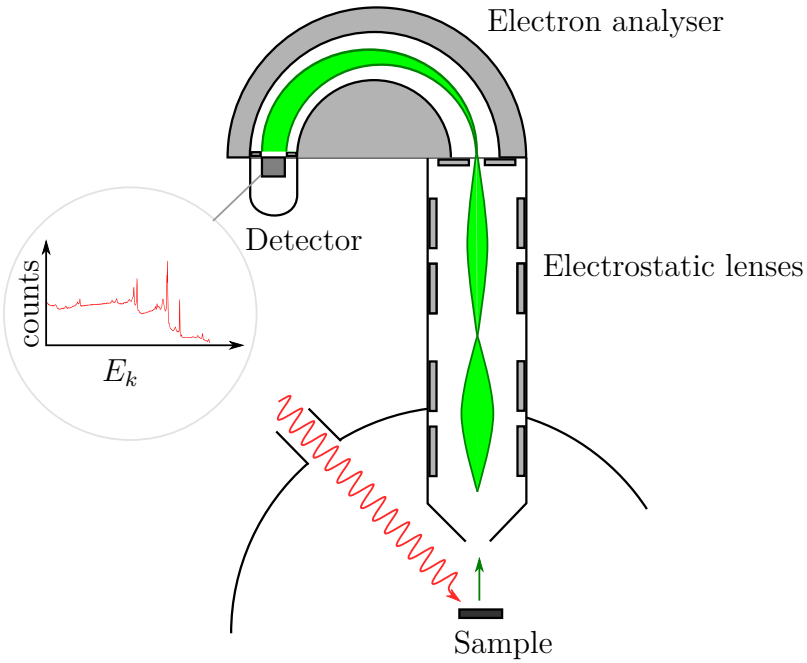

Figure 3.2: Sketch of photoelectron detection by a hemispherical analyser. An incoming photon directed towards a sample causes photoemission. This emits an electron that is collected by the analyser, where electrostatic lenses focus the electrons into the entrance slit of the analyser. In the analyser the electrons are energy filtered by an electric field between two concentric spheres, and those with the correct pass energy are allowed to hit the detector where they are detected.

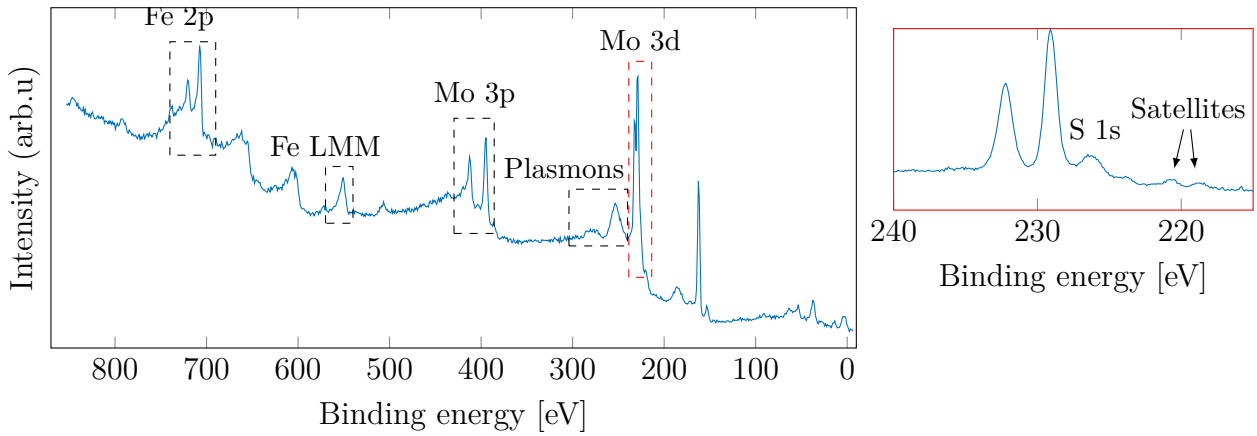

Figure 3.3: A widescan of a MoS_2 sample with an iron overlayer. The figure shows the different features of an XPS spectrum. The core level emissions are depicted by the element and orbital they are emitted from, an Auger peak is depicted as well as the plasmon losses of the Mo 3d peak. A zoomed in higher resolution scan of the Mo 3d peaks in the red box is added to highlight the satellite peaks.

3.2 X-ray photoemission spectroscopy (XPS)

3.2.1 Features of an XPS spectrum

In Figure 3.3 a widescan of an XPS measurement is shown. An XPS spectrum shows a wide array of features. In addition to the elemental orbital transition peaks; Auger-peaks, satellites and plasmon peaks can be found in the spectrum. In addition several loss mechanisms result in a background to the spectrum that has to be taken into account in order to analyse.

Satellite peaks come as a result that a monochromatic light is not being employed in the measurements. This means that other transitions in the anode material might cause excitations in the sample. As the photon energy is changed in equation (3.1), this results that a replica of the peak will be found at a constant energy away from the original peak. "Ghost peaks" are quite similar to satellite peaks. A "ghost peak" comes from photons excited by a contaminant on the anode material. Typically oxygen may reside on the anode material, causing X-rays from transitions in oxygen to be emitted.

Auger peaks are a result of a related mechanism to photoemission, as can be seen in Figure 3.4. An electron from the L_1 orbital relaxes into the K orbital. The energy release from this transition results in an electron in the $L_{2,3}$ orbital being ejected into vacuum. This is a competing effect with photoemission and can also be employed to extract spectroscopic information about a material. The technique is named as Auger Electron Spectroscopy (AES). For quantification purposes XPS is usually a more precise technique.

Electrons in the sample may also undergo inelastic collisions as they are emitted from the sample, and thus altering the energy of the recorded electrons. These energy loss processes results in a background from the electronic states other than the characteristic energies for the photoelectric lines. The shape of the background takes a character determined by a probability distribution of the states undergoing some modification of their initial

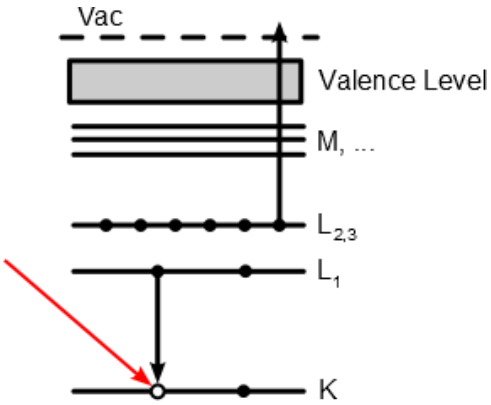

Figure 3.4: Sketch of an Auger process. An incoming X-ray or electron (red arrow) causes a vacancy in the K orbital that results in a transition of an electron from the L_1 to the K orbital. The energy release of this process results in an electron from the $L_{2,3}$ being emitted. Figure taken from Ref.[45].

value. In some materials these inelastic loss mechanism can be identified as plasmon loss peaks. These occur due to quantised oscillations in the valence electrons or free electrons in metals. This can be an intrinsic effect, as the photoemission process is happening a core-hole is formed, this can result in a coupling between the core-hole and the oscillations of the valence states. This will be observed as a photoelectron peak with less energy than the main peak. Since the oscillations are different in the surface state and bulk state, there is difference between surface plasmon and bulk plasmon losses. Extrinsically this can happen as the photoelectrons may scatter with free electrons with discrete energy bands, which form loss distributions of relatively narrow structures.

Spin-orbit splitting

As seen in Figure 3.3 the Mo 3d core level is split into two peaks. This is due to spin-orbit splitting. This is a consequence of the orbital angular momentum l is coupling with the spin orbital momentum s. The splitting results in a state with total angular momentum given by

$$j = |l \pm s|. \tag{3.6}$$

This happens for all states, except for for the s-subshell, and must be taken into account in the analysis. The peaks will have specific area ratios based on the degeneracy of each spin state. For example, for a 2p state, where $n = 2$ and $l = 1$, will j be 1/2 and 3/2. The area ratio between these two spin orbit peaks will be 1:2, corresponding to 2 electrons in the $2p_{1/2}$ and 4 electrons in $2p_{3/2}$. Table 3.1 shows the area ratio of the different subshells. The peaks will split with a fixed energy, that can be found in tables.

3.2.2 Analysis

There are two merits of the analysis of XPS data. It is both a neat method for analysing samples qualitatively and quantitatively. Qualitatively it is a non-destructive way of

Table 3.1: Spin-orbit splitting j values and peak area ratios for the respective subshells

Subshell	j	Area ratio
s	1/2	n/a
p	1/2 3/2	1:2
d	3/2 5/2	2:3
f	5/2 7/2	3:4

identifying the components of a sample. By comparing a spectrum like the one seen in Figure 3.3 with databases, the different species in the sample can be identified. More accurately the binding energy of the peak tells what kind of bonds the elements have with each other, and will thus give a good identification of the chemistry in the surface region of the sample.

To understand the sampling depth of photoemission the inelastic mean free path λ have to be introduced. This is the mean free path the electrons travel before losing energy. For most elements the inelastic mean free path seem to be following a universal curve, as shown in Figure 3.5. In this work the inelastic mean free path used has been calculated using the QUASES IMFP[46], that calculates the inelastic mean free path by the TPP-2M formula[47].

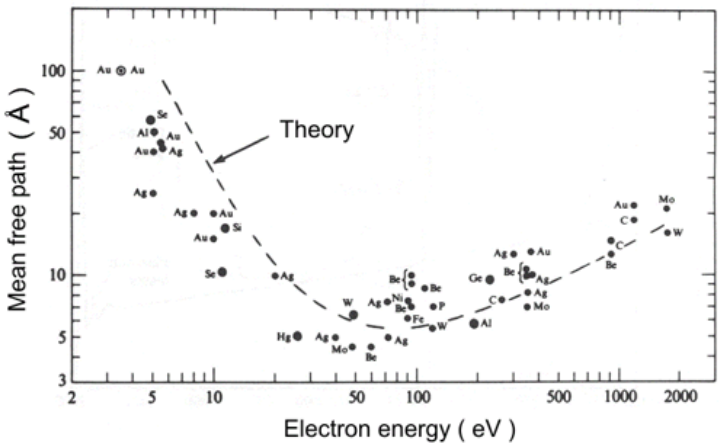

Figure 3.5: "Universal curve" of mean free path. The broken line is the theoretical curve described by equation (5) in [48] and the points are measured dependence of inelastic mean free path. Figure taken from Ref.[49]

By employing the inelastic mean free path, the detected intensity I_S of electrons emitted at an depth d will have their intensity I_0 attenuated according to the Beer-Lambert law

$$I_S = I_0 e^{-d/\lambda}. \tag{3.7}$$

Electrons will be emitted at all depths, but at a certain depth it is more likely that intensity is too attenuated. The sampling depth of XPS is defined as the depth at which 95% of all photoelectrons are scattered by the time they reach the surface, this depth is 3λ. For most elements with a Al K_α source, λ is in the range of 1 - 3.5 nm. A monolayer

of a material is typically about 0.3 nm, thus making XPS sensitive to about the 10-30 first layers of a material.

The measured intensity of an XPS experiment is

$$dI_{\text{measured}} = N_k(x,y,z)\sigma_k \exp\left(\frac{-z}{\lambda_k \cos\theta}\right) T\Omega(E_k,x,y,z)D_0 dxdydz \tag{3.8}$$

where T incident X-ray flux, $N_k(x,y,z)$ is the number of atoms(molecules), Ω is the acceptance solid angle of the electron analyser, σ_k is the photoelectric cross section and D_0 is the instrument detection efficiency. During the course of an experiment the last three terms usually remain constant, as they are instrumental, and would under normal conditions not change. Whereas the first three could potentially change and are the ones of interest. By assuming that the sample is homogeneous, equation (3.8) can be simplified and the intensity of the peak is given by

$$I = \rho\sigma\lambda K \tag{3.9}$$

where K is all the instrumental factors. The atomic percentage X_j of an element j can then be expressed as

$$X_j = \frac{I_j/(\sigma_j\lambda_j)}{\sum_i I_i/(\sigma_i\lambda_i)} \cdot 100\%. \tag{3.10}$$

Line shape

The line shape of a photoemission experiment might be complicated, and different species in a sample may have emitted photoelectrons in the same energy range. To separate this information curve fitting with an assumption of a peak shape is employed. A symmetrical line shape in a photoemission experiment can be described by a Voigt function. A Voigt function

$$V(x;\alpha,\gamma) = \int_{-\infty}^{\infty} G(x';\alpha)L(x-x';\gamma)dx' \tag{3.11}$$

is a convolution between a Gaussian function

$$G(x;\alpha) \equiv \frac{e^{-x^2/(2\alpha^2)}}{\alpha\sqrt{2\pi}} \tag{3.12}$$

and a Lorentzian function

$$L(x;\gamma) \equiv \frac{\gamma}{\pi(x^2+\gamma^2)}, \tag{3.13}$$

where α and γ are the width of the Gaussian and Lorentzian respectively. The Lorentzian function enters into the photoemission experiment due to lifetime broadening of the atomic

orbital. The Gaussian enters through the experimental setup and phonon broadening due to temperature.

Background

Due to inelastically scattered electrons, the spectrum is found on a background. In the analysis this background has to be taken into account. Several models for backgrounds are being used for photoemission experiments, and there is a skill to understand when to use the correct background. The most common backgrounds are a linear function, the Shirley background[50] and the Tougaard background [51]. For this work the Shirley background has been used. The Shirley background assumes that the background arises solely from inelastic scattering of electrons of higher kinetic energy, and is proportional to the integrated photoelectron intensity to higher kinetic energy.

3.2.3 Angle-resolved XPS

By utilizing that the sensitivity to the bulk and the surface changes when the emission angle from the sample is changed, depth profiling of films on the surface of a substrate can be performed non-destructive with XPS [52]. The mathematical outline starts with Beer-Lambert law in equation (3.7). As can be seen in Figure 3.6 different detection angle changes the surface sensitivity in the sample, and Beer-Lambert law has to be changed to

$$I = I^{\infty} \exp\left(-t/\lambda \cos\theta\right), \tag{3.14}$$

where I^{∞} involves all the sensitivity factors for the sample. Here λ needs to be redefined to be the elastic attenuation length (EAL). For most purposes the IMFP and EAL can be used interchangeably, but for the following equation the EAL should be used. Whereas IMFP only include inelastic collisions, the EAL includes elastic collisions as well. In this work EAL has been calculated from theory by NIST EAL database[53].

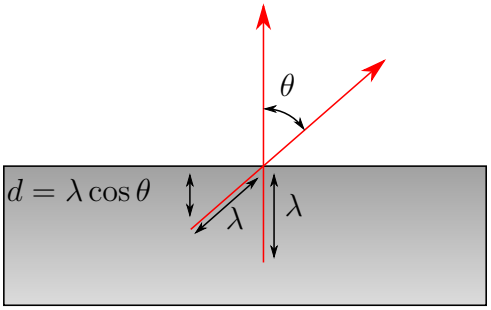

Figure 3.6: Sketch of how the depth dependence changes as the emission angle is changed. If an electron at normal emission is coming from an depth λ, will the electron be coming from a depth $d = \lambda \cos\theta$ at if the detection angle is changed to θ.

Consider now a two layered material with a thin top layer of a material A on a substrate B. The intensity I_A from the top layer is the integration between 0 and d and becomes

$$I_A = I_A^\infty[1 - \exp(-d/\lambda_{A,A}\cos\theta)]. \tag{3.15}$$

Whereas the signal from the substrate arriving at the interface between A and B has the intensity I_B^∞, and passing through layer A this is attenuated giving the intensity

$$I_B = I_B^\infty \exp(-d/\lambda_{B,A}\cos\theta). \tag{3.16}$$

$\lambda_{i,j}$ is defined as the effective attenuation length of a signal i through a material j. The ratio of these intensities give

$$\frac{I_A}{I_B} = \frac{I_A^\infty[1 - \exp(-d/\lambda_{A,A}\cos\theta)]}{I_B^\infty \exp(-d/\lambda_{B,A}\cos\theta)}, \tag{3.17}$$

where

$$\frac{I_A^\infty}{I_B^\infty} = \frac{N_A\sigma_A\lambda_{A,A}T_A}{N_B\sigma_B\lambda_{B,B}T_B}. \tag{3.18}$$

Agglomeration/intercalation model

The growth on a surface can often be quite complicated, and the evolution of a layer on the surface can develop in many different ways. Intercalation can be the one case, where the adatoms on the surface diffuse into the structure and lies between the van der Waals gaps. The overlayer does not necessarily need to grow in a layer by layer growth, and can agglomerate on the surface. After heat treatment both of these two cases are likely, and therefore a model for how these will develop in ARXPS is necessary.

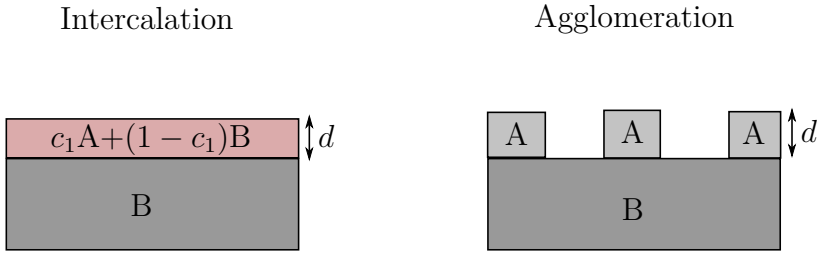

Figure 3.7: Figure showing two model cases for intercalation and agglomeration. For intercalation the top of the sample is a slab of a mixture of A and B, where the concentration of A is c_1. For the agglomeration there are structures on the surface of average height d with a average coverage c_2.

Consider a sample with an overlayer of thickness d_0 of a material A, the sample is modified such that the overlayer migrates into the substrate B. Assuming that A does not desorb this would lead to a conservation $d_0 = c_1 d_1$, where d_1 is the depth the A intercalates into, and c_1 is the concentration of A in this volume. This leads to an intensity from A

$$I_{\mathrm{A}} = I_A^{\infty} c_1 \int_0^{d_1} \exp\left(-x/\lambda \cos\theta\right) \mathrm{d}x = I_A c_1 [1 - \exp\left(-d_1/\lambda_{A,A} \cos\theta\right)] \tag{3.19}$$

and an intensity from B

$$\begin{aligned} I_{\mathrm{B}} &= I_B^{\infty}(1 - c_1) \int_0^{d_1} \exp\left(-x/\lambda \cos\theta\right) \mathrm{d}x + I_B^{\infty} \int_{d_1}^{\infty} \exp\left(-x/\lambda \cos\theta\right) \mathrm{d}x \\ &= I_B^{\infty}(1 - c_1)[1 - \exp\left(-d_1/\lambda_{B,A} \cos\theta\right)] + I_B^{\infty} \exp\left(-d_1/\lambda_{B,A} \cos\theta\right). \end{aligned} \tag{3.20}$$

For agglomeration islands on the surface cover an proportion of the surface area c_2 and have an average height d_2. If the sample modified the conservation of A assuming no desorption is $d_0 = c_2 d_2$. This leads to the observed intensity of A

$$I_{\mathrm{A}} = c_2 I_A^{\infty} \int_0^{d_2} \exp\left(-x/\lambda \cos\theta\right) \mathrm{d}x = I_A c_2 [1 - \exp\left(-d_2/\lambda_{A,A} \cos\theta\right)] \tag{3.21}$$

and for the substrate B

$$\begin{aligned} I_{\mathrm{B}} &= I_B^{\infty}(1 - c_2) \int_0^{\infty} \exp\left(-x/\lambda_{B,B} \cos\theta\right) \mathrm{d}x + c_2 \int_{d_2}^{\infty} \exp\left(-x/\lambda_{A,B} \cos\theta\right) \mathrm{d}x \\ &= (1 - c_2) I_B^{\infty} + c_2 I_B^{\infty} \exp\left(-d_2/\lambda_{A,B} \cos\theta\right). \end{aligned} \tag{3.22}$$

These equations are mathematically the same, if assuming $c_1 = c_2 = c$ and $d_1 = d_2 = d$. This suggest that these two cases would give a similar angle dependent dispersion. Employing this model will extract some useful information about the sample. For example for the case of a low c and a large d, it is unlikely that there has formed a sparse array of pillars on the surface, on the other hand this is a likely situation for intercalation. If d is shorter than the distance to the van der Waals gap from the surface, and c is large it is most likely islands forming on the surface. By fitting this the to acquired ARXPS, is possible to model how the interface between A and B is.

Shadowing effects is neglected in the agglomeration model. This is when an electron emitted normal emission would go through the bare surface, but at an angle off normal emission would travel through an island before being detected. This will affect the signal, but is for simplicity neglected.

ARXPS has its implications. The model assumes that the layers are homogeneous and flat, that the interfaces are abrupt and that the photoelectrons does not show interference effects. This is hard to achieve experiments on layered materials, but still the measurement technique provides valuable information.

Maximum entropy theory

Another way to evaluate how the compositional variations of the sample vary through the sample is the multilayer model. The sample can been separated into layers as seen in Figure 3.8, where each layer has a composition $n_{j,i}$ where all the elements j for each layer

i adds up to one. The attenuation of the intensity from one element in a layer will then be described by

$$T_j(\theta) = \exp\left(-t/\lambda_j \cos\theta\right). \tag{3.23}$$

Adding up this intensity for each layer one ends up with

$$I_j(\theta) = s_j[n_{j,0} + n_{j,1}T_j(\theta) + n_{j,2}T_j(\theta)^2 + ...] \tag{3.24}$$

or

$$I_j(\theta) = k_j \sum_{i=0}^{N} n_{j,i}T_j(\theta)^i. \tag{3.25}$$

Where k_j is the sensitivity for the specific element.

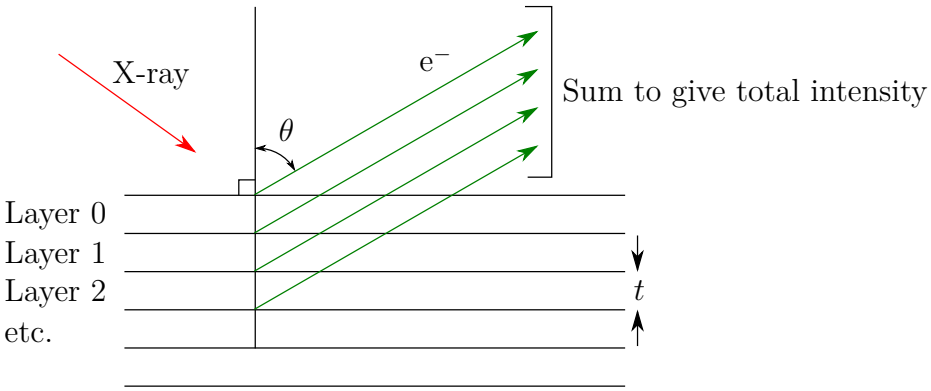

Figure 3.8: The structure used to model the XPS intensity variations in layered samples. Figure adapted from Ref.[54].

In order to fit the model to the acquired ARXPS data, the maximum entropy method [54] can be employed. Briefly the maximum entropy method utilizes an entropy function to evaluate a guess in order get the best fit without overfitting the data. ARXPS data is relatively noisy and the entropy function ensures that the data is fitted with the minimum amount structure required that can be justified by the data. The fit of the data has therefore the minimum information required, the maximum entropy. The entropy function in question for this method is

$$S = \sum_i \sum_j n_{j,i} - m_{j,i} - n_{j,i} \log\left(n_{j,i}/m_{j,i}\right) \tag{3.26}$$

where $n_{j,i}$ is the current guess in the iteration and $m_{j,i}$ is the initial guess. In order to check the quality of the fit the sum of the squares of the errors (χ^2) is calculated according to

$$\chi^2 = \sum_k \frac{(I_k^{\text{calc}} - I_k^{\text{obs}})^2}{\varphi_k^2} \tag{3.27}$$

where φ_k is the standard deviation and k is an iteration variable over the measurement points. The fitting combines these two expressions into a joint probability function

$$Q = \alpha S - \chi^2/2 \tag{3.28}$$

where the maximum is the best fit. α is a regularizing constant, where a large value for α will result in a fit that is too smooth, while a small value will result in overfitting of the data. The fitting works by iterating over a range of different trial profiles and searching for the largest value of Q.

3.2.4 Experimental setup

X-ray gun

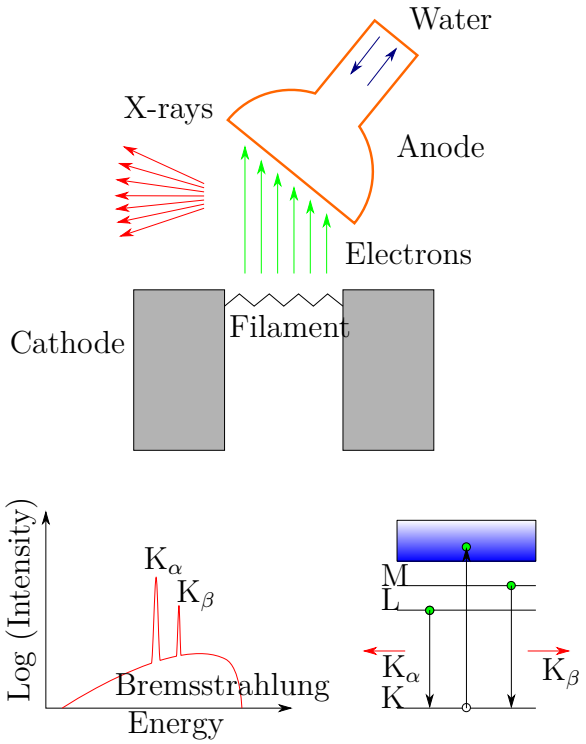

Figure 3.9: X-ray schematic. A heated filament generates electrons that are accelerated towards an anode by an electric field. The energy transfer from the impacting electron causes an electron in the inner orbitals of the anode material to be ejected. Electrons of outer orbitals relaxes into the available state in the inner orbital. This causes X-rays of specific energies to be emitted depending on the anode material. The continuous radiation referred to Bremsstrahlung is the radiation from the electrons being decelerated as they hit the anode material. In order to keep the anode cool water is flown through from the inside. Figure adapted from Ref.[40].

For XPS X-rays needs to be generated, these can either be generated by the principle in Figure 3.9 or by a synchrotron. Electrons are generated in a heated filament, these are accelerated by an electric field between the cathode and towards an anode. In the

anode the electron knocks out an electron from the inner orbitals, and an electron from an outer orbital relaxes into the now empty orbital, and release the energy difference as an X-ray photon. This results in a characteristic spectrum with X-rays emitted with specific energies, as seen in Figure 3.9. The continuous spectrum is generated by the electrons being decelerated as they hit the anode material, this is called Bremsstrahlung (braking-radiation in German). In order to keep the anode cool, water is continuously run through it. In the XPS laboratory at NTNU a twin anode SPECS XR 50 X-ray gun is used. Here there are two separated sides where one is coated with aluminium and the other is coated with magnesium. This gives the option of two different specific emission lines to choose from, Al K_α (1486.9 eV) and Mg K_α (1253.6 eV). For the twin anode the energy resolution of the magnesium source is $\Delta E_{\mathrm{Mg}} = 0.68\mathrm{eV}$ and for the aluminium source $\Delta E_{\mathrm{Al}} = 0.85\mathrm{eV}$ [55].

In St.Andrews a SPECS Focus 500 X-ray monochromator for the X-rays was employed. The principle of this is shown in Figure 3.10. By emitting the X-rays first on a mono-crystalline quartz crystal and employing the diffraction conditions in the crystal, it is possible to direct the X-rays of the desired energy within narrow range towards surface of the sample. The spectrum from this kind of setup will not have the problem with satellite peaks and will have narrower energy uncertainty. On the other hand a lot of the intensity from X-ray source is thrown away in the diffraction leading to longer acquisitions in order to achieve the same signal to noise ratio.

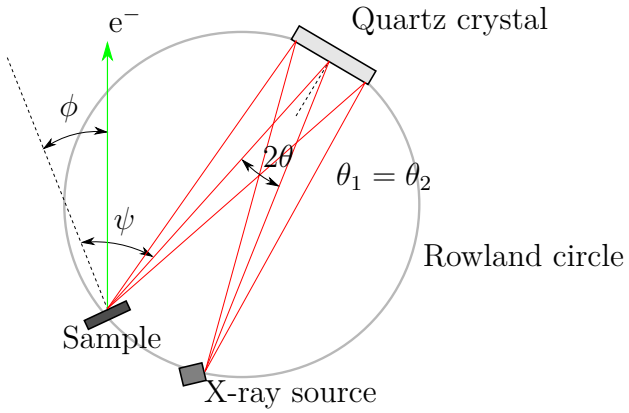

Figure 3.10: Schematic of how monochromatic light can be generated for X-rays. The sample, the X-ray source and a quartz crystal is placed in a configuration called a Rowland circle. The polychromatic X-rays are directed towards the quartz crystal where they are diffracted in all directions depending on the diffraction conditions. By directing the quartz crystal at an specific angle towards the sample diffracted monochromatic X-rays of narrow energy uncertainty will cause photoemission in the sample. Figure adapted from Ref.[56].

3.3 Angle-Resolved Photoemission Spectroscopy (ARPES)

ARPES is a measurement technique that makes use of the photoelectric effect to probe the electronic properties of solids, and makes it possible to map out energy bands directly. UPS is a quite similar technique, where the valence band at normal emission is probed. The details in this section about ARPES also applies to UPS.

3.3.1 Basic principles

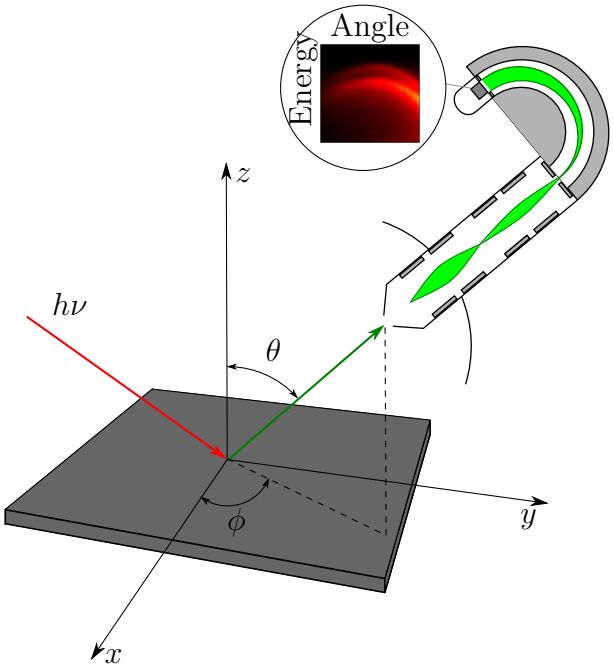

Figure 3.11: An experimental setup of an ARPES measurement. A photon with an energy $h\nu$ is directed towards a sample, this then emits an electron from the sample by the photoelectric effect which is collected by a hemispherical analyser at the angles ϕ and θ. The electrons travel through the hemispherical analyser before being detected.

ARPES follows the same principles of photoemission as XPS, but in ARPES rather than looking at the core levels the electronic structure of the valence band of the valence band is probed. In order to map out the electronic structure the kinetic energy of the collected electrons and the angle they are emitted at needs to be detected. This is done by collecting the electrons at a finite acceptance angle. The momentum of an electron emitted at an angle ϕ and θ is decomposed into

$$\boldsymbol{k_x} = \frac{1}{\hbar}\sqrt{2mE_{\text{kin}}}\sin\theta\cos\phi, \tag{3.29}$$

$$\boldsymbol{k_y} = \frac{1}{\hbar}\sqrt{2mE_{\text{kin}}}\sin\theta\sin\phi \tag{3.30}$$

and

$$\boldsymbol{k_z} = \frac{1}{\hbar}\sqrt{2mE_{\text{kin}}}\cos\theta. \tag{3.31}$$

where ϕ is the azimuthal angle in the plane, θ is the polar angle and m is the electron mass.

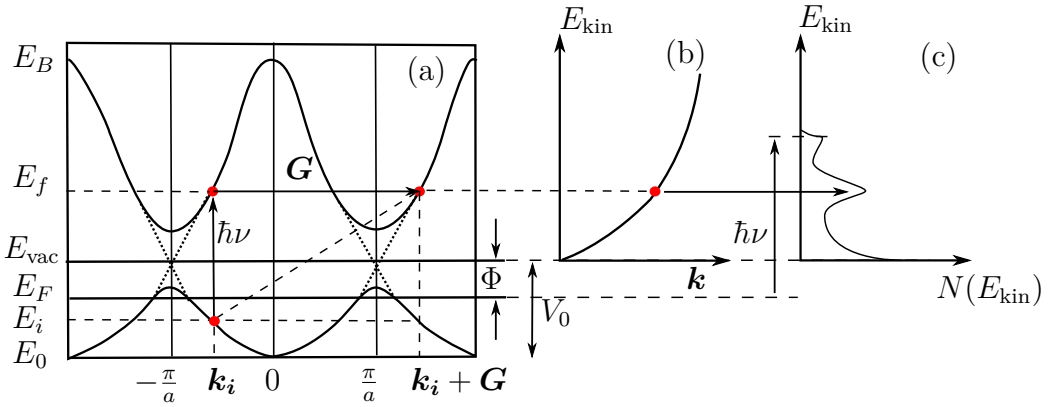

Figure 3.12: Kinematics of the photoemission process within the three-step nearly-free-electron final state model. (a) shows a direct optical transition in the solid supplied with the required momentum $\boldsymbol{G}$, Which creates a free-electron final state in vacuum in (b). This causes a photoelectron spectrum with a background due to scattered electrons in (c). Figure adapted from Ref.[39].

ARPES can be described by the same three step model as discussed earlier, and shown in Figure 3.12. First an electron is excited from the initial state to the final state either through a direct transition or supplied by the lattice with the required momentum. The transition is direct since for most measurements the photon-momentum is quite low, and is approximately zero. The electron then travels to the surface, where it passes through a surface potential and is liberated to vacuum. This leaves the parallel component of the electron momentum

$$\boldsymbol{k}_{||} = \frac{1}{\hbar}\sqrt{2mE_{kin}}\sin\theta \tag{3.32}$$

rigorously conserved in the process. On the other hand $\boldsymbol{k}_\perp$ is not conserved in the process, but it is still needed to map out the electronic dispersion $E(\boldsymbol{k})$ with the total crystal vector $\boldsymbol{k}$. To determine this further approximations are needed, for example under the nearly free electron model $\boldsymbol{k}_\perp$ can be approximated as

$$\boldsymbol{k}_\perp = \frac{1}{\hbar}\sqrt{2m(E_{\text{kin}}\cos^2(\theta) + V_0)} \tag{3.33}$$

where V_0 is the inner potential, the energy difference between the bottom of the valence band and vacuum.

3.3.2 Experimental setup

In order to do high quality ARPES measurements the detector and the manipulator impose limitations. This is the reason for the travel to St.Andrews, as the laboratory there is better suited for ARPES measurements. An attempt of an ARPES measurement in Trondheim with a channeltron detector is shown in Figure 3.13a, whilst a similar ARPES measurement with a 2D detector from St.Andrews is shown in Figure 3.13b. The channeltron detector has a finite angular acceptance range, and the manipulator also limits the resolution as after each scan the manipulator has to be moved to an new angle in order to map out the band structure. With a 2D detector the electrons are dispersed by angle in one direction and energy in the other direction, acquiring the electrons at a higher angular precision.

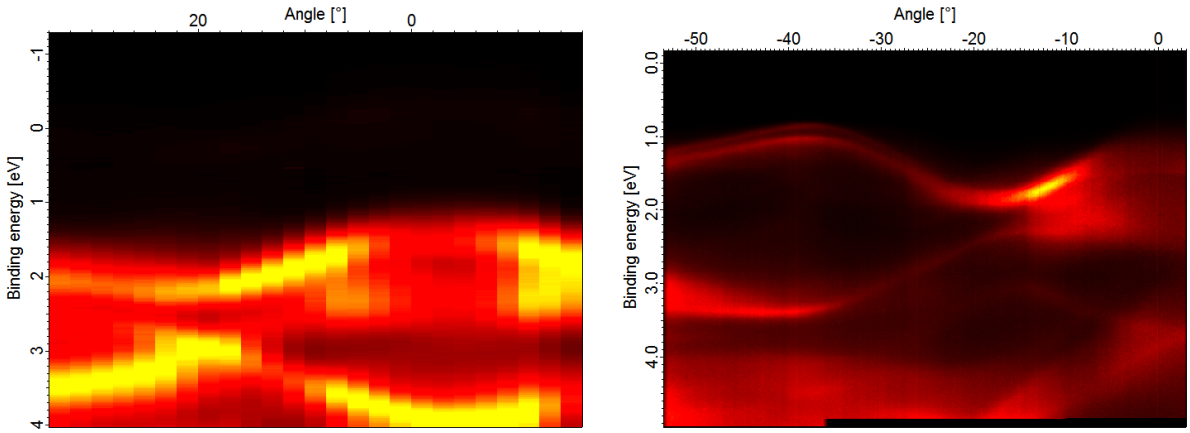

(a) ARPES with a line detector **(b)** ARPES with a 2D detector

Figure 3.13: Comparsion of two different detector systems for ARPES. Both spectra is taken on a freshly cleaved MoS_2 sample. The photon energy in (a) is from the HeI_α (21.2 eV) without monochromator, and (b) with a monochromator. (a) is dispersion on just off $\bar{\Gamma} - \bar{M}$, whereas (b) is a dispersion along $\bar{\Gamma} - \bar{K}$.

UV lamp

In order to get low energy photons a helium UV lamp is used. The lamp, sketched in Figure 3.14, works by letting a gas flow through the gas inlet. In this experiment helium gas was used, but argon, neon and other gases can also be used. In the center of the lamp the gas is ignited, creating a plasma. This plasma emits, just like in a fluorescent light bulb, light from the distinct emission lines, which are guided through a long capillary towards the sample where photoemission can happen. In order to keep the lamp from overheating a fan cools from the outside. Two stages of differential pumping pumps the gas away. The sketch in Figure 3.14 shows the UPS lamp used in the NTNU homelab, a SPECS UVS 10/35. In Scotland the SPECS UVS 300 was used, this is a higher flux, more intense and more sophisticated lamp. The general principle of creating a plasma that emits UV rays is the same. In St. Andrews there was also employed a monochromator, the SPECS TMM 304, for the UV rays employing the same principle for monochromation

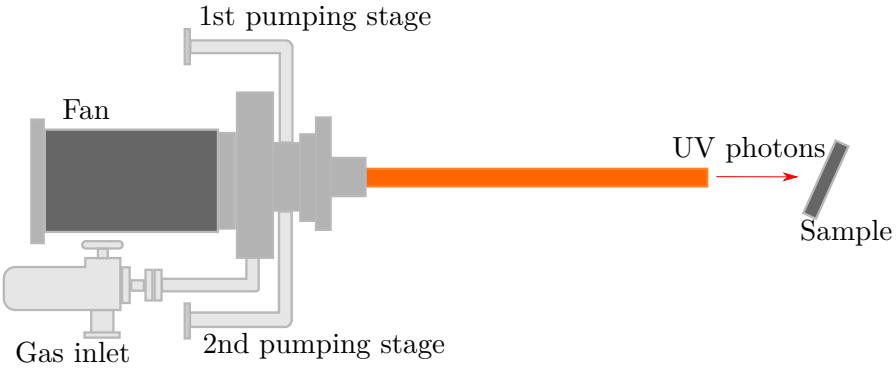

Figure 3.14: Sketch of the SPECS UVS 10/35 UPS lamp. The desired gas enters the gas inlet at a flow adjusted by a valve. The gas is ignited in the volume of the lamp, allowing the gas to be a plasma that discharges light at specific emission lines depending on the gas pressure. The light is directed towards the sample causing photoemission in the sample. A fan ensures that the lamp keeps cool, and two stages of differential pumping ensures that the gas is pumped away safely. The first pumping stage to a roughing pump were the majority of the gas is pumped, and the second stage to a turbo-molecular pump.

as the for the X-rays. With this lamp together with the electron analyser is the total energy resolution for ARPES system in St. Andrews of the order ∼3-10 meV.

3.4 Low energy electron diffraction (LEED)

Low Energy Electron Diffraction is an experimental technique for the determination of the crystal structure of a surface. The technique works by directing a collimated beam of low energy electrons towards a surface, allowing them to diffract and detecting the diffraction on a fluorescent screen.

The technique can be utilized for many practical purposes. Qualitatively can it be used for determining the symmetry and the structure of a surface. This is particularly useful for ARPES measurements, as this gives an indication of how the sample must be rotated in order to get to the right high symmetry direction. It can also be used to determine the crystalline reconstruction of an adsorbate layer on the surface. Even simpler it can be used to judge the quality of an overlayer on the surface, as a disordered overlayer would obstruct the diffraction and give a diffuse pattern. Quantitatively, so-called I-V curves can be generated, this is done by recording the intensity variation of the peak as the energy is changed. This can be compared to models, and can be used to determine the exact positions of the atoms in a crystal.

3.4.1 Basic principle

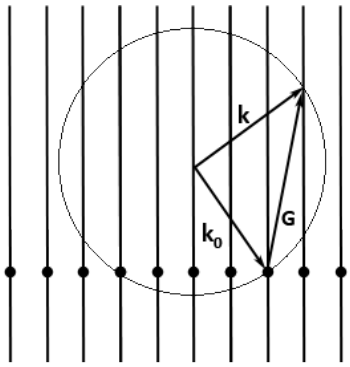

Figure 3.15: Ewald's sphere construction for diffraction from a 2D-lattice. The intersections between Ewald's sphere and reciprocal lattice rods defines allowed diffraction conditions. Figure taken from Ref.[57].

In the kinematic theory of diffraction in LEED, the electrons impinge on a well ordered surface and are scattered only once. The wavelength of the electron is given by the de Broglie hypothesis

$$\lambda = \frac{h}{\sqrt{2mE}}, \tag{3.34}$$

where h is Planck's constant, m is the electron mass and E is the kinetic energy of the electron. With some manipulation this ends up as

$$\lambda(\text{Å}) = \frac{12.265}{\sqrt{E(\text{eV})}} \tag{3.35}$$

in a normal LEED experiment. In LEED the electrons kinetic energy is in the range 20-300 eV, yielding a wavelength of around 1Å, which corresponds to interatomic distances. Since the kinetic energy of the electrons is so low or the mean free path of the electrons is so short that the electrons only can interact with the top few layers. This means that there will be no diffraction condition in the perpendicular direction. As a consequence the reciprocal lattice will then be a 2D lattice. The Ewald sphere for a 2D lattice is depicted in Figure 3.15. Instead of having reciprocal lattice points, the diffraction condition is defined by reciprocal lattice rods. The diffraction condition for a 2D lattice with an incident vector $\boldsymbol{k_0^{||}} = 2\pi/\lambda_0$ and a scattered vector $\boldsymbol{k}^{||} = 2\pi/\lambda$ is

$$\boldsymbol{k}^{||} - \boldsymbol{k_0^{||}} = \boldsymbol{G_{hk}} = h\boldsymbol{a^*} + k\boldsymbol{b^*} \tag{3.36}$$

where

$$\boldsymbol{a^*} = \frac{2\pi \boldsymbol{b} \times \hat{\boldsymbol{n}}}{|\boldsymbol{a} \times \boldsymbol{b}|} \tag{3.37}$$

and

$$\boldsymbol{b^*} = \frac{2\pi \hat{\boldsymbol{n}} \times \boldsymbol{a}}{|\boldsymbol{a} \times \boldsymbol{b}|}, \tag{3.38}$$

where $\boldsymbol{a}$ and $\boldsymbol{b}$ are dimensions of the real space lattice.

3.4.2 Experimental setup

A typical setup for a LEED system is shown in Figure 3.16a. A collimated beam of low energy electrons (20-200 eV) are generated by a filament, typically a tungsten filament or a LaB_6 filament. The electrons are directed upon a sample, and the electrons diffract with the crystal lattice in the sample. The scattered electrons then hit the fluorescent screen. The diffraction spots can then be detected by eye or a CCD camera.

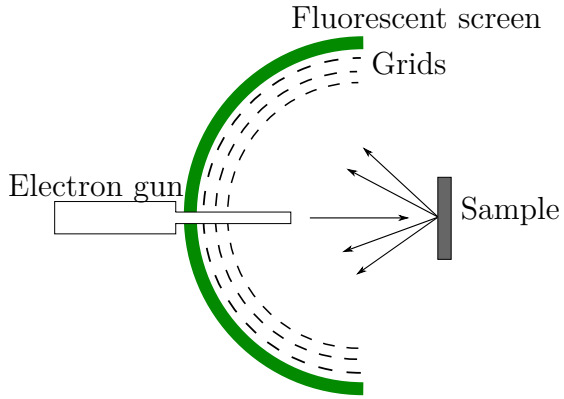

(a)

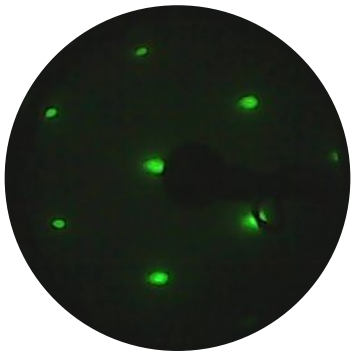

(b) Example LEED pattern of a cleaved MoS_2 crystal at 88 eV.

Figure 3.16: LEED schematic. (a) Electrons from an electron gun diffract in the sample, and creating a LEED pattern, as seen in (b), on a fluorescent screen.

3.5 Ultra High Vacuum

For doing photoemission experiments it is paramount to work in Ultra High Vacuum (UHV) conditions. The term UHV stands for a rest gas of a pressure of around 10^{-9} mbar and below. The importance of UHV is first of all for keeping the sample clean for surface sensitive experiments. Samples are often prepared in vacuum to ensure the cleanest conditions. Furthermore UHV prevents free particles of obstructing the path of the photoelectrons. In order to understand why UHV conditions is important the mean free path l of molecules by kinetic gas theory

$$l = \frac{k_B T}{\sqrt{2}\pi\xi^2 P} \tag{3.39}$$

can be investigated. Where ξ is the molecular diameter, P is the pressure of the gas, k_B is Boltzmanns constant and T is the temperature. At room temperature and ambient pressures the mean free path for a gas is on the order of nm. By reducing the pressure to UHV conditions, the mean free path is increased by 12 orders of magnitude to km.

Also by looking at the rate of impinging molecules R on a surface

$$R = \frac{P}{\sqrt{2\pi M k_B T}} \tag{3.40}$$

where M the molecular mass in units of the atomic mass constant. For a pressure of 10^{-6} mbar at room temperature the rate at which water molecules will impinge on the surface will be $R = 3.6 \times 10^{14}$ cm^{-2}s^{-1}. A surface contains 10^{15} atoms/cm^{-2}, and at these pressures the sample will be contaminated in the matter of seconds.

In order to achieve UHV several different pumping systems have to be used. A roughing pump will do the initial pumping down to about 10^{-3} mbar. This roughing pump backs a turbo molecular pump that will efficiently pump down to potentially 10^{-11} mbar. At 10^{-7} mbar an ion pump will be able to trap gas from interacting with the rest of the chamber. A titanium sublimation pump (TSP) will also help improve the vacuum.

There are several types of roughing pumps. For these experiments both rotary vane pumps and scroll pumps have been used. The principle of an oil sealed rotary vane pump is shown in Figure 3.17. The gas flows into the pump and is moved around to the exhaust by a rotating rotor. The disadvantage with these popular pumps is that there is a risk of getting oil contamination into the chamber. A scroll pump has the advantage that it is a dry pump. The principle of a scroll pump is sketched in Figure 3.18. The pump consist of two archimedean spirals, where one is fixed and the other is rotating. The gas enters between the opening of two archimedean spirals, and due to the rotation the gas can be transported away.

A cut through a turbo-molecular pump is shown in Figure 3.19. The turbo-molecular pump consists of several rotating blades spinning at normally 80000 revolutions per minute. When a gas molecule pass one of the rotating blades they gain momentum further into the stack of blades, and eventually gets pumped out. This works very efficiently for heavy molecules, but for lighter molecules a TSP is appropriate.

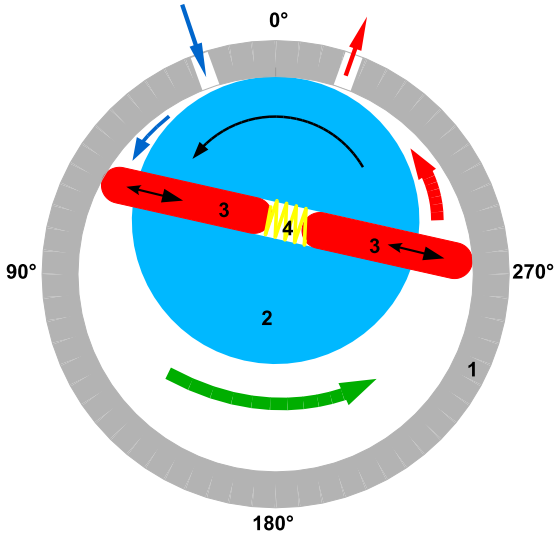

Figure 3.17: Rotary vane pump. By rotating spring loaded vanes on a rotor, gas is pumped out of the system to the exhaust. The system oil sealed. 1. system, 2. rotor, 3. vanes and 4. spring. Figure taken from Ref.[58]

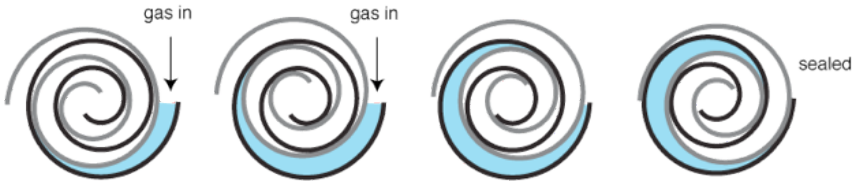

Figure 3.18: Sketch of a scroll pump. Gas enters into two archimedean spirals, where one is fixed and the other is rotating. The rotation of the spirals pumps the gas away. Figure taken from Ref.[59]

A titanium sublimation pump works by evaporating titanium onto the walls in a safe area in the vacuum chamber. Clean titanium is very reactive. Residual gas in the chamber is likely to hit the walls covered with titanium and react to form a stable, solid product, which in turn will reduce the gas pressure in the chamber. The reactivity of the titanium will reduce over time, so after a certain time a new layer of titanium will be evaporated onto the walls.

The principles of an ion pump is shown in Figure 3.20. A rest gas enters the ion pump where it is ionized by the high voltage difference between the anode and the cathode. The electric field accelerates the ions towards the titanium cathode where they are either buried in it or reacts with the titanium. Additionally, there is probability of titanium being sputtered off the cathode, and covering other parts of the pump with titanium. The pump will then act in the same way as a TSP, increasing the pumping efficiency. A magnetic field is also applied around the pump, making the ions travel in a helical motion, increasing the probability of ionizing other gas molecules.

Figure 3.19: A cut through turbo-molecular pump. The gas molecules enters at the top of the turbopump, and gain momentum through the stack of rotating blades. In the bottom left a roughing pump is connected to the flange and the gas is pumped out of the system. Figure taken from Ref.[60]

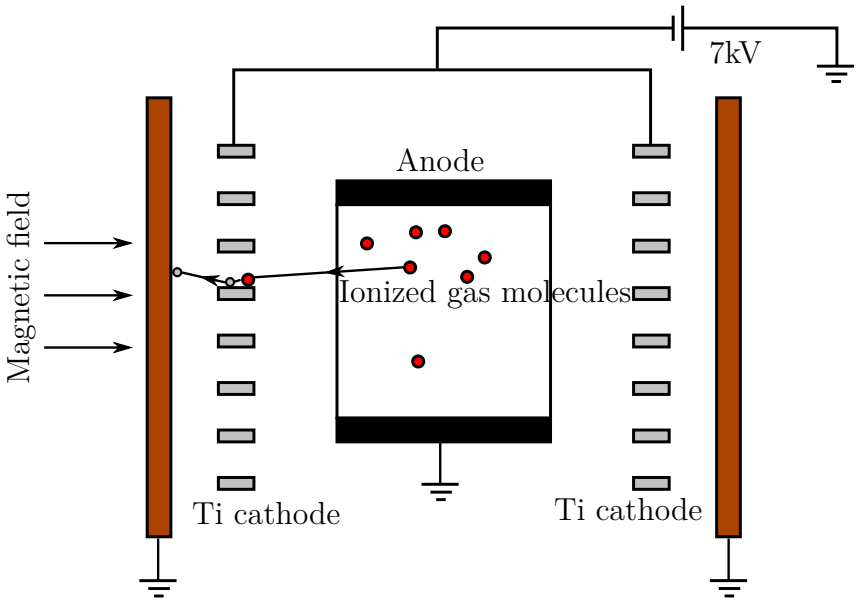

Figure 3.20: A schematic of an ion pump. An anode and a cathode is set under a voltage difference causing the gas in the pump to ionize and be accelerated towards the cathode. This burries the gas in the Ti cathode, and potentially sputters of Ti, leaving a clean surface of Ti to react with other molecules in the system. A magnetic field is present to make the gas molecules move in a spiral motion, increasing the probability of impacting other molecules and ionizing them.

4 Method

4.1 Sample

The samples used in this project were MoS_2 samples extracted from a lump of geolocial MoS_2 from the Kingsgate mine in New South Wales Australia. As other high quality large TMDC samples are hard to produce it was an advantage to these experiments to have a large amount of samples, that could be disposed if the quality of the cleave was not good enough. The large lump produced nice flakes with fairly homogeneous phases judged by eye, optical microscope and LEED.

4.2 Sample preparation

The sample was prepared in three different ways, two in the XPS laboratory at NTNU and one in the ARPES laboratory in St. Andrews. At NTNU the sample was prepared by gluing it to the sample plate with silver epoxy or by clipping the sample to the plate with two thin strips of tantalum foil by welding. The sample was then cleaved *in vacuo* by the scotch tape method, Figure 4.1. This was performed by taping one end of the tape to the sample and one to the wall of the load lock. Once vacuum was reached the sample was moved on the arm cleaving it as the scotch tape tore off. The quality of the sample was then judged by eye, LEED and XPS before proceeding with the experiments. Cleaving the samples by this method is not consistent, and it is important check whether the surface quality is good and contamination is low. In the process of cleaving, the surface of the sample might flake up, or it might tear off the tape unevenly. Quite a few samples had to be rejected before proceeding with the measurements. The clipped samples were harder to cleave, as they have some slack under the strips of tantalum. It became necessary to cleave some of the clipped samples in air, making them somewhat contaminated, mainly with carbon.

In St. Andrews the samples were cleaved *in situ* as shown in Figure 4.2a. The sample was first glued on top of the sample plate with silver epoxy, and was then baked for 15 minutes. This was to bake off moisture and let the glue set. A ceramic pin was glued to the sample with silver epoxy. Glue was also applied along the sides of the ceramic pin such that it was properly connected. The setup was baked again for 15 minutes. Then the sample was installed in the load lock, and moved through a multiple of vacuum chambers with decreasing pressure, finally arriving in the preparation chamber. In the preparation chamber a force was applied on the ceramic pin, Figure 4.2b, cleaving the sample and leaving a fresh new surface. This was done at low temperature, 25 K, to minimize the

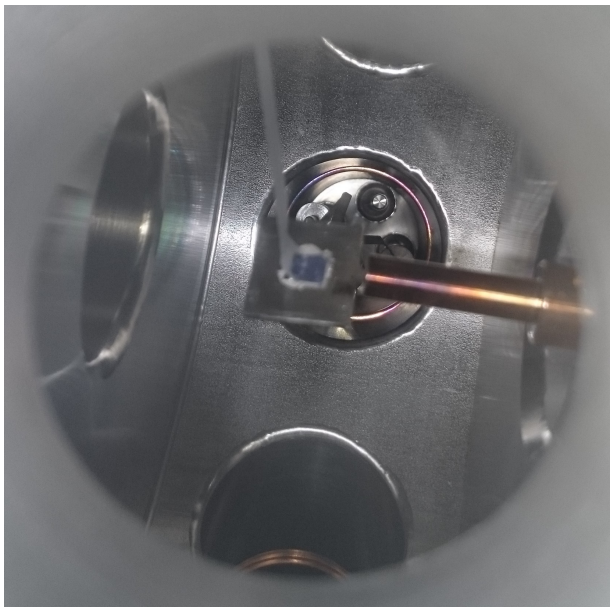

Figure 4.1: Cleaving by the scotch-tape method. The tape is glued to the wall of the vacuum chamber and the sample. As soon as vacuum in the range of 10^{-8} mbar is achieved is the arm with the sample moved. This exfoliates the top layers of the sample, leaving a clean surface.

time between the cleaving and measuring, in order to have the cleanest possible sample for the measurements.

The sample as described in the section 2.1 is built up of bilayers connected with weak van der Waals forces. When cleaving the sample, the aim is that the weak van der Waals forces will break and the sample will have single phased smooth surface.

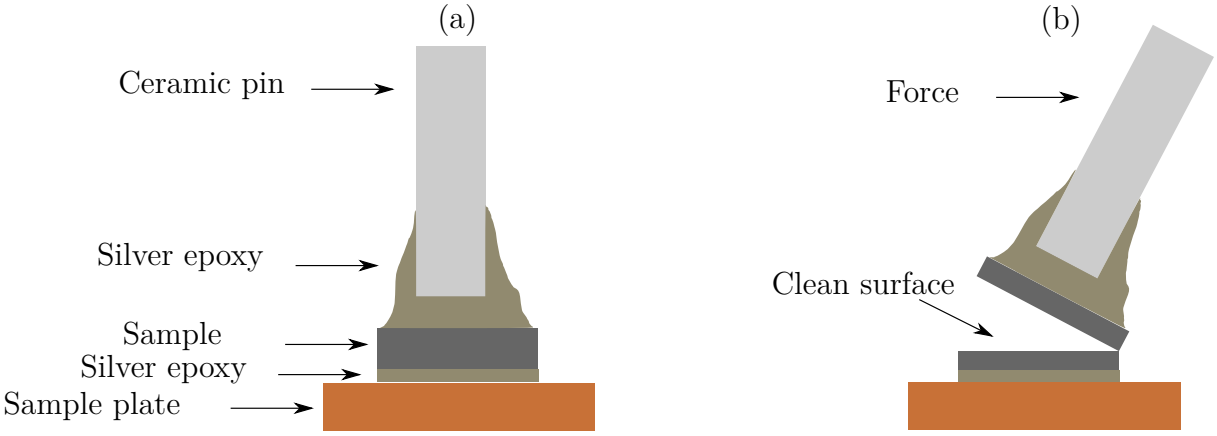

Figure 4.2: (a) is the sample prepared before cleaving. The sample is glued to a sample plate with silver epoxy, and has a ceramic glued to the top. (b) shows how the sample cleaves when force is applied to the ceramic pin.

4.3 Evaporation

4.3.1 Mini e-beam evaporator

In the XPS laboratory at NTNU iron was evaporated onto the sample by a Oxford Applied Research EGCO4 Mini e-Beam Evaporator, Figure 4.3. In the evaporator iron is installed as a rod. The rod is held at high voltage, which draws an electron current from a nearby hot filament. These electrons impact on the rod creating a hot tip, which evaporates the iron towards the sample. By manipulating the electron current a controlled growth on top of the sample can be obtained.

Figure 4.3: Mini e-beam evaporator. The evaporator is mounted on the outside of the vacuum directed towards the sample. Water cooling goes through the pipes, and there is the possibility to have shutter in order to deposit multiple materials. Figure taken from Ref.[61].

4.3.2 Evaporation of iron in St. Andrews

In St. Andrews the evaporation of iron was done by a much simpler “homemade” device. It was an iron wire wrapped around with a tungsten wire. The tungsten wire had a current running through it, such that the iron wire was heated and iron could evaporate onto the sample. Compared to the Mini e-beam evaporator the evaporation in this setup was less controllable, though with trial and error acceptable overlayers were achieved. The thickness of the overlayer was estimated by XPS.

4.3.3 Evaporation of potassium

To evaporate potassium on the sample, a factory-made SAES getter was used. The dispenser, Figure 4.4, has a container in the middle with potassium that is sealed with a glue. This keeps the reactive alkali metal from contact with air, which is crucial for a pure dosing. The evaporator was mounted on a feed-through by welding the flat ”wings” on the side of the getter to the electrical connectors on the feed-through. From the outside a power source was connected, so that an electrical current could run through it. Before dosing any potassium a smaller current had to be used in order to dissolve and pump away

the glue. By increasing the current the potassium would start to evaporate, covering the sample in potassium. These dosers give a fairly homogeneous film coverage at a fairly consistent rate depending on the current.

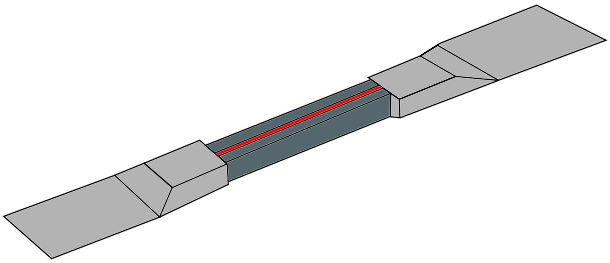

Figure 4.4: Potassium doser. Potassium is contained in the centre volume that is sealed off by glue.

4.4 Thermal treatment

The measurements in XPS laboratory at NTNU was carried out at room temperature. In order to attempt to intercalate iron into the crystal structure the sample was heated to a higher temperatures. This was done by putting a current through a filament that was placed under the sample holder on the manipulator heating the sample radiatively from beneath. By this method temperatures of 700°C could be achieved. After heating the sample was cooled down to approximately room temperature, before proceeding with measurements.

In St. Andrews the sample was kept at 25K at all measurements and the deposition of iron was done at approximately room temperature. In ARPES measurements it is desired to have the best energy resolution possible to resolve subtle details in the electronic structure. By cooling the sample down to the lowest possible temperatures the thermal broadening of the spectrum is reduced, and higher energy resolution is achieved. These temperatures were achieved by feeding liquid helium down the manipulator and cooling the sample. The temperature was controlled by controlled heating against the cooling of the sample, to keep the sample temperature fixed over the measurements. The deposition of iron was performed on a different manipulator arm in a different vacuum chamber, which was not cooled. Over the time it took to transfer the sample and prepare the evaporator the sample was most likely at room temperature.

4.5 Measurement and data analysis

The XPS measurements in the results chapter has been measured in fixed analyser transmission mode (FAT) where core levels are taken at a pass energy $E_{\text{pass}} = 30$ eV and the widescans are taken at $E_{\text{pass}} = 100$ eV.

The analysis of the XPS data was carried out by curve fitting and calculating the areas of the of the individual components in IGOR PRO. The data had first the Shirley

background subtracted from them, and was then curve fitted with Voigt functions. The most important information to extract from the core levels is the area and the position of the different components in order to calculate the thickness, make an ARXPS curve and estimate the stoichiometry. Some of the core levels, like the S 2p and Fe 2p core level, had no other overlapping components, and a area of the background subtracted data sufficed. The Mo 3d core level was fitted by Voigt functions, in order to distinguish the overlap from the S 2s core level.

The ARXPS curves are generated by measuring the desired core levels over a wide angle range. At each angle the area of each core level is calculated. The data is then presented in order to best be evaluated by the two models presented in section 3.2.3.

Thickness of the overlayers in the results section will be referred to by the thickness calculated by equation (3.17) from the Mo 3d core level and the Fe 2p core level. As it turns out is the coverage of the sample discussable, still this provides a reference with respect to the data acquired on the different samples.

In order to acquire ARPES measurements the sample was first aligned by LEED or a laser. The orientation of the LEED pattern tell how the sample is aligned. In Figure 3.16b is the sample aligned by few degrees off $\bar{\Gamma} - \bar{M}$ high symmetry line in reference to analyser slit in the XPS laboratory in Trondheim. By rotating the sample 30° in the azimuthal direction, the sample would be aligned along $\bar{\Gamma} - \bar{K}$. By laser can the sample be aligned by shining laserlight on the sample and aligning the reflection to a specific position. ARPES measurements are then acquired by rotating the sample by equations (3.29) and (3.30) to the desired location in reciprocal space, and measuring. Two types of scans where acquired by ARPES. The angular dispersions were acquired by dispersing angle and energy on the detector and rotating the sample along the high symmetry line. The $\bar{K}$-point was found accurately by doing a constant energy map around $\bar{K}$. This is done by taking several scans as indicated in 4.5, and using the data to build the map to accurately determine the $\bar{K}$-point. Such maps can also be used to build a 3D maps of the band structure in the whole BZ.

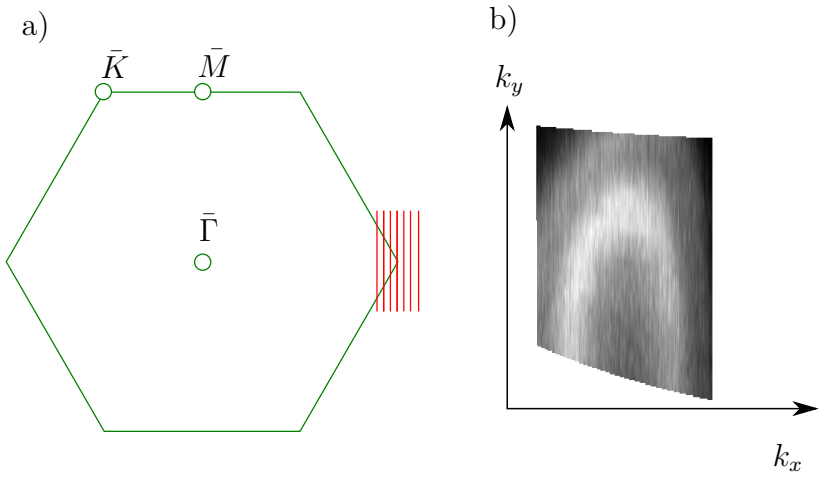

Figure 4.5: Sketch of how to do a constant energy map. (a) shows the hexagonal 1BZ of MoS_2. Several scans are done with the analyser slit aligned as indicated by the red lines. By treating data a constant energy like the one shown in (b) can be created around $\bar{K}$. (b) shows a constant energy map at E_B =1.07 eV, showing two bands crossing.

The ARPES data was analysed by stitching together the respective scans to build a picture of the valence band. Before presenting the data, the data was k-warped, changing the measurements k instead of angle. Energy distribution curves (EDC) were created by summing over a finite small angular range of the ARPES dispersion plotting energy versus intensity. These were fitted with Voigt functions after a Shirley background was subtracted from them.

5 Results

In this section the main results for the experiments carried out in this project will be presented. First, the data acquired in the XPS laboratory in Trondheim will be presented. In this section, the data collected for MoS_2 samples where iron and potassium doping has been carried out at the material surface will be presented. In the second section the ARXPS measurements will be presented together with fits modelled by the multilayer model and intercalation/island model. In the last section XPS, LEED and ARPES data acquired in St. Andrews will be presented.

5.1 XPS, LEED and ARPES

5.1.1 Growth of iron on MoS_2

Typical XPS spectra with depositions of iron on the surface of MoS_2 are shown in Figure 5.1a. This sample was cleaved in vacuum and showed negligible contamination of carbon and oxygen or any other contaminant. The thickness of the iron overlayer was calculated to be 0.2 nm for the first deposition and 0.5 nm for the second deposition. In Figures 5.1(b)-(d) high resolution scans of the Mo 3d, S 2p and Fe 2p core levels are shown. The addition of iron influences the spectra for the Mo 3d and S 2p core level by shifting them towards lower binding energy. The Mo 3d5/2 peak is found at 229.40 eV before any treatment, after the first deposition of iron it first shifts 0.31 eV, and an additional 0.02 eV after the second iron deposition. The same shift is also observed for the S 2p core level.

Growth on several samples has been carried out and the initial position of the Mo 3d5/2 core level before addition of iron was measured to be 229.54±0.14 eV, which fits well according to average values in NISTs database [62]. The addition of iron caused a shift to 229.03±0.04 eV, which is an average shift of the Mo 3d5/2 peak is 0.41±0.07 eV. The larger uncertainty in the binding energy position of the freshly cleaved surface is due to different levels of contamination in the different samples, which may shift the peak. The contamination was generally low, and usually from carbon. For samples with two depositions of iron the shift seemed to saturate after the first deposition, with only a minor shift after the second deposition. All depositions carried out were in the range of 0.2 nm to 0.8 nm, without any significant difference between a smaller deposition and a larger deposition. The deposition of iron to the surface did not change the relative intensity between the Mo 3d core level and S 2p core level. The FWHM of the S 2p and Mo 3d core levels stayed the same after deposition suggesting that no chemical reaction was occurring.

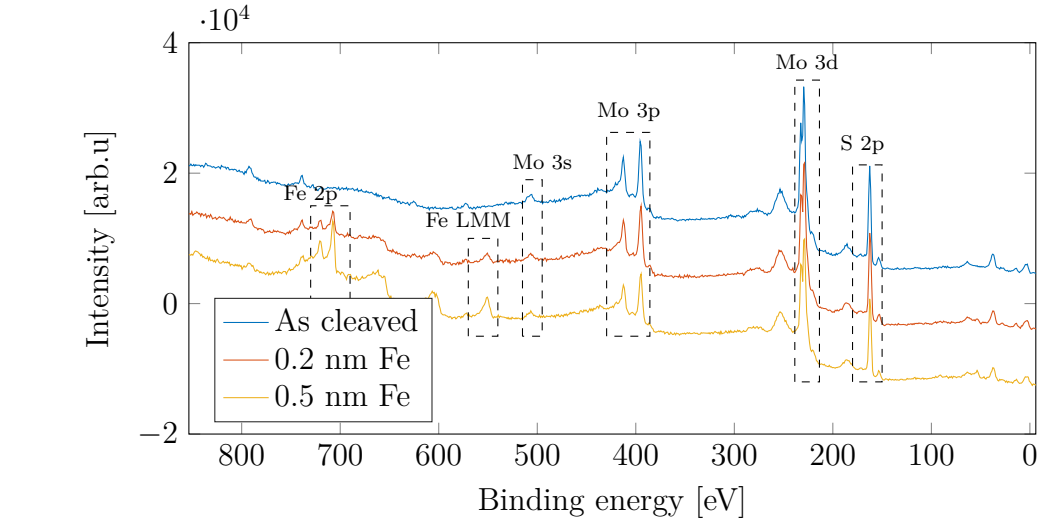

(a) Widescan

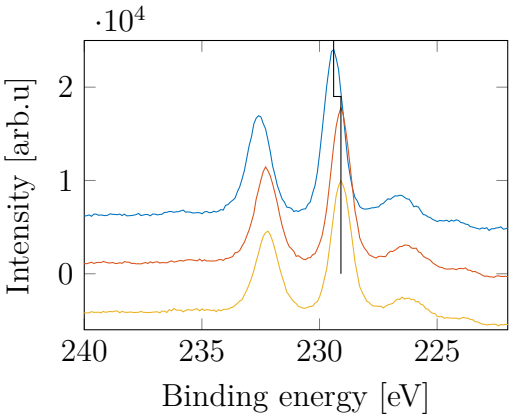

(b) Mo 3d

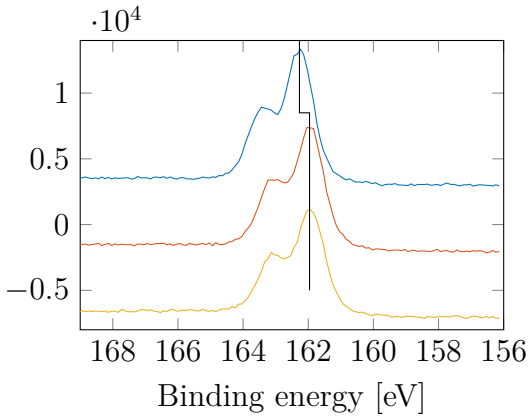

(c) S 2p

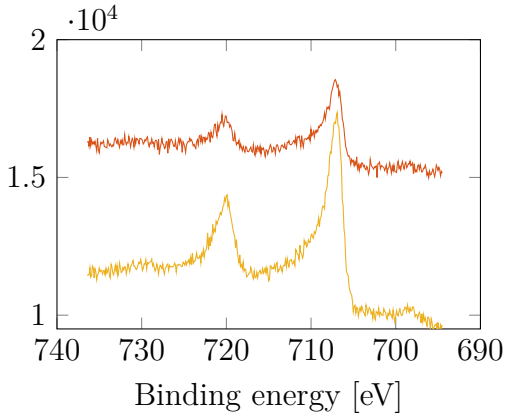

(d) Fe 2p

Figure 5.1: (a) XPS widescan using a Mg K_α (1253.6 eV) source showing how the spectra changes with a cleaved sample, an overlayer of 0.2 nm iron and an overlayer of 0.5 nm iron. (b), (c) and (d) show the changes to the core levels Mo 3d, S 2p and Fe 2p with respect to the same addition of iron. Each scan is subtracted a constant offset, where the top most curve corresponds to the real number of counts. For the widescan the offset is -8500, for Mo 3d it is -5000, for S 2p it is -5000, for Fe 2p it is -7000. The line through the Mo 3d5/2 peak and the S 2p3/2 peak is added as a guide for the eye to observe the shift.

In Figure 5.2 a comparison of LEED measurements of two different layer thicknesses is shown. The samples show a hexagonal LEED pattern as expected for the 2H-polymorph of MoS_2. The addition of iron to the sample blurs the LEED pattern, making it weaker. No additional reconstructing due to the iron deposition was observed. This may suggest that the iron is not making a new ordered structure on the surface.

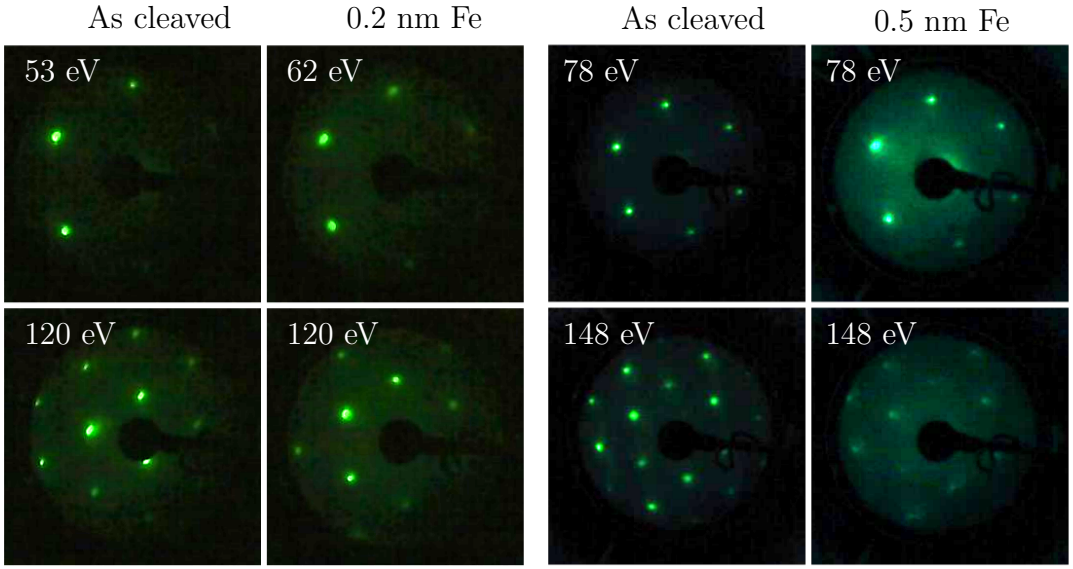

Figure 5.2: LEED pattern of two different samples with addition of 0.2 nm Fe and 0.5 nm Fe. The measurements are taken with an electron energy indicated in the top left corner.

The ARPES dispersion in Figure 5.3 is a cut off the Γ-K direction as indicated in Figure 5.3c. Figure 5.3b shows that even with an addition of 0.6 nm of iron there is still a dispersion from the MoS_2, but shifted approximately 0.3 eV towards lower binding energy, similar to the shift seen in the core levels in Figure 5.1. At the Fermi level a flat band is formed, probably derived from an amorphous metal on the surface. In Figure 5.3(d) an UPS measurement at normal emission is shown. This clearly visualizes that the line shape of the sample is shifted by 0.3 eV, and as already shown in the ARPES spectra a band at the Fermi level forms. The shift observed in the core levels and the valence band attributed to band bending, caused by the p-doping effect of the iron deposition.

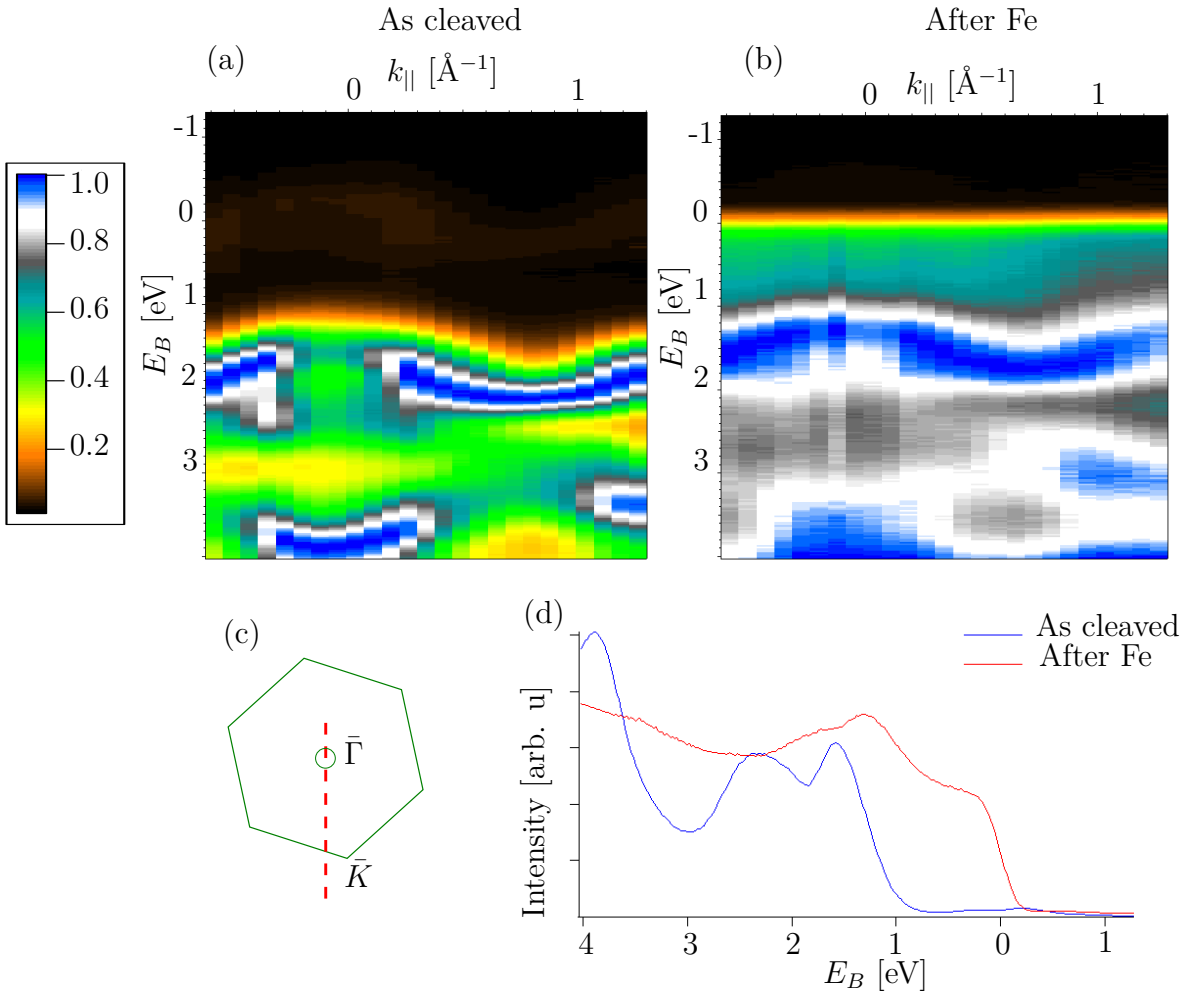

Figure 5.3: ARPES and UPS measurements on a sample with and without iron. (a) and (b) show ARPES dispersions along the red line indicated in the schematic representation of 1BZ in (c). (a) is the sample as cleaved, and (b) is the sample with an iron overlayer of 0.6 nm. In (d) UPS measurements at normal emission is shown. The measurements are taken with a HeI$_\alpha$ (21.2 eV) source.

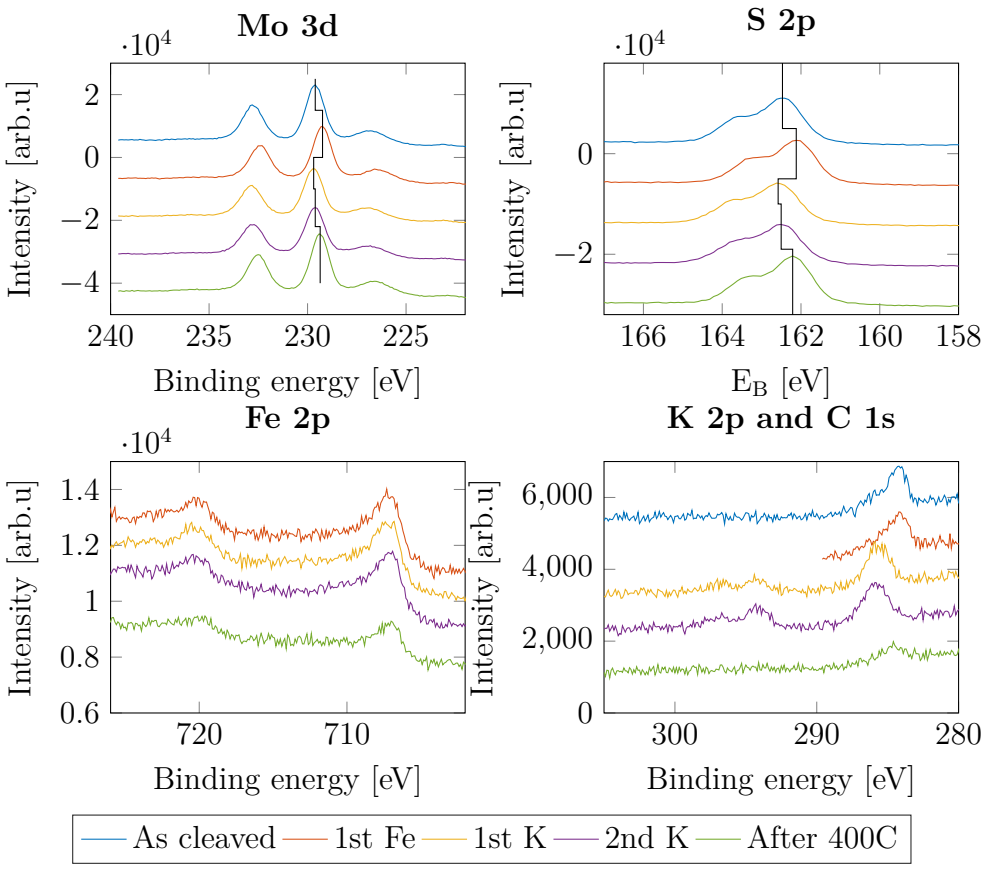

Figure 5.4: Core level XPS scans using a Al K_α (1486.6 eV) of Mo 3d, S 2p, Fe 2p, K 2p and C 1s on a sample treated with first a deposition with 0.2 nm iron, then two doses at 15 seconds at 5.5 A of potassium, and then annealed to 400°C. The scans are acquired by an Al K_α source (1486.61 eV). Each scan is subtracted a constant offset, where the top most curve corresponds to the real number of counts. For Mo 3d the offset is -10000, for S 2p it is -8000, for Fe 2p it is -1000 and for K 2p/C 1s it is -1000. The line through the Mo 3d5/2 peak and the S 2p3/2 peak is added as a guide for the eye to observe the shift.

5.1.2 Potassium counterdoping

Figure 5.4 shows the core levels with the addition of iron and potassium to the surface of MoS_2. The heat treatment to 400°C will be commented in the next section. Carbon contamination can be observed in Figure 5.4, the contamination is likely due to the fact that the sample has been cleaved in air. This sample was first dosed with 0.2 nm of iron, which caused a shift of 0.36 eV in the Mo 3d and S 2p core level. After the deposition of iron is the C 1s unaffected suggesting that iron is not interacting with the carbon. The sample was then dosed with potassium two times for 15 seconds each at a current 5.5 A with the potassium evaporator, shifting the core level back to its initial as cleaved position. The addition of potassium to the surface seems to have no effect on the iron core level. On the other hand the carbon core level shifts, suggesting that the potassium reacts with the carbon present on the surface. The addition of potassium does not change the relative intensity of the Mo 3d and S 2p core levels nor their FWHM.

The addition of potassium affects the LEED pattern even more strongly than iron, as visible in the strongly suppressed LEED intensity in Figure 5.5. The amount of the doped potassium is very small, thus it can be excluded that it is enough to give rise to a overlayer on the surface.

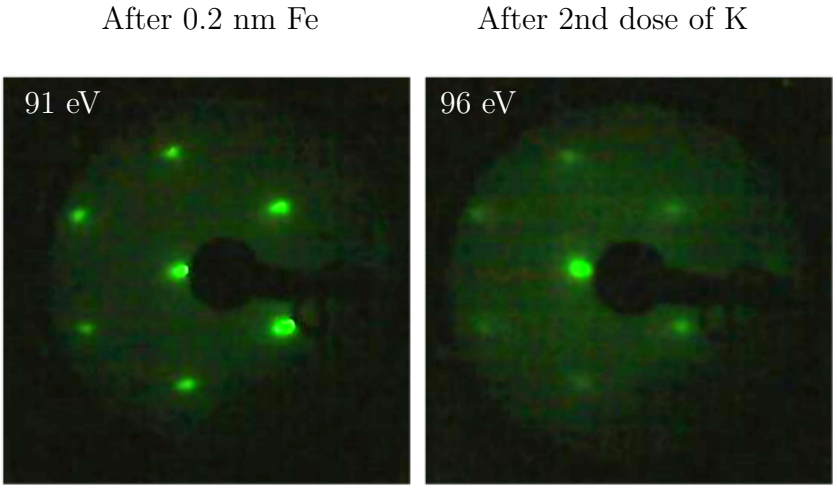

Figure 5.5: LEED measurements comparing the crystal structure at the surface after a 30 second deposition of potassium on a MoS_2 sample with 0.2 nm of iron on the surface. The measurements are taken with an electron energy indicated in the top left corner.

5.1.3 Heat treatment with iron on MoS_2

Heat treatment was first attempted with the samples glued to the sample plate with silver epoxy. This lead to substantial degassing most likely from the glue, and after annealing to 150°C the LEED pattern was barely visible and the XPS showed large contamination of oxygen and carbon.

In order to try to reduce the degassing, the glue was set to cure longer. Previously it had been cured for 45 minutes, now it was left over night. This lead to a lower degassing, when the sample was heated to 80°C. The sample was then exposed to air before doing the last measurements. This produced the LEED patterns seen in Figure 5.6, where exposing the sample to atmosphere did not seem to affect the LEED pattern significantly. On the other hand, the Fe 2p core level had completely shifted in Figure 5.7. The new position of the Fe 2p core level corresponds to iron being bonded in Fe_2O_3. Heating to higher temperatures would degas the glue even more as this would be outside the serving temperature of the glue. The samples were after these observations clipped in order to be able to heat the samples to higher temperatures.

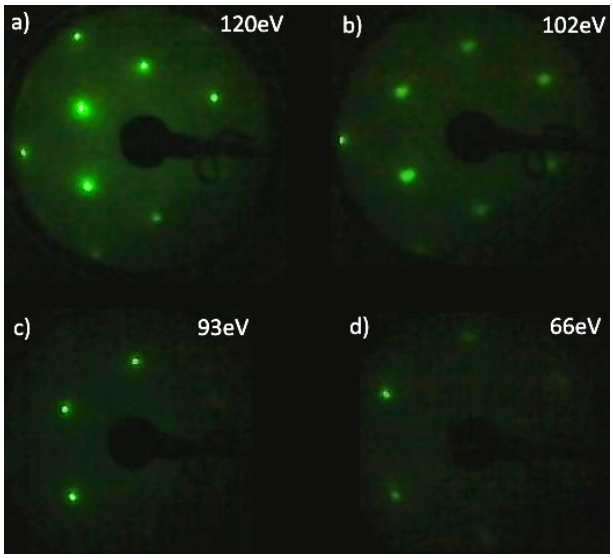

Figure 5.6: LEED patterns of MoS_2 after deposition of 0.3 nm of iron. Figures a) and c) show the patterns obtained after annealing the sample to 80°C. Figures b) and d) show the patterns obtained after exposing the sample to atmosphere for 5 minutes.

In Figure 5.8 the XPS core levels of a sample with an overlayer of 0.4 nm of iron annealed to 500°C is shown. After heating the sample to 500°C both the Mo 3d and S 2p core level shifted by 0.2 eV to higher binding energy. After heating the sample the relative intensity of both S 2p and Mo 3d increased, whereas the relative intensity in iron and carbon was reduced. Carbon was most likely desorbed from the surface, whereas how the iron was behaving will be further discussed later. There was no change in the relative intensity of the Mo 3d core level compared to S 2p core level, and their FWHM stayed constant before and after annealing.

In Figure 5.4 the sample was annealed to 400°C after being exposed to 0.2 nm iron and a small dose of potassium. Annealing the sample caused a shift of 0.24 eV Mo 3d5/2

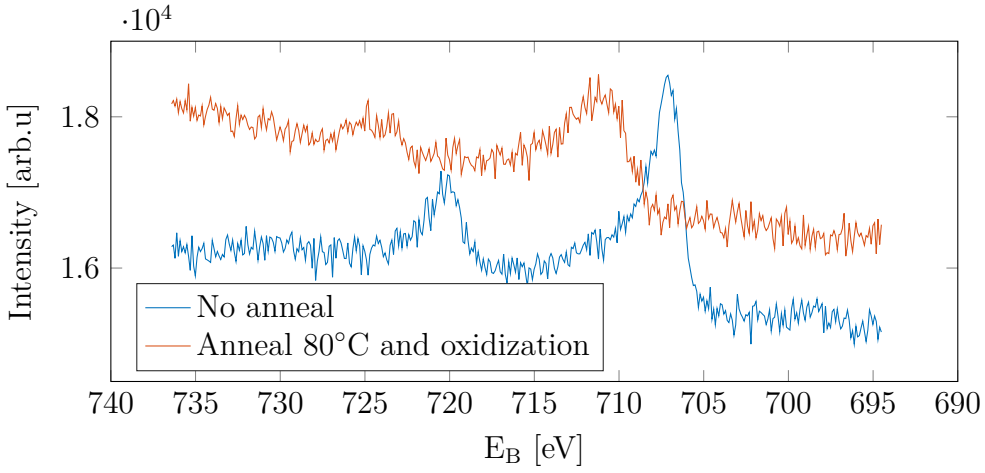

Figure 5.7: XPS core level scan of Fe 2p of a sample annealed and oxidized and a sample with a pure iron overlayer. The measurements were taken with a Mg K_α (1253.6 eV) source.

and S 2p towards lower binding energy. The spectra had already been shifted by the potassium to the same binding energy as if the sample was pristine and freshly cleaved. After heating both K 1s and C 1s reduced substantially, whereas the relative intensity in Mo 3d and S 2p increased. The relative intensity and FWHM between the Mo 3d core level and S 2p core level remained constant after heating similar to the other annealing.

The LEED pattern for the sample heated to 500°C is fully recovered as shown in Figure 5.9. For this sample it was difficult to find a LEED pattern after the deposition of iron at an electron energy lower than 190 eV. In Figure 5.9 a sharp LEED pattern at 82 eV is observed, suggesting that the surface has a ordered structure.

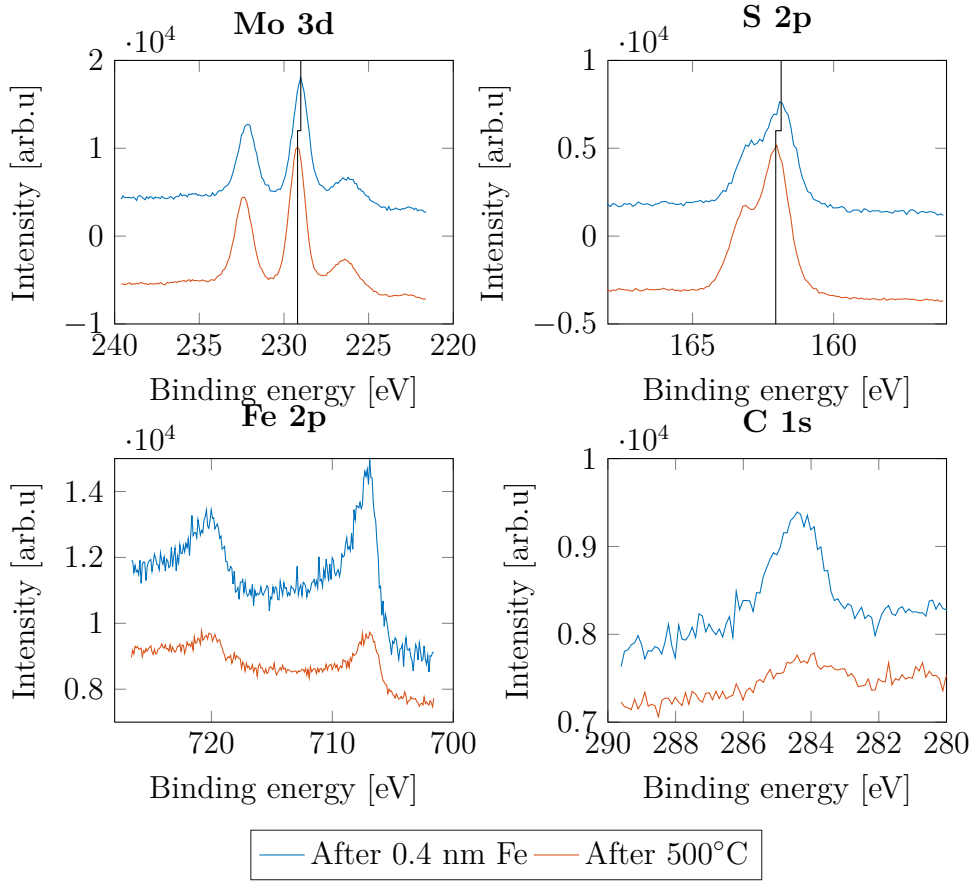

Figure 5.8: Core level XPS scans using a Al K_α (1486.6 eV) source of Mo 3d, S 2p, Fe 2p and C1s on a sample treated with first a deposition with 0.6 nm iron and then annealed to 500°C. The scans are acquired by an Al K_α source (1486.61 eV). Each scan is subtracted a constant shift, where the top most curve corresponds to the number of counts. For Mo 3d the offset is -10000, for S 2p it is -5000, for Fe 2p it is -1000 and for C 1s it is +1000. The line through the Mo 3d5/2 peak and the S 2p3/2 peak is added as a guide for the eye to observe the shift.

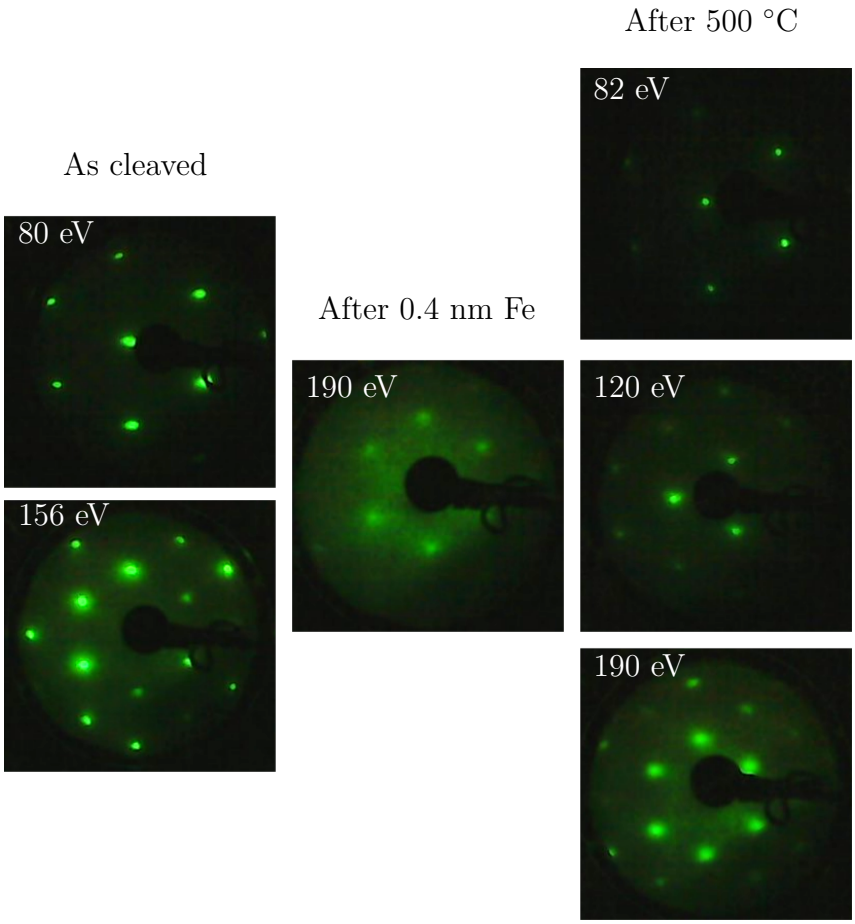

Figure 5.9: LEED measurements showing the evolution of a sample as the sample is deposited with 0.4 nm Fe, and then heated to 500°C. The electron energy is denoted in the top left corner of each measurement.

5.2 ARXPS

The ARXPS data has been fitted by two different models the agglomeration/intercalation model and the multilayer model. The agglomeration/intercalation model is presented in Figures 5.10 and 5.11 with fit coefficients denoted in Tables 5.1, 5.2 and 5.3. The XPS data presented in Figure 5.8 is for the sample as the ARXPS data in Figure 5.10. As a reminder, in the agglomeration/intercalation model c represents the coverage/concentration of iron and d represents the "depth of intercalation"/"island height". The data in Figure 5.10 before annealing is fitted in two different ways, one where $c = 1$, as if the overlayer was continuous, and one where c is used as a unbound fit parameter.

After heating the sample up to 500°C, it is not expected that a uniform iron layer will form onto the surface: either intercalation or clustering is likely to occur. This will impose a restriction on the parameter c which is expected to be different from 1. In addition, for the data collected after annealing, two different fitting schemes have been used: The first, where all data points have been taken into account and the second where the first three points have been excluded, since they showed a significant deviation with respect to the whole observed trend. Such a deviation could be explained by photoelectric diffraction. Both the measurements in Figure 5.10 and 5.11 are taken on the same sample, just two different cleaves. The LEED measurements in Figures 5.9 and 5.5, both show that the samples are aligned along a high symmetry direction. The emitted photoelectrons will then be able to fulfill diffraction conditions on their way out of the crystal, giving a large increase in intensity at the angle where the diffraction condition is fulfilled.

Table 5.1: Fixed values for the models. $I^{\infty}_{\text{Fe 2p}}/I^{\infty}_{\text{Mo 3d}}$ is calculated from theory and λ is provided by NIST EAL software [53].

$I^{\infty}_{\text{Fe 2p}}/I^{\infty}_{\text{Mo 3d}}$	$\lambda_{\text{Mo 3d}}$	$\lambda_{\text{Fe 2p}}$
0.86	1.6 nm	1.0 nm

Table 5.2: Fit values for the fits in Figure 5.10, where c is the coverage/concentration and d is the "depth of intercalation"/"island height" as defined in section 3.2.3.

	c	d [nm]
Fit Fe (c fixed)	1	0.35±0.01
Fit Fe (c free)	0.51±0.06	0.97±0.2
Fit 1 500°C	0.3±0.1	0.5±0.3
Fit 2 500°C	0.85±0.01	0.15±0.09

The photoelectric diffraction is more evident in Figure 5.11, where it scatters the trend more. The sample in Figure 5.11 had iron deposited for half time as the sample in Figure 5.10. In Figure 5.11 measurements for just iron on the surface and after the deposition of potassium to the surface is provided, showing that there is no significant change after deposition of potassium. Two fits are provided to this data, one where $c = 1$ corresponding to full coverage of the surface, and one where c is allowed to float. After heating to 400°C one fit is provided neglecting the data point at 5° as it is an outlier and probably is taken at a diffraction condition.

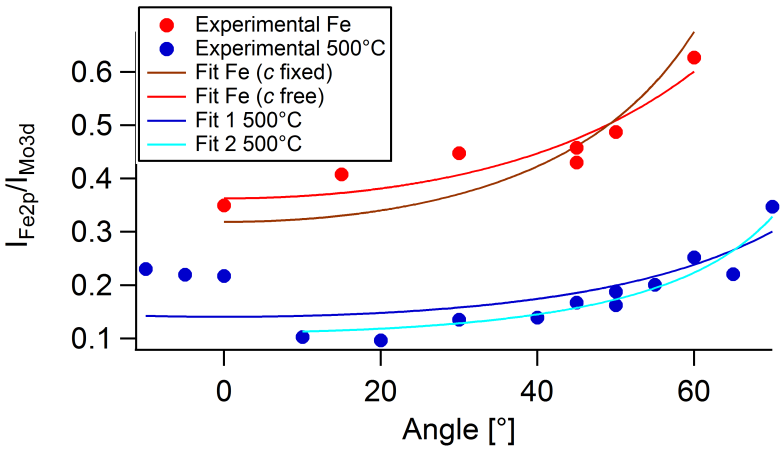

Figure 5.10: Angular dispersed XPS data for sample dosed with iron for 5 minutes and 40 seconds at 10nA flux. Red dots denote the experimental data before the sample is heated, and blue dots after the sample has been annealed to 500°C. Two fits are provided for the sample before annealing, one where $c = 1$ corresponding to a continuous overlayer, and the other where c is allowed to be an unbound fit paramter. After annealing the sample, two fits are provided where "Fit 2 500°C" keeps constraint on the fitting range. The vertical axis corresponds to intensity of Fe 2p divided intensity of Mo 3d. Fit parameters are provided in Table 5.2 and 5.1.

Table 5.3: Fit values for the fits in Figure 5.11, where c is the coverage/concentration and d is the "depth of intercalation"/"island height" as defined in section 3.2.3.

	c	d [nm]
Fit Fe (c fixed)	1	0.22±0.01
Fit Fe (c free)	0.55±0.1	0.50±0.14
Fit 400°C	0.15±0.02	2.05±0.93

In Figure 5.12 ARXPS data from a sample with iron on the surface is modelled with the multilayer model fitted with maximum entropy theory. The fit in Figure 5.12 is given by the concentration matrix in Table 5.4. The ARXPS data is the same as the data before annealing in Figure 5.11. The data is presented in a different way, instead just comparing the Fe 2p and Mo 3d core level, S 2p is also included. The model suggests that the sample is situated on a substrate, and the iron is found within the first 0.3 nm. As all the core levels are normalized the photoelectron diffraction is reduced.

In Figure 5.13 ARXPS data of the sample heated to 400°C with potassium and iron the surface fitted by the concentration profile in Figure 5.13b is presented. The fit is good at higher angles, whereas lower angles the fit is not as good, but here the data is also obstructed by photoelectron diffraction. The model suggests that there is an even distribution of ∼10% iron within the first unit cell, with slightly more iron on the surface. The sample heated to 500°C with just with iron on the surface modelled with the multilayer model is shown in Figure 5.14. The fit suggests that the iron is distributed at a concentration of ∼10% within the first two unit cells, also with a slightly more iron on the surface. The model has been simplified by assuming continuous distributions of molybdenum and sulphur within the crystal, which is an acceptable approximation with

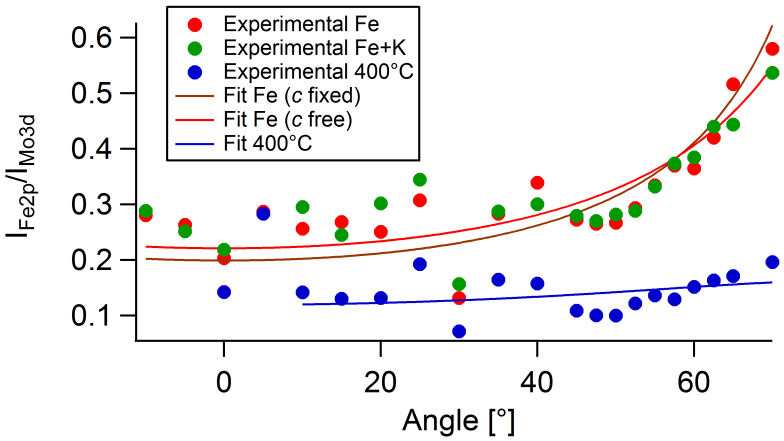

Figure 5.11: Angular dispersed XPS data for sample dosed with iron for 2 minutes and 50 seconds at 10nA flux. Red dots denotes the experimental data after iron deposited to the surface, green dots after potassium has been deposited to the surface and blue dots after the sample has been annealed to 400°C. Two fits are provided before annealing, where c fixed corresponds to a continuous overlayer, and the other where c is allowed to be fitted freely. After annealing one fit is provided to the data, where the point at 5° is neglected as this an outlier. The vertical axis corresponds to intensity of Fe 2p divided by intensity of Mo 3d. Fit parameters are provided in Table 5.3 and 5.1.

Table 5.4: Layer by layer concentration matrix of the fit presented in Figure 5.12. Each row and column represents the concentration of the respective element in the respective layer starting from the surface at the top. The layer thickness $d = 0.3$ nm.

Fe	Mo	S
0.52	0.22	0.25
0	0.33	0.66
0	0.37	0.62
0	0.33	0.66
⋮	⋮	⋮

a layer thickness of 0.3 nm.

Lastly in Figure 5.15 the measured ARXPS profile for the sample with iron and potassium is added as a reference before annealing. In this is carbon included in the angular distribution. Figure 5.15b shows a relative density plot, this is created by taking the logarithm of the intensity at 60° divided by the intensity at 0°, providing a depth profile of the element independent of the other elements present in the sample. This suggest that carbon is a surface contaminant, and that iron and potassium is situated in the surface region.

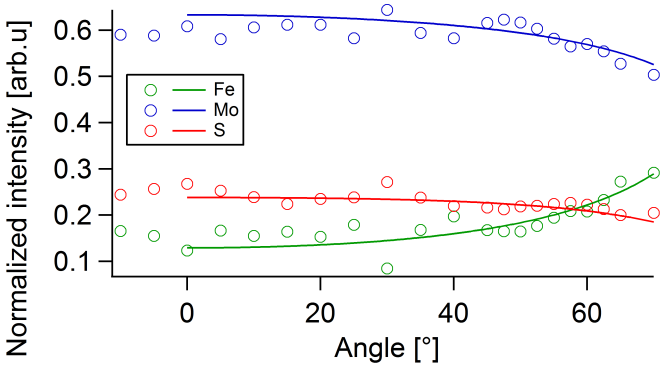

Figure 5.12: ARXPS measurement of a sample dosed with 0.3 nm Fe. Markers denote measured signal, and the straight lines denote the model using the concentration matrix presented in Table 5.4. The angle is defined such that 0° is normal emission with respect to the sample.

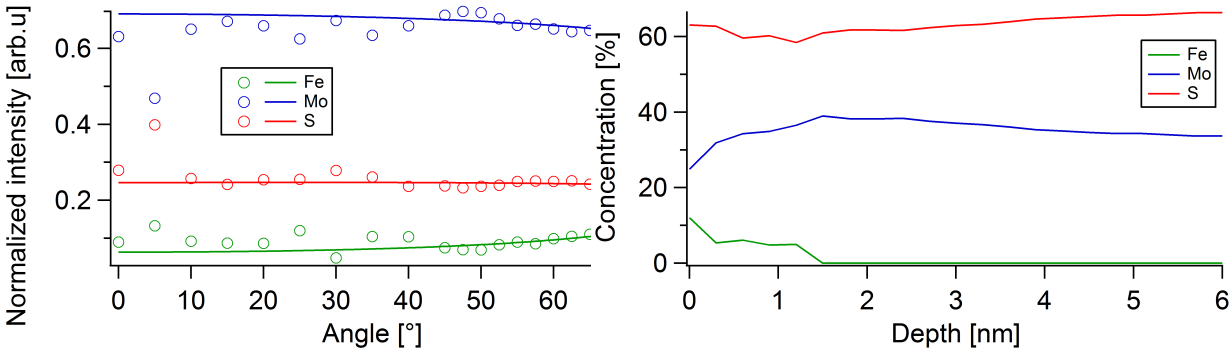

(a) ARXPS data with fit. **(b)** Concentration

Figure 5.13: (a) ARXPS data for a sample with potassium and iron on the surface heated to 400°C modelled by the multilayer model with the concentration presented in (b). Circles in (a) are experimental data and solid lines are the model fit. The vertical axis in (a) represents the intensity of each element normalized by the intensity of all elements present at each angle. The data has been modelled with a layer thickness $d = 0.3$ nm.

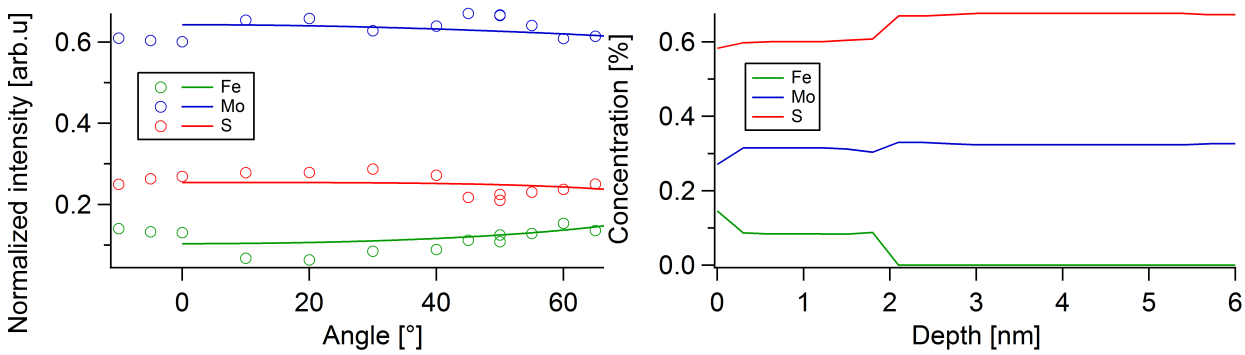

(a) ARXPS data with fit. **(b)** Concentration

Figure 5.14: (a) ARXPS data for a sample with iron on the surface heated to 500°C modelled by the multilayer model with the concentration presented in (b). Circles in (a) are experimental data and solid lines are the model fit. The vertical axis in (a) represents the intensity of each element normalized by the intensity of all elements present at each angle. The data has been modelled with a layer thickness $d = 0.3$ nm.

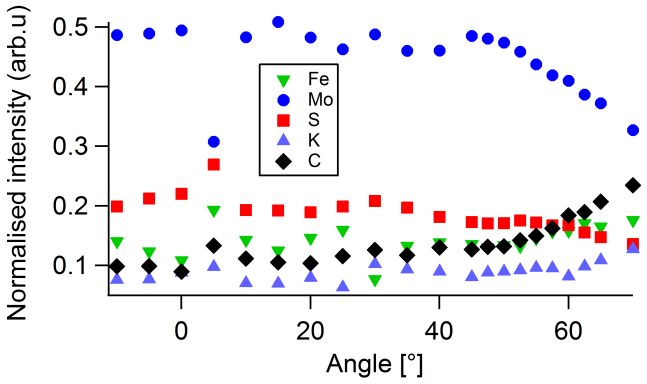

(a) ARXPS data

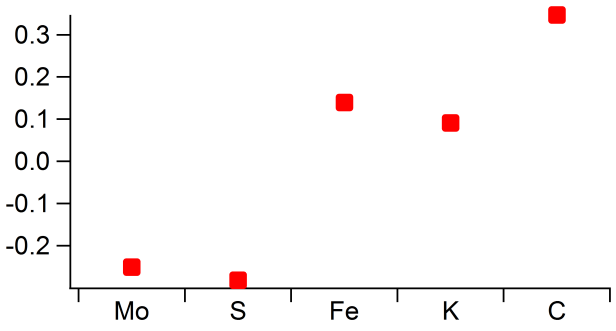

(b) Relative density plot

Figure 5.15: (a) ARXPS data for a MoS_2 sample with iron, potassium and with carbon contamination. (b) Relative density plot of the core levels, the logarithm of the intensity at 60° divided by the intensity at 0°. The vertical axis provides information where the element is with respect to the others.

5.3 Low temperature ARPES measurements (St. Andrews)

In Figure 5.16 the valence band of 2H-MoS_2, recorded along $\bar{\Gamma} - \bar{K}$, is shown. The electronic structure appears sharp, especially at the $\bar{K}$-point where the distinct spin orbit coupled split is observed. For bulk MoS2, the valence band is expected to exhibit its maximum at the $\bar{\Gamma}$ points of the Brillouin zone. However, as visible in Figure 5.16, this is not clear as the spectral weight vanishes close to the top of the valence band, hindering the exact determination of the band maximum. This strong suppression of the ARPES intensity close to normal emission is not unexpected [63–66]. It is a well known process in photoemission experiments and originates from the selection rules for transitions from initial into a final state: the photoemission matrix elements is dependent on photon energy, light polarization and geometry of the experimental setup, thus a particular combination of these parameters can alter or, as documented in Ref.[64], even suppress the ARPES intensity. This effect is most prominent at normal emission, nominally the $\bar{\Gamma}$-point in Figure 5.16.

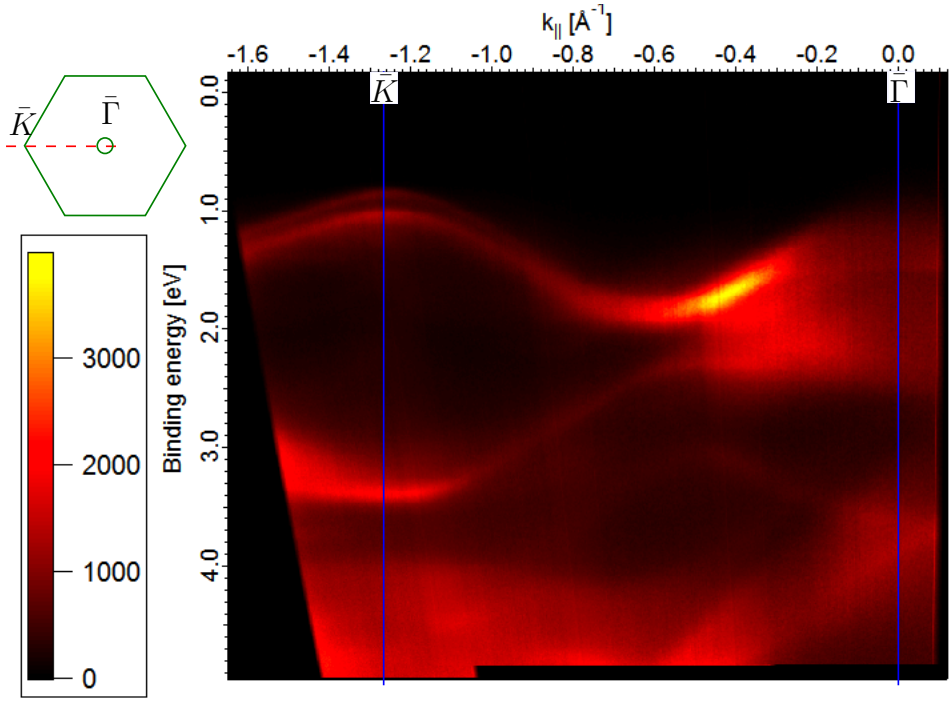

Figure 5.16: Valence bandstructure of 2H-MoS2 recorded along $\bar{K} - \bar{\Gamma}$ (as indicated by the red line in the green hexagon in the top left corner) by ARPES with photon energy $h\nu$ =21.2 eV. The intensity in the color scale is electron counts per second. Blue lines indicate the high symmetry points $\bar{K}$ and $\bar{\Gamma}$.

Several spectra from different samples were acquired at the low temperature ARPES facility in St. Andrews. In Figure 5.17 ARPES scans around the $\bar{K}$-point for four different situations are shown. The spectrum shown in the top is from the same sample as in Figure 5.16. The as cleaved spectrum show an splitting of the two bands of ∼0.16 eV, which is consistent with other observations [64, 67, 68].

After the deposition of 0.15 nm of iron to the surface the spectrum shows broader features, this is probably due to inelastic scattering on the surface due to the iron overlayer not being fully uniform. This is consistent with previous with LEED observations. The fit for this EDC in Figure 5.17 suggests there is a shift towards higher binding energy of ∼0.12 eV, with the same splitting between the two peaks at low binding energy. This shift suggests that the iron is doping the sample. At higher binding energy in both of these curves extra peaks are added. This additional intensity is part of the background, and could potentially be from an impurity band, some other band in the spectrum or as an artifact of creation of the EDC. The EDC shown in Figure 5.17 is an integration of ±1° through the $\bar{K}$-point, this integration could potentially form a new peak. It could also be flakes sticking out in an odd direction such that intensity from another place in the Brillouin zone contributes to the intensity. The same structure is also observed in Fig. 9 in Ref.[64], though seemingly larger. Another deposition giving a thickness of 0.52 nm was also performed on this sample, giving the UPS scan at normal emission shown in Figure 5.18. This shows a similar structure as what was observed in Figure 5.3, with an impurity flat band forming at the Fermi level. The ARPES signal (not shown) on the other hand was completely washed out after this deposition.

The spectrum from sample B in Figure 5.17 is interesting. After the addition of a minuscule amount of iron on the surface the spectrum seems to have split up in four separate peaks. Where the separation of the two at high binding energy is 0.13 eV, and the separation of the two at lower binding energy is 0.21 eV. Great care was made in order to ensure that this was in fact the $\bar{K}$-point, by mapping out a constant energy map shown in Figure 4.5. This splitting of the states, will be further discussed in section 6.4.

The last spectrum from sample C in Figure 5.17 is added to show how a larger amount of iron washes out the structure. There is still some kind of band, but what this is attributed to is hard to say, and the splitting of the bands due to spin orbit coupling cannot be distinguished. Towards the Fermi level there is a large background suggesting that there is the same impurity band at the Fermi level as in Figure 5.3 and 5.18.

Figure 5.19 denotes the shifts in the core levels for the sample referred to as Sample A in Figure 5.17. The peak position for the Mo 3d core level was found at 229.18 for the as cleaved sample, which is still within the range from the tabulated average value of 229.5±0.4 eV in NISTs database [62], but outside the range of what was presented earlier. Measurements on gold were carried out just before these measurements, and the calibration of the instrument was good, as the other core levels for instance iron and gold were found at their correct value. After the first deposition, the Mo 3d core level is shifted by ∼0.02 eV towards higher binding energy, and the second deposition with a larger amount of iron shifts the Mo 3d core level by ∼0.1 eV towards higher binding. For the C 1s core level in Figure 5.19 an extra peak emerges after the iron deposition. This peak could be explained by some of the iron bonding with some of the carbon, this corresponds well to $FeCO_3$ in Ref.[69]. This extra component was not observed in any other sample in this project. The shift seen in the core levels and valence band here is on the contrary to the shift seen in the core levels after iron deposition previously discussed. Suggesting that some other mechanism might be going on, this will be discussed in more details in section 6.3. The LEED measurement in Figure 5.20 may suggest that this sample has a stepped surface. For the samples referred to as sample B and sample C in

Figure 5.17 the position of the Mo 3d core level is situated at 229 eV, which is similar to what was been observed for the samples deposited with iron with the mini e-beam evaporator at room temperature. The Fe 2p core level for these samples was found at a binding energy 707.3±0.2 eV, which is within the range of tabulated values of metallic iron [62]. There were no signs of Fe^{2+} and Fe^{3+} forming in the spectrum.

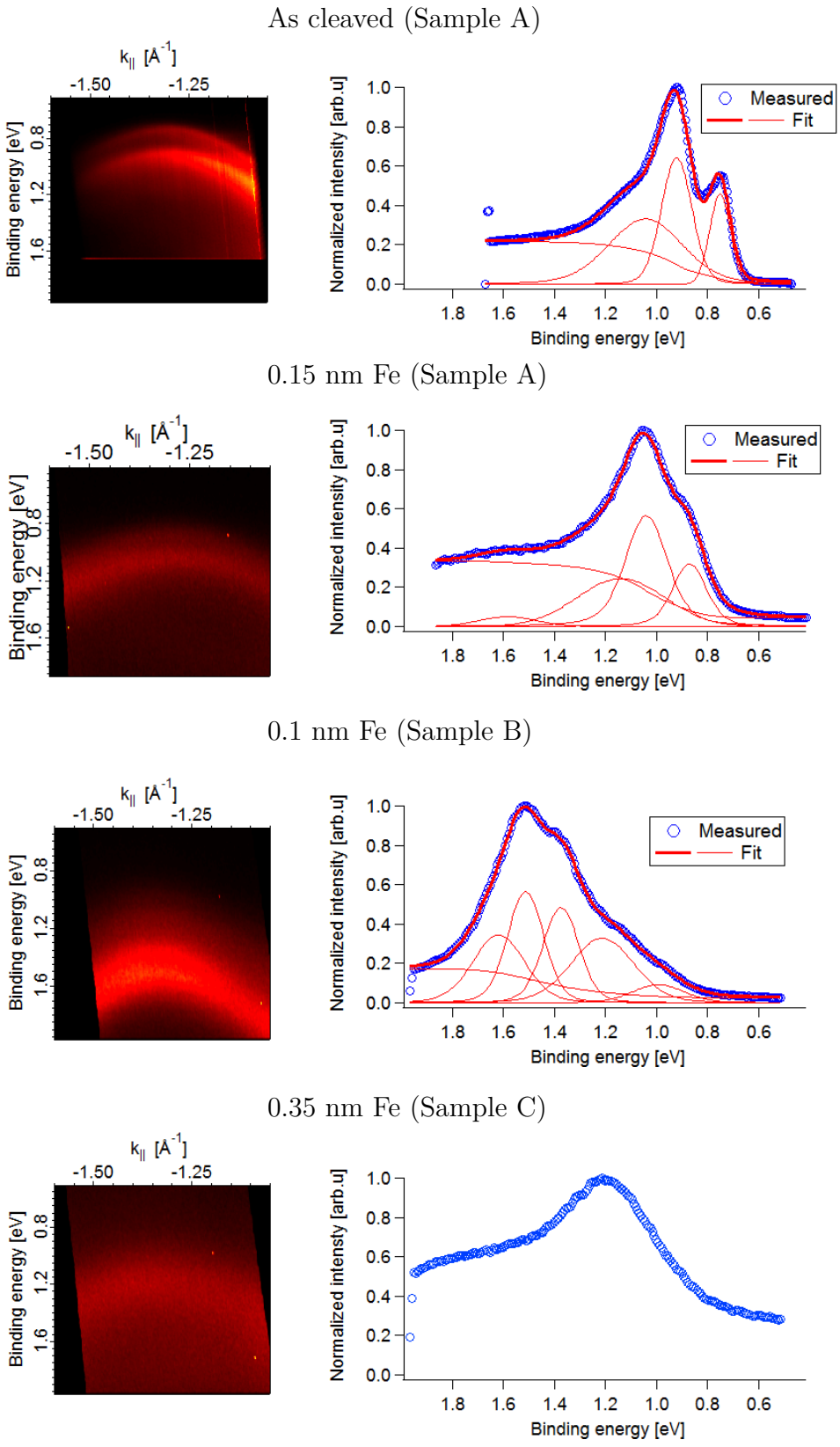

Figure 5.17: ARPES and EDCs at $\bar{K}$ for sample A as cleaved and with 0.15 nm iron, sample B with 0.1 nm iron and sample C with 0.35 nm iron. The EDCs cuts at constant $\boldsymbol{k}$ through the center of the ARPES scans. Circles in the EDCs denotes the measured data, thick solid line the model fit and thinner solid lines the components of the fit. This scan was taken at a photon energy $h\nu$ =21.2 eV with monochromated HeI$_\alpha$.

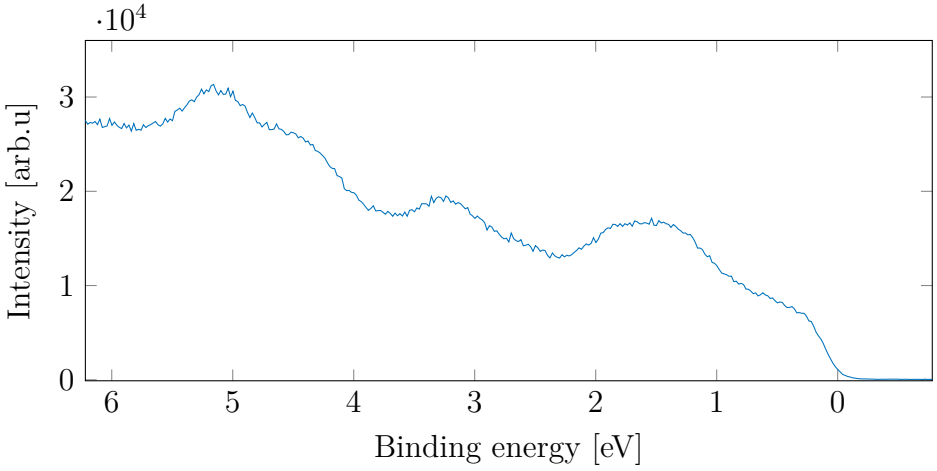

Figure 5.18: UPS scan at normal emission with 0.52 nm of iron on the surface. This scan was taken at a photon energy $h\nu$ =21.2 eV of monochromated HeI$_\alpha$.

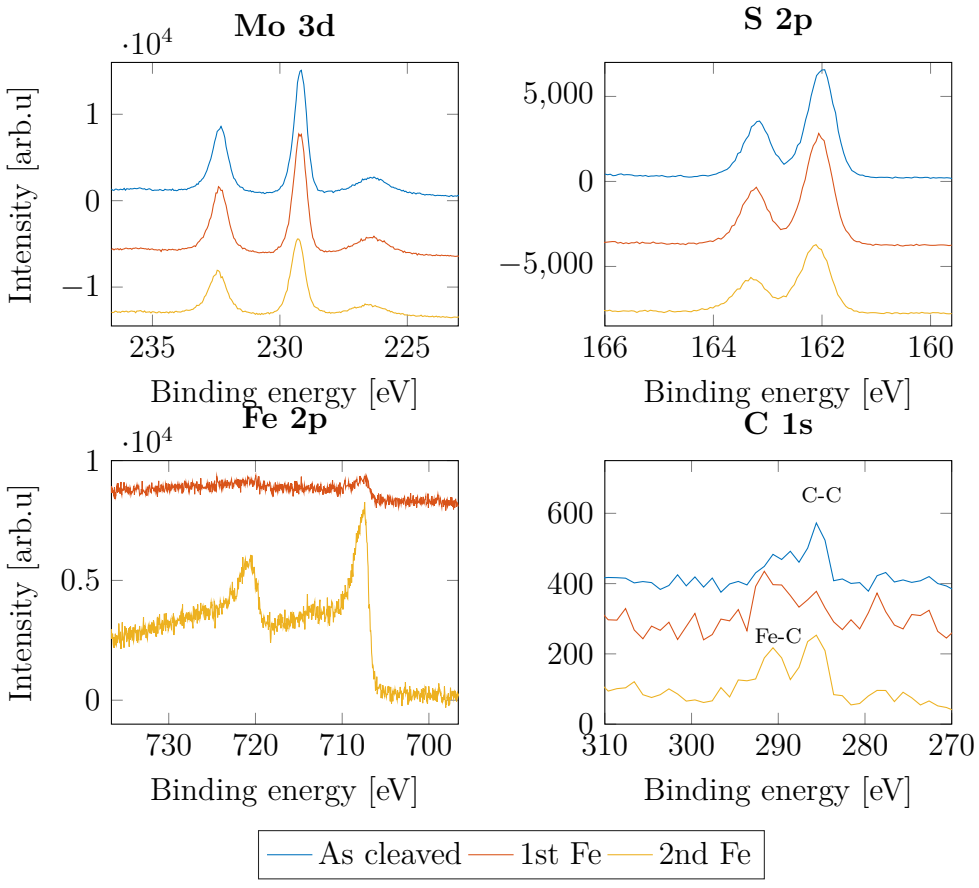

Figure 5.19: Core level XPS scans of Mo 3d, S 2p, Fe 2p and C 1s on sample A in Figure 5.17 treated with two iron depositions. The scans are acquired by a monochromated Al K$_\alpha$ source (1486.61 eV). Each scan is subtracted a constant shift, where the top most curve corresponds to the real number of counts. For Mo 3d the offset is -7000, for S 2p it is -4000, for Fe 2p it is -8000 and -140 for C 1s. The reduced quality of the scan for C 1s is due to it being taken at a different pass energy.

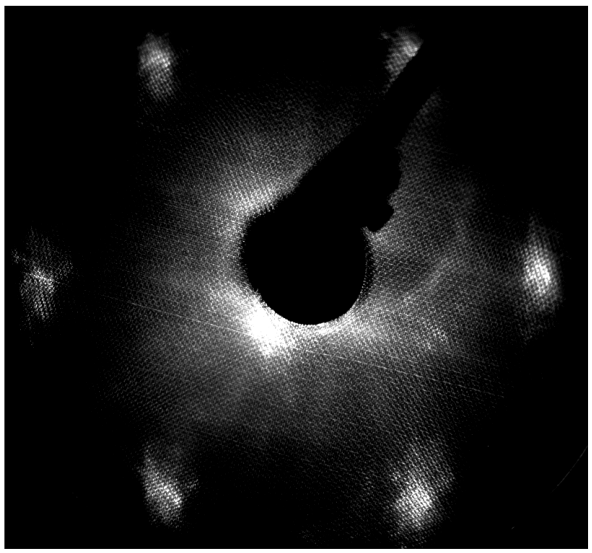

Figure 5.20: LEED measurement of sample A in Figure 5.17 at 154 eV.

6 Discussion

6.1 Growth of iron and potassium

The ARXPS measurements and model fits in Figure 5.12 suggest that iron grows in the surface region. This is also confirmed by the fit parameters presented for the model in Figures 5.10 and 5.11. If the iron was to spontaneously intercalate from the surface into the sample without annealing, there would not be a shift due to oxidization in the XPS core level as the iron would lie unreactive in van der Waals gap. Partial intercalation seems unlikely without heat treatment. The shift in the XPS measurement in Figure 5.7 after annealing to 150°C, and thereafter oxidizing the sample confirms this.

The growth of iron on the surface might not follow the ideal (Frank-van der Merwe) layer by layer growth. The iron on the surface could potentially be forming as islands or nanoparticles on the surface. A quite similar experiment on a geological MoS_2 crystal is reported in Ref.[16], where they study the growth of iron by XPS and STM. In their STM measurements they observe that iron has a 3D growth, and tend to form as nanoparticles near defects on the surface. By employing Auger electron spectroscopy to study the growth of iron on MoS_2, the authors of Ref.[70] also report that the iron has a more 3D growth on the surface of MoS_2. They report that at first iron seems to initially form as islands on the surface, which with increasing amount of iron form into three-dimensional small metallic particles on the surface. With an elevated substrate temperature, the iron starts to form 3D particles at an earlier stage of the deposition. For the measurements in this work, both assuming the formation of continuous overlayers and assuming islands forming, the models fit well. Judging from the LEED measurements, Figure 5.2, the iron does not form an ordered overlayer, as no surface reconstruction is observed in the measurements. It could grow in a layer by layer fashion, but the measurements are taken at a thickness where the layer is not fully completed. The unordered structure is further confirmed by the ARPES measurements in Figure 5.3, if the iron were to form an ordered layer on the surface would bands crossing the Fermi level be observed. In Figure 5.3 an impurity flat band is forming from the scattering of unordered metallic impurities. Still the LEED measurements in Figure 5.2 suggest that the iron overlayer must be fairly homogeneous, as the pattern is not very obstructed by the iron on the surface.

The Fe 2p spectra remain unchanged with the deposition of potassium on the sample. As can be seen in Figure 5.11, the angular relation between Mo 3d and Fe 2p stays the same. Kamaratos *et al.* [71–73] have studied the interaction of potassium on the surface of MoS_2 extensively with a potassium source from the same manufacturer of the dosers used in this work. They report that at room temperature potassium has a tendency to grow in 2D nanostructures, and that part of the potassium intercalates at room temperature. The shift in Figure 5.4 suggest the potassium is reacting with the carbon. The behaviour of

carbon in Figure 5.15, suggests that carbon is on the surface. This then suggests that potassium is also on the surface. This is further confirmed by the LEED pattern in Figure 5.5 being further obstructed after the addition of potassium. The scope of this project is not the intercalation of potassium. What is desired with the addition of potassium is to shift the Mo 3d and S 2p back to their initial position, so that in later studies band bending effects can be distinguished from magnetic effects induced by the iron. This shift is observed.

In order to be able to control the growth more carefully a different system or geometry could have been used. Ideally to track the growth of the iron as it was deposited. This can be done in several ways. If the iron was evaporated in a geometry such that LEED measurements could be performed simultaneously, would it be possible to track the growth of iron by carefully studying the intensity of diffraction spots as the iron was evaporated. By looking at the intensity profile, one could be able to count the number of monolayers grown on the surface, and could abort the deposition at the desired overlayer thickness. The ideal technique for this is Reflection high-energy electron diffraction (RHEED) [74]. RHEED is quite similar to LEED, but in RHEED the electrons are impacted sample at grazing incidence. This makes the technique more surface sensitive. By monitoring the intensity change as the layers are growing on the surface, RHEED tells a lot about surface growth. Such monitoring could also be done by XPS. In Ref.[75], they monitor the growth of Cu on Pd(111) RHEED and XPS. By continuously monitoring intensity of the substrate against the deposited element, they are able to get information about growth on the surface. By reducing the deposition rate, such monitoring would be possible in the homelab, and it would be possible to get more information about the growth modes. Direct measurements after the iron is grown on the surface would also provide valuable information. Doing a similar study with STM as they do in Ref.[16] would give information about the morphology on the surface. Similarly would a study by SEM provide useful information about the morphology of the surface.

It can be concluded that the surface growth of iron is not simple, the iron is most likely forming some kind of unordered structure with fairly good coverage on the surface. The growth of iron on the samples measured in St. Andrews most likely follow the same growth modes, but could be more complicated, as different behaviours are observed. This will be further discussed in section 6.3.

6.2 Behaviour of iron after heat treatment

The behaviour of iron after heat treatment is far more complicated. As can be seen in Figures 5.11 and 5.10, there is definitely a change after heating. The two models provide slightly different information. The multilayer model in Figures 5.13 and 5.14 suggests that the iron has diffused into the structure of the MoS_2, which suggests intercalation. Heating to 500°C causes a diffusion deeper into the bulk, whereas heating to 400°C with potassium also on the surface suggests that iron has intercalated slightly shallower than in the first case. For both cases the multilayer model suggests that there is a higher concentration in the 0th layer, the surface. These fits then suggest intercalation with some iron still left on the surface. The problem with the multilayer model is that it does not handle 3D

structure formation on the surface, as it assumes that each layer is homogeneous.

3D structure formation is better handled by the intercalation/agglomeration model. Island formation, 3D structure formation and intercalation give similar profiles for ARXPS measurements, but still it is possible to distinguish them. The fit for the sample heated to 400°C in Figure 5.11 and Table 5.3, suggest that after heating the iron has formed either a low coverage of tall 3D structures, or iron has diffused into the first two unit cells of the MoS_2 at a concentration of 15%. The last interpretation seems more plausible. The fit also provides a conservation to some extent of the iron. Compared to the multilayer model, this fit suggests a deeper intercalation of the iron at a higher concentration. For the sample heated to 500°C, both of the fits in Figure 5.10 suggest some kind of clustering, as opposed to the multilayer model. The fit with the restricted range in Table 5.2 is the most plausible, where the surface is mostly covered with islands, since the other fit seems to be fitting to points outside the trend. What is not considered in the model for islands is the possibility of shadowing effects. It has been assumed that islands are small, such that this will not have an effect on the model. At larger angles the emitted electrons might pass through neighbouring nanostructures on the surface, and thus will cause a different attenuation. In Ref.[76] they study this and report that island formation and surface roughness quickly complicates ARXPS measurements.

The ARXPS measurements are prone to a lot of uncertainties and their accuracy is hard to determine for this case. Photoelectric diffraction is observed for these measurements, and it obstructs the profile of the measurements. Ideally if an azimuthal rotation was possible, the sample would have been rotated to an angle where less diffraction would occur within measurement range. If the surface of the sample is not entirely flat or flakes from the cleave are sticking up, this can influence the data. Samples that did not look flat or had flakes that could be observed visually were rejected before measurements were carried out, but still there could be flakes obstructing on a lower scale. The detection area can change as the sample is rotated. If the detection area at normal emission is a circle, the detection area will be an elongated ellipse at higher angles. Thus changing the sensitivity of the measurement.

These models are not entirely conclusive. For the sample heated to 400°C with potassium, both models suggest some kind of intercalation, and for the sample heated to 500°C they do not agree. The XPS data in Figure 5.8 show a reduced band bending after heating, this may suggest in the direction of agglomeration. As the surface is getting less and less covered the effect of the band bending is reduced. In Ref.[77] this is an argument for agglomeration. What is interesting is that there is no shift or significant change in the Fe 2p core level after heating, other than the intensity being attenuated. It could be expected that if iron was situated in the van der Waals gap it would be in a different chemical environment, and would thus give a shift or an extra component to the peak. This is on the other hand is not observed. A combination of intercalation and 3D surface growth is probably the most likely case with the possibility of potassium on the surface promoting intercalation. Other sources report that in this temperature range it is most likely agglomeration happening [15, 77]. Kamaratos *et al.*[15] provide a convincing report, and observe intercalation first after 20 cycles of evaporation of iron on the surface and heating the sample to 1200 K. This is observed by Ar^+ sputtering and measuring the change in the respective Auger peaks. They also report that after 900 K the iron starts

to desorb from the surface. In a later study Kamaratos *et al.*[78] report observing a 2x2 LEED pattern forming after heating to 1200 K, suggesting that the small amount left on the surface forms an ordered structure. In Ref.[77] they report that the surface is destroyed after heating to 1200 K. They also report chemical reactions between sulphur and iron, which in this work there is no evidence for. The relation between the intensity of the sulphur and molybdenum core levels does not change upon heating or the addition iron, nor does the FWHM change after heating or addition of iron change. This suggests that there are no chemical reactions with the iron and sulphur, which potentially could be happening. In Ref.[79] they report the intercalation. They create their structures by laser depositing MoS_2 on top of iron, and form iron sulfides and intercalates iron upon heating. They argue that for higher temperatures that iron sulfides and the Fe-MoS_2 compounds reduces back to metallic iron and MoS_2.

In Ref.[80] they study the intercalation with Conversion electron Mössbauer spectroscopy (CEMS) and XPS. They have an excess of sulphur, which many of these sources report, which is not observed in this work. They report that upon heating, iron agglomerates on the surface, and the excess sulphur is transferred to the iron. They also observe some intercalation already at 423K by CEMS. The intercalation is observed outside of the sampling depth of XPS. In Ref.[81] the same group increases the intercalation by Ar^+ sputtering the surface, creating defects to transport the iron into the crystal structure.

In further work studies with different experimental techniques should be employed, to gain further confidence about the intercalation of iron. SEM and STM can be used to look at the surface in real space, to track the evolution of the iron overlayer with temperature. Further and longer heating steps have to be employed, keeping an eye on how the sulphur behaves as this is reported to react with the surface iron at higher temperatures [80]. One must also consider the possibility that high quality iron intercalated crystals cannot be achieved in this way. Perhaps intercalation when synthesising a MoS_2 crystal is simpler. It would also be worth considering using artificially synthesised MoS_2 crystals, as these might have less contamination and defects. Comparing if a crystal with more defects will have better features for intercalation. On the other hand, defects in a crystal will not give nice ARPES measurements, and is thus not that interesting for further work. A destructive study about the intercalation could also be carried out, investigating how much of the iron that intercalates and how much of the iron that agglomerates on the surface. Still there is the possibility of our heated samples giving interesting ARPES spectrum, the UPS lamp was out of service when the thermal treatments were carried out. The sharp LEED pattern in Figure 5.9 suggests that the surface quality is good, this suggest that good band structure measurement can be achieved. This has to be investigated in further work.

If iron is not a suitable material, other elements that can provide magnetism can be investigated, such as nickel and cobalt for intercalation or as a surface thin film. As stated in Ref.[15] palladium and nickel tends to diffuse uniformly into the crystal structure of MoS_2, which suggest that they might have decent properties for intercalation.

6.3 Different chemical shifts

The core levels in Figure 5.19 and the EDCs in Figure 5.17 showed a different shift than what observed for the measurements performed at the XPS laboratory at NTNU.

The UPS/ARPES and XPS scans of the core levels taken at the XPS laboratory at NTNU is consistent with what are observed in Ref.[77]. For a deposition of 0.6 nm of iron, in this work it is observed a shift towards lower binding energy of ∼0.3 eV and ∼0.4 eV for the core levels. They observe a shift of ∼0.4 eV for a deposition of 0.1 nm, with the same metallic flat band forming at the Fermi edge. For an overlayer of 0.3 nm to 1 nm they observe that the spectrum from MoS_2 has more or less disappeared. This can be explained by different inelastic mean free paths for the two experiments. Their experiments are taken at a photon energy of 152 eV, whereas the experiments in this work are taken at 21.2 eV. In Figure 3.5, a photon energy of 152 eV has a shorter IMFP than a photon energy of 21.2 eV, this leaves them more surface sensitive, and can explain why the bands are disappearing. The shift in the valence band and core levels can be explained by band bending. Band bending arise as an energy offset in the band structure of a semiconductor near a junction, due to space charge effects. In a junction between a metal and a semiconductor like in this work, the semiconductor's Fermi level is pinned to the metals Fermi level, shifting the core levels and the valence band. Band bending is not dependent on temperature or magnetic field, but is an effect of the electric field in the junction [82].

Since MoS_2 is a semiconductor, charging with the photoemission process could be happening. This is an effect where the photoemission process depletes the sample for electrons, which if not replenished causes a positive charge of the sample. This will be a potential that attracts the electrons on their way out of the sample, which shifts the spectrum to higher binding energy. This seems as an unlikely explanation since twin anode X-ray gun in the XPS laboratory at NTNU produces secondary electrons in the collision with the anode material, and these will replenish the lost electrons in the sample. As stated earlier the binding energy of the core level also correspond well to tabulated sources for MoS_2. In St. Andrews the spectrum is found at lower binding energy than the tabulated values, so it cannot be charging.

What could be happening for the measurements in Figures 5.17 and 5.19 is inhomogeneous band bending due to a stepped surface. Ref.[65] has done a thorough study on this phenomena, and report shifts as great as 2 eV for a surface with high step densities compared to a flat surface. This is a local Fermi level pinning caused by electric field gradients forming at the surface by charged dislocations from regions of high step densities. As can be seen in their report they still manage to acquire good ARPES data, even though they have a stepped surface. The LEED pattern in Figure 5.20 may suggest a similar stepped surface as in Figure 1c in Ref.[65]. The samples in St. Andrews were cleaved by the top post method, whereas the samples in the XPS laboratory at NTNU were cleaved by the scotch tape method. The top post method could for some of the samples induce higher step densities and therefore change the surface potential, leaving the core levels observed at a different binding energy as in Figure 5.19. A stepped surface could introduce edge states that changes how the iron bonds with the surface. This could change the shifts observed for the core levels and valence band, and can possibly explain what is observed.

The iron source used in St. Andrews could induce contamination onto the surface. The source is two twisted iron and tungsten wires. It is possible that tungsten also evaporates onto the surface, but there were no signs of tungsten in the spectrum. There could also be carbon contamination on the evaporator that reacts with iron in the evaporation process. If small amounts of iron-carbides are forming this could change how the iron reacts with the surface. The formation of an iron-carbide is likely what is observed for C 1s in Figure 5.19. Iron-carbide on the surface will give a different potential, a different band bending and hence a different shift in the core levels. Which probably is the most likely explanation for the n-doping of sample A in Figure 5.17. This iron-carbide formation was not observed for any other samples.

The details of the different shifts is not fully understood, and a repetition of the experiments with more similar experimental conditions needs to be carried out. For instance should the more controllable mini e-beam evaporator used in the XPS laboratory at NTNU, also have been used at the low temperature ARPES facility in St. Andrews. In this way the film thickness and coverage would be more similar, and it could be possible to distinguish what effect is going on. Still the ARPES data taken in St. Andrews provide interesting information and cannot be disregarded.

6.4 ARPES

The ARPES acquired in the XPS laboratory at NTNU in Figure 5.3 provide the information that there is a constant shift, a flat impurity band at the Fermi level and the bands are still dispersing. It provides information about growth quality and leads the way for further studies. The shift back to the initial position in the core levels induced by the deposition of potassium leads the way to separate the effects of band bending from magnetic effects. Unfortunately the UPS lamp was out of service at this point of the measurements, so a detailed study of the valence band will have be to carried out later.

For the ARPES data acquired in St. Andrews it can be understood that making heterostructures with a ferromagnetic overlayer on top of semiconducting MoS_2 is complicated. In order get good band structure measurements a better control of the thin film growth needs to be achieved, and then the interactions between the two structures can be investigated.

Smaller deposited amounts like on sample A in Figure 5.17, where n-type doping is observed, warrants a more detailed study. It has to be distinguished whether this shift is due to a complicated morphology of the surface or due to the iron-carbide that forms on this sample. If iron-carbide is the origin of the doping, this is still interesting to examine. Ref.[30] suggest that cluster doping with iron and different elements, like carbon, may be a strategy to explore diluted magnetic semiconductors. Having a semiconducting and ferromagnetic behaviour might pave the way to the creation of a dilute magnetic semiconductors with MoS_2 [12]. The information of the bulk doping can hopefully be transferred to monolayer MoS_2 to be able to make 2D dilute magnetic semiconductors. This is a unsolved problem in physics. How can materials that show both ferromagnetic properties and semiconducting properties at room temperature be made? A dilute magnetic semiconductor combines ferromagnetic properties and semiconducting properties to provide

new ways for conduction. In normal electronics the control is of charge carriers, but with a magnetic semiconductor the quantum spin state can be controlled [13]. Further experiments with low amounts of iron needs to be carried out together with a detailed study of the magnetic properties of the material.

The spectrum for sample B in Figure 5.17 is interesting. What is happening could be described by Figure 6.1. The iron on the surface of the MoS_2 causes a potential that strongly affects the band structure in the first layer, but not as strongly for the second layer, causing a shift between the band structures in the two layers. Normally, the band structure of bulk MoS_2 would be as in Figure 2.5, but with a surface potential, the two layers will shift differently causing a splitting as seen in Figure 6.1. This has been observed for rubidium doping on WSe_2 [83]. For a shift like this it would be expected that the separation of the bands corresponding to each layer would be constant. The pairwise separation observed for sample B in Figure 5.17 is ∼0.3 eV and ∼0.38 eV, thus much larger than the expected split of ∼0.16 eV [64]. The splitting could also be due to magnetic impurities lifting the time reversal symmetry of the crystal, causing a splitting due to magnetism. The Zeeman splitting and Landau levels described in section 2.3 would be too weak effects to consider for this. Large field strengths are required to observe these two effects, and Ref.[16] report that an overlayer of 6 monolayers is required to induce a magnetic field in the iron film. Still other effects due to magnetic impurities and the potential at the surface can possibly explain this. In order to disentangle this a larger part of the band structure must be acquired and modelled. The observed spectra could also be due to poor sample quality. The sample looked good by LEED and eye, but there could still be a dent in the sample, such that intensity from other parts of the Brillouin zone could be contributing. Further work needs be done to distinguish why the bands are splitting in sample B and not sample A in Figure 5.17.

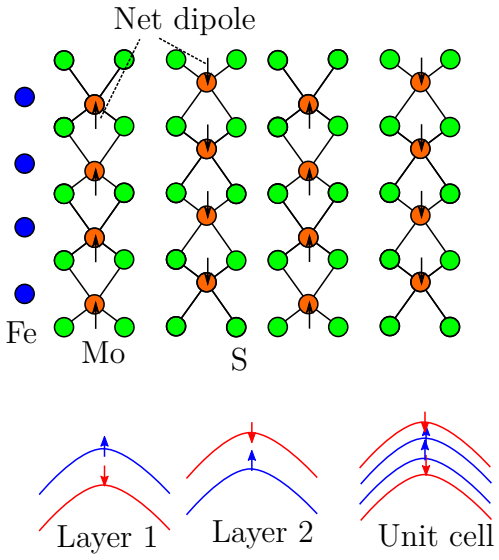

Figure 6.1: Iron on the surface causes a potential that band bends the top layer with a different strength than the second layer, causing a splitting of the band structure for the unit cell.

7 Conclusion

7.1 Concluding remarks

In this work, the growth of iron on MoS_2 and the behaviour of iron after annealing has been studied. The reason behind this study is to understand the growth mechanism, such that an intricate system can be created to study the magnetic influence from iron on the already spin polarized band structure of MoS_2. The influence of magnetic impurities in a spin-orbit coupled environment would potentially allow for all spins manipulation: by controlling the layer-by-layer growth of a magnetic overlayer, ideally, one would be able to access new routes towards the fabrication of spin-based devices, where the control of even a single electron spin is crucial

The measurements were carried out using XPS, LEED and UPS in the XPS laboratory at NTNU to study the growth of iron and the behaviour after annealing. The results show that the iron grows fairly smoothly on the surface, and does not seem to intercalate at room temperature. The addition of iron to the surface causes band bending in the core levels and in the valence band, with an average shift of 0.41 ± 0.07 eV towards lower binding energy. It has been shown that by counterdoping with iron and potassium the core levels shift back to the position of as a pristine cleaved MoS_2 surface, compensating for the effect of banding induced by the growth of iron. This can later be used to decouple magnetic effects from band bending.

The results from annealing the sample have shown that the iron changes it's spatial configuration on the surface. It has been shown that by modelling the changes of a sample dosed with iron and potassium and annealed to 500°C by two separate models, that the iron could be intercalating into the first 1-2 unit cells with some iron left on the surface. The models were inconclusive for the sample that was annealed to 500°C with only iron on the surface. This suggests that both intercalation and 3D particle growth could be happening. Sharp LEED patterns after annealing suggest that the surface quality is good. ARPES measurements carried out in the XPS laboratory at NTNU showed that a flat band formed at the Fermi level due to scattering of electrons with metallic impurities after a deposition of 0.6 nm of iron.

A preliminary low temperature ARPES study was carried out in the electronic structure laboratory in St. Andrews. This showed that for lower doses of iron the semiconducting behaviour of MoS_2 was preserved. One sample showed n-type doping without a change in the splitting of the bands. The n-type doping could be explained by inhomogeneous band bending or iron-carbide forming on the surface. Another sample showed a splitting of the two bands at the $\bar{K}$-point into four, which could originate from an electrical potential and magnetic effects due to iron on the surface.

The findings in this report confirm that the TMDCs are strongly interacting, and further understanding of the interactions and control of these systems could pave the way for spintronics for a new generation of multifunctional electronic devices.

7.2 Further work and outlook

Through this work a further understanding of the growth of iron on MoS_2 has been gained. There are still further questions to be asked. Is it possible to get an epitaxial layer by layer growth? To gain more information about the growth real space probing by STM, AFM or SEM would provide valuable information of the surface morphology. These techniques can be used to check where the iron grows, and measures can be taken in order to change the surface growth. If for instance the iron grows around defects, a better surface quality is needed. Changing parameters such as temperature and deposition rate could potentially change the growth mechanism. By monitoring the growth by RHEED it is possible to be more confident about the growth, and it would be possible to monitor the growth mechanism as a function of external parameters. By reducing deposition rate and monitoring growth as the iron deposited with XPS could also provide valuable information.

To gain more confidence about intercalation destructive testing might be a viable option, by for example argon sputtering the surface of the MoS_2. Then layer by layer can be sputtered away, whilst monitoring the signal from the molybdenum, sulphur and iron core levels with XPS. This would give more confidence on how much of the iron that has intercalated and how much of the iron that agglomerates on the surface. Studying the surface after heat treatment with microscopy techniques could also provide valuable information about the agglomeration on the surface.

If iron is not a suitable material, other magnetic elements can be investigated, such as nickel and cobalt for intercalation or as a surface thin film. Even if iron is a suitable material it would be interesting to investigate how other magnetic materials interact with MoS_2, and how the properties might change.

New ARPES measurements at a synchrotron facility will have to be carried out, with a more detailed study of how the band structure is influenced by the magnetic phase introduced by the iron. This could be carried out by changing the deposition, as the data acquired in St. Andrews show interesting features for lower doses of iron. This could potentially pave the way for dilute magnetic semiconductors, which would be a great technological advancement. The information acquired on MoS_2 can also be used to do research on other TMDCs with even more interesting phases, such as superconductivity, charge density waves and spin density waves, to develop a further understanding for how these mechanisms develop and how they change their properties with the introduction magnetic fields and magnetic impurities.

Bibliography

1. Novoselov, K. S. *et al.* Electric field effect in atomically thin carbon films. *science* **306,** 666–669 (2004).
2. Riley, J. *et al.* Direct observation of spin-polarized bulk bands in an inversion-symmetric semiconductor. *Nature Physics* **10,** 835–839 (2014).
3. Bawden, L. *et al.* Spin-valley locking in the normal state of a transition-metal dichalcogenide superconductor. *Nature communications* **7** (2016).
4. Zhang, X., Liu, Q., Luo, J.-W., Freeman, A. J. & Zunger, A. Hidden spin polarization in inversion-symmetric bulk crystals. *Nature Physics* **10,** 387–393 (2014).
5. Rahn, D. *et al.* Gaps and kinks in the electronic structure of the superconductor 2 H-NbSe 2 from angle-resolved photoemission at 1 K. *Physical Review B* **85,** 224532 (2012).
6. Xi, X. *et al.* Ising pairing in superconducting NbSe2 atomic layers. *Nature Physics* (2015).
7. Li, L. *et al.* Fe-doping–induced superconductivity in the charge-density-wave system 1T-TaS2. *EPL (Europhysics Letters)* **97,** 67005 (2012).
8. Kim, C. M., Kim, C. S., Kim, S. B. & Hahn, E. J. Magnetic properties of Fe-doped 2H-TaS2. *Journal of the Korean Physical Society* **60,** 79–82. ISSN: 1976-8524 (2012).
9. Li, L. *et al.* Superconductivity of Ni-doping 2H–TaS 2. *Physica C: Superconductivity* **470,** 313–317 (2010).
10. Polesya, S., Mankovsky, S., Ködderitzsch, D., Bensch, W. & Ebert, H. Dzyaloshinskii–Moriya interactions and magnetic texture in Fe films deposited on transition-metal dichalcogenides. *physica status solidi (RRL)-Rapid Research Letters* **9999** (2015).
11. Wolf, S. *et al.* Spintronics: a spin-based electronics vision for the future. *Science* **294,** 1488–1495 (2001).
12. Cheng, Y., Zhu, Z., Mi, W., Guo, Z. & Schwingenschlögl, U. Prediction of two-dimensional diluted magnetic semiconductors: doped monolayer MoS 2 systems. *Physical Review B* **87,** 100401 (2013).
13. Dietl, T. A ten-year perspective on dilute magnetic semiconductors and oxides. *Nature materials* **9,** 965–974 (2010).
14. Spalvins, T. A review of recent advances in solid film lubrication. *Journal of Vacuum Science & Technology A* **5,** 212–219 (1987).
15. Kamaratos, M. & Papageorgopoulos, C. Intercalation of MoS2 (0001) with Fe, Ni and Pd. *Solid state communications* **61,** 567–569 (1987).
16. Hsu, H.-C. *et al.* Surface morphology, magnetism and chemical state of Fe coverage on MoS 2 substrate. *Applied Surface Science* **357,** 551–557 (2015).
17. Commons, W. *Molly Hill molybdenite* <`https://commons.wikimedia.org/wiki/File:Molly_Hill_molybdenite.JPG`> (2008).

18. Schönfeld, B., Huang, J. & Moss, S. Anisotropic mean-square displacements (MSD) in single-crystals of 2H-and 3R-MoS2. *Acta Crystallographica Section B: Structural Science* **39,** 404–407 (1983).
19. Finteis, T. *et al.* Occupied and unoccupied electronic band structure of WSe 2. *Physical Review B* **55,** 10400 (1997).
20. Hemmer, P. C. *Kvantemekanikk* (Tapir, 1980).
21. Winkler, R., Papadakis, S., De Poortere, E. & Shayegan, M. *Spin-Orbit Coupling in Two-Dimensional Electron and Hole Systems* (Springer, 2003).
22. Yuan, H. *et al.* Zeeman-type spin splitting controlled by an electric field. *Nature Physics* **9,** 563–569 (2013).
23. Hunvik, K. W. B. *Spin-resolved spectroscopic study of $NbSe_2$* MA thesis (NTNU, 2015).
24. Winkler, R. in *Spin–Orbit Coupling Effects in Two-Dimensional Electron and Hole Systems* 131–150 (Springer, 2003).
25. Lu, J. *et al.* Evidence for two-dimensional Ising superconductivity in gated MoS2. *Science* **350,** 1353–1357 (2015).
26. Saito, Y. *et al.* Superconductivity protected by spin-valley locking in ion-gated MoS2. *Nature Physics* (2015).
27. Li, Y. in *Probing the Response of Two-Dimensional Crystals by Optical Spectroscopy* 55–64 (Springer, 2016).
28. MacNeill, D. *et al.* Breaking of valley degeneracy by magnetic field in monolayer MoSe 2. *Physical review letters* **114,** 037401 (2015).
29. Aivazian, G. *et al.* Magnetic control of valley pseudospin in monolayer WSe2. *Nature Physics* (2015).
30. Feng, N. *et al.* First principles prediction of the magnetic properties of Fe-X6 (X= S, C, N, O, F) doped monolayer MoS2. *Scientific reports* **4** (2014).
31. Zou, F., Zhu, L., Gao, G., Wu, M. & Yao, K. Temperature-controlled spin filter and spin valve based on Fe-doped monolayer MoS 2. *Physical Chemistry Chemical Physics* (2016).
32. Lu, S.-C. & Leburton, J.-P. Electronic structures of defects and magnetic impurities in MoS2 monolayers. *Nanoscale research letters* **9,** 1–9 (2014).
33. Yin, M., Wang, X., Mi, W. & Yang, B. First principles prediction on the interfaces of Fe/MoS 2, Co/MoS 2 and Fe 3 O 4/MoS 2. *Computational Materials Science* **99,** 326–335 (2015).
34. Commons, W. *Growth modes of thin films* <`https://en.wikipedia.org/wiki/File:GrowthModes.png`> (2007).
35. Venables, J., Spiller, G. & Hanbucken, M. Nucleation and growth of thin films. *Reports on Progress in Physics* **47,** 399 (1984).
36. Emery, N., Hérold, C., Marêché, J.-F. & Lagrange, P. Synthesis and superconducting properties of CaC6. *Science and Technology of Advanced Materials* (2016).
37. Schöllhorn, R. Intercalation chemistry. *Physica B+ C* **99,** 89–99 (1980).
38. Hüfner, S. *Photoelectron spectroscopy: principles and applications* (Springer Science & Business Media, 2013).
39. Damascelli, A. Probing the electronic structure of complex systems by ARPES. *Physica Scripta* **2004,** 61 (2004).
40. Als-Nielsen, J. & McMorrow, D. *Elements of Modern X-ray Physics* 2nd ed. (Wiley, 2011).

41. Hofmann, P. *Surface Physics: An Introduction* 1.3 (Philip Hofmann, 2013).
42. Nordling, C., Sokolowski, E. & Siegbahn, K. Precision method for obtaining absolute values of atomic binding energies. *Physical Review* **105,** 1676 (1957).
43. Sokolowski, E., Nordling, C. & Siegbahn, K. Magnetic analysis of x-ray produced photo and auger electrons. *Arkiv Fysik* **12** (1957).
44. SPECS. *Manual for the Phoibos Hemispherical Energy Analyzer Series* 2006.
45. Commons, W. *Auger Process* <https://commons.wikimedia.org/wiki/File:Auger_Process.svg> (2007).
46. Tougaard, S. *QUASES-IMFP-TPP2M Ver.3.0* http://quases.com/products/quases-imfp-tpp2m/. 2016.
47. Tanuma, S., Powell, C. & Penn, D. Calculations of electron inelastic mean free paths. *Surface and Interface Analysis* **37,** 1–14 (2005).
48. Seah, M. & Dench, W. Quantitative electron spectroscopy of surfaces: a standard data base for electron inelastic mean free paths in solids. *Surface and interface analysis* **1,** 2–11 (1979).
49. Zbigniew, P. *Universal curve IMFP* <http://users.uj.edu.pl/~ufpostaw/2_Pracownia/D1/images/jak_ba1_eng.png>.
50. Shirley, D. A. High-resolution X-ray photoemission spectrum of the valence bands of gold. *Physical Review B* **5,** 4709 (1972).
51. Tougaard, S. Practical algorithm for background subtraction. *Surface Science* **216,** 343–360 (1989).
52. Fischer, T. *Angle Resolved XPS Application Note: 31014* https://www.thermofisher.com/content/dam/tfs/ATG/CAD/CAD\%20Documents/Application\%20&\%20Technical\%20Notes/Surface\%20Analysis/D16069~.pdf.
53. Jablonski, A. *NIST electron effective-attenuation-length database* http://www.nist.gov/srd/nist82.cfm. 2011.
54. Livesey, A. & Smith, G. The determination of depth profiles from angle-dependent XPS using maximum entropy data analysis. *Journal of electron spectroscopy and related phenomena* **67,** 439–461 (1994).
55. SPECS. *Manual for the XR50 X-ray Source* 2006.
56. SPECS. *Manual for the FOCUS 500 X-ray Monochromator*
57. Commons, W. *Ewald sphere* <https://commons.wikimedia.org/wiki/File:Ewaldsphere1.png> (2008).
58. Commons, W. *Rotary vane pump* <https://commons.wikimedia.org/wiki/File:Rotary_vane_pump.svg> (2006).
59. Ultra-high vacuum (UHV) pages, P. H. *Scroll pump* <http://philiphofmann.net/ultrahighvacuum/ind_scrollpump.html>.
60. Commons, W. *Cut through turbomolecular pump* <https://commons.wikimedia.org/wiki/File:Cut_through_turbomolecular_pump.jpg> (2005).
61. Research, O. A. *Manual for Mini e-beam evaporator*
62. Naumkin, A. V., Kraut-Vass, A. & Powell, C. J. *NIST X-ray photoelectron spectroscopy database* (Measurement Services Division of the National Institute of Standards and Technology (NIST) Technology Services, 2008).
63. Jin, W. *et al.* Direct measurement of the thickness-dependent electronic band structure of MoS 2 using angle-resolved photoemission spectroscopy. *Physical review letters* **111,** 106801 (2013).

64. Böker, T. *et al.* Band structure of MoS 2, MoSe 2, and α- MoTe 2: Angle-resolved photoelectron spectroscopy and ab initio calculations. *Physical Review B* **64,** 235305 (2001).
65. Mahatha, S. & Menon, K. S. Inhomogeneous band bending on MoS2 (0001) arising from surface steps and dislocations. *Journal of Physics: Condensed Matter* **24,** 305502 (2012).
66. Zhu, Z., Cheng, Y. & Schwingenschlögl, U. Giant spin-orbit-induced spin splitting in two-dimensional transition-metal dichalcogenide semiconductors. *Physical Review B* **84,** 153402 (2011).
67. Xiao, D., Liu, G.-B., Feng, W., Xu, X. & Yao, W. Coupled spin and valley physics in monolayers of MoS 2 and other group-VI dichalcogenides. *Physical Review Letters* **108,** 196802 (2012).
68. Suzuki, R. *et al.* Valley-dependent spin polarization in bulk MoS2 with broken inversion symmetry. *Nature nanotechnology* **9,** 611–617 (2014).
69. Biesinger, M. C. *et al.* Resolving surface chemical states in XPS analysis of first row transition metals, oxides and hydroxides: Cr, Mn, Fe, Co and Ni. *Applied Surface Science* **257,** 2717–2730 (2011).
70. Kamaratos, M. & Papageorgopoulos, C. A study of the behavior of Fe and Ni on MoS 2. *Solid state communications* **49,** 715–718 (1984).
71. Kamaratos, M., Vlachos, D. & Papageorgopoulos, C. Potassium adsorption on MoS2 (0001) at low temperature. *Journal of Physics: Condensed Matter* **5,** 535 (1993).
72. Papageorgopoulos, C., Kamaratos, M., Kennou, S. & Vlachos, D. Coadsorption of K and O 2 on MoS 2 (0001). *Surface science* **277,** 273–281 (1992).
73. Papageorgopoulos, C., Kamaratos, M., Kennou, S. & Vlachos, D. The behavior of K on the basal plane of MoS 2. *Surface Science* **251,** 1057–1061 (1991).
74. Laukkanen, P., Sadowski, J. & Guina, M. in *Semiconductor Research* 1–21 (Springer, 2012).
75. De Siervo, A. *et al.* Growth study of Cu/Pd (111) by RHEED and XPS. *Surface science* **575,** 217–222 (2005).
76. Martin-Concepcion, A., Yubero, F., Espinos, J. & Tougaard, S. Surface roughness and island formation effects in ARXPS quantification. *Surface and interface analysis* **36,** 788–792 (2004).
77. Lince, J. R. *et al.* Photoelectron spectroscopic study of the interaction of thin Fe films with the MoS 2 (0001) surface. *Surface Science* **223,** 65–81 (1989).
78. Kamaratos, M. & Papageorgopoulos, C. Adsorption properties of Fe on MoS 2. *Surface science* **160,** 451–466 (1985).
79. Lee, T.-S., Esposito, B., Donley, M., Zabinski, J. & Tatarchuk, B. Surface and buried-interfacial reactivity of iron and MoS 2: a study of laser-deposited materials. *Thin solid films* **286,** 282–288 (1996).
80. Zabinski, J. & Tatarchuk, B. Chemical reactivity at buried-interfaces: I. Iron on stoichiometric molybdenite. *Surface science* **241,** 157–170 (1991).
81. Zabinski, J., George, T. & Tatarchuk, B. Chemical reactivity at buried-interfaces: II. Iron on nonstoichiometric and/or defected molybdenite. *Surface science* **241,** 171–189 (1991).
82. Brillson, L. The structure and properties of metal-semiconductor interfaces. *Surface Science Reports* **2,** 123–326 (1982).

83. Riley, J. *et al.* Negative electronic compressibility and tunable spin splitting in WSe2. *Nature nanotechnology* **10,** 1043–1047 (2015).